Electrical Characterisation of Aerospace Grade Carbon-Fibre-Reinforced Polymers

PhD Thesis

Rabia Abid

December 2015

CARDIFF SCHOOL OF ENGINEERING

ABSTRACT

This thesis is primarily concerned with experimental tests and computer simulations to determine electrical characteristics of carbon fibre composites used in aerospace. The work has involved an extensive review of published literature, numerical modelling and experimental findings on electrical characterization of carbon fibre composites.

The numerical modelling on carbon composites was carried out using finite element package COMSOL, using preliminary conductivity values from literature. Lightning impulse waveform D was used, on a surface electrode to study the effect of lightning strike on carbon composites. Existence of shared equi-potentials was found.

Low current testing using variable ply lay ups of carbon composites was performed, the resistance measurements were taken using two probe method for volume conductivity, these values were compared and complied well with the values in literature. Surface resistance was also measured using new techniques, which introduced material and contact resistance into the parasitic resistance, the measurements of parasitic resistance gave an accurate measure of current distortion in variable ply layups. The current distortion was more transverse to the fibre direction and less in line to the fibre direction.

High current testing was performed using high voltage system in Cardiff high voltage lab, this was done for two current ranges Amperes and kA range. For both current ranges the samples were tested for mechanical strength requirements keeping in mind the mechanical design requirements for aircraft designers, it was found that the mechanical strength for samples impact with lightning impulse was not effected in Amperes range however it starts to effect in kA range at 11 kA.

Thermal damage in carbon composites was viewed under the scanned electron microscope using continuous current injection into a carbon composite sample obtained from a T joint. The sample microstructure showed that the fibres have splits and cracks along their diameters which shows that the direct current will be quite damaging to carbon fibres and will disrupt their electrical network.

PUBLICATIONS

1. R. Abid, A. Haddad, H. Griffiths, D. Clark, M. Cole, S. Evans , "Electrical Characterization Of Aerospace Graded Carbon Fiber Reinforced Plastic Composites Under Low Current DC And Impulse Energizations", International Conference on Lightning and Static Electricity, USA, 2013
2. R. Abid, A. Haddad, H. Griffiths, D. Clark, M. Cole, S. Evans, "Mechanisms of Damage Propagation in Carbon Composites under High Impulse Current Magnitudes", 50th International Universities Power Engineering Conference (UPEC), Staffordshire University, UK, 2015

AWARDS

Best Paper Award Certificate, 50th International Universities Power Engineering Conference (UPEC 2015), Staffordshire University UK for the paper entitled "Mechanisms of Damage Propagation in Carbon Composites under High Impulse Current Magnitudes".

DECLARATION

This work has not previously been accepted in substance for any degree and is not currently submitted in candidature for any degree.

Signed…….. (candidate) Date……

Statement 1

This thesis is being submitted in partial fulfilment of the requirements for the degree of PhD

Signed…….. (candidate) Date……

Statement 2

This thesis is the result of my own independent work/investigation, except where otherwise stated. Other sources are acknowledged by explicit references.

Signed…….. (candidate) Date……

Statement 3

I hereby give consent for my thesis, if accepted, to be available for photocopying and for inter-library loan, and for the title and summary to be made available to outside organisations.

Signed…….. (candidate) Date……

Statement 4: PREVIOUSLY APPROVED BAR ON ACCESS

I hereby give consent for my thesis, if accepted, to be available for photocopying and for inter-library loans **after expiry of a bar on access previously approved by the Graduate Development Committee.**

Signed…….. (candidate) Date……

ACKNOWLEDGEMENTS

In the name of Allah Almighty, the most beneficent most gracious and most merciful, who blessed me with the wisdom, knowledge and strength to accomplish my goal.

I want to thank my supervisors and mentors, Prof. Manu Haddad and Dr. Huw Griffiths, for their help and support all through the project. I am grateful for their patience during my studentship and for correcting my mistakes that always led to my betterment. I would also like to thank Dr. David Clark for designing experiments and devising measurement techniques for my work, and Mr. Chris Stones at MBLL and Airbus Group Innovations for sponsoring this studentship**.**

I also thank my parents, Abid and Tasneem, for their great support.

NOMENCLATURE

a	Radius of the metal fastener
A	Total damage area
AC	Alternating current
A_c	Area of composite
A_f	Cross-sectional area of fibre
b	Distance between the metal fastener and the metal ring
C	Capacitance
$D1$	Diameter of the central electrode on the top surface
DC	Direct current
g	Gap between top electrode and sample
GF	Gauge factor
I	Current
$I_{circuit}$	Current passing through the circuit
I_p	Peak current
I_t	Injected current
J	Joule heating
L	Length of the sample
l	Electrode spacing
N	Number of fibres
N_b	Number of carbon fibres
N_d	Number of diagonal plies
N_o	Number of non-diagonal plies

P_{ec}	Electrical power dissipated via current flow into the conductor
p_j	Impact threat
Q	Net electrical charge
r	Distance between the end of the fastener and the end of the metal ring
R	Resistance
R_0	Resistance at zero strain
R_a	Apparent resistance
R_c	Contact resistance
R_c	Resistance of the composite
R_d	Dispersion resistance
R_e	Electrode resistance
R_t	Total resistance of fibre
R_m	Material resistance
R_v	Resistance at peak current intensity
S_c	Cross-sectional area of carbon fibres
S_t	Total cross-sectional area of the sample
t	Thickness of the composite
t_d	Thickness of diagonal plies
t_o	Thickness of non-diagonal plies
t_{ply}	Thickness of a ply
V	Voltage
V_f	Fibre volume fraction
V_{Ip}	Peak voltage
W	Width of the sample
x	Spatial coordinate in x direction

y	Spatial coordinate in y direction
Z_p	Impulse resistance
α	Euler angle
δ_e	Electrical ineffective length
ΔR	Change in resistance
ε_L	Applied strain
ε_r	Relative permittivity
ϑ	Critical volume fraction
ϑ_c	Critical volume fraction of the conducting constituent
θ	Ply orientation
ξ	Damage parameter
ρ	Apparent resistivity
ρ_c	Resistivity of the carbon-fibre-reinforced plastics
ρ_{long}	Longitudinal resistivity
σ	Conductivity
σ_0	Conductivity of the conducting phase
σ_{cp}	Cross-ply conductivity
σ_L	Longitudinal conductivity
σ_T	Transverse conductivity

TABLE OF CONTENTS

ABSTRACT II
PUBLICATIONS III
AWARDS III
DECLARATION IV
ACKNOWLEDGEMENTS V
NOMENCLATURE VI
TABLE OF CONTENTS IX
INTRODUCTION 1
1.1. BACKGROUND 1
1.2. AIMS AND OBJECTIVES 2
1.3. CONTRIBUTIONS OF THIS THESIS 3
1.4. CHARACTERISATION OF THE BEHAVIOUR OF DIFFERENT CARBON COMPOSITES 4
1.5. MATERIAL AND PLY LAY-UPS 5
1.6. THESIS LAYOUT 5
STRUCTURE AND ELECTRICAL RESISTANCE OF CARBON-FIBRE-REINFORCED PLASTICS (CFRPS) - A REVIEW 8
2.1 INTRODUCTION: MATERIAL CONSTRUCTION 8
2.2 STRUCTURAL AND ELECTRICAL PROPERTIES OF CARBON FIBRE COMPOSITES 11
2.3 FACTORS AFFECTING THE STRENGTH OF CARBON FIBRE COMPOSITES 13
2.4 FASTENERS 14
2.5 STRUCTURAL PROCESSING OF CARBON FIBRES 14
2.6 ELECTRICAL PROPERTIES OF RESIN 18
2.7 LONGITUDINAL RESISTANCE 19
2.8 TRANSVERSE RESISTANCE 22
2.9 MEASURING THE ELECTRICAL CONDUCTIVITY OF CARBON-FIBRE-REINFORCED PLASTICS 24
2.9.1 Four-probe resistance measurements 25
2.9.2 Four-probe measurements of potential change 26
2.9.3 Advantages of four-probe resistance measurements 26
2.9.4 Multi-probe method 27
2.10 ELECTRICAL RESPONSE OF CARBON-FIBRE-REINFORCED PLASTICS UNDER MECHANICAL LOADING 27
2.11 ELECTRICAL RESISTANCE TO MEMORIZE MAXIMUM LOAD 32
2.12 MAPPING ELECTRICAL CONDUCTIVITY USING ELECTRICAL RESISTANCE 34
2.1 ELECTRICAL RESISTANCE AS A DAMAGE MONITORING TOOL 38
2.2 CONCLUSIONS 43
POTENTIAL AND CURRENT DISTRIBUTION IN CARBON COMPOSITE PANELS: NUMERICAL MODELLING AND LABORATORY TESTS 44
3.1 BACKGROUND 44
3.2 LIGHTNING ATTACHMENT ZONES 46
3.3 DIRECT EFFECTS OF LIGHTNING ON AIRCRAFT 49
3.4 DEFINITION OF VOLTAGE WAVEFORMS 50
3.5 SINGLE-LAYERED PANEL—NUMERICAL MODELLING 52
3.6 MODELLING A TWO-LAYERED PANEL 55

3.7 MODELLING THE EXPERIMENTAL PANEL STRUCTURE 58
3.8 EXPERIMENTAL STUDIES OF FLAT PANELS 60
3.9 SIMULATIONS OF LIGHTNING STRIKES 61
3.10 CURRENT AND POTENTIAL DISTRIBUTION IN TWO LAYERED PANELS 64
3.11 POTENTIAL PROFILES 69
3.12 THROUGH-THICKNESS POTENTIAL PROFILES 70
3.13 EMBEDDED ELECTRODE DESIGN SIMULATION 74
3.14 CONCLUSIONS 77
ELECTRICAL CHARACTERISATION: SURFACE AND VOLUME RESISTANCE STUDY 78
4.1 INTRODUCTION: TWO- AND FOUR-PROBE METHODS 78
4.2 ABRASION TECHNIQUES 79
4.3 ELECTRODE FORMATION TECHNIQUES ` 79
4.3.1 Silk screening using conductive silver paint 80
4.3.2 Open contacts with a spring-loaded configuration 80
4.3.3 Sealed contacts with soldered terminals 82
4.3.4 Photo etching 83
4.3.5 Wire/braid setting with paint 86
4.3.6 Thermal vacuum evaporation 87
4.4 CFRP RESISTANCE MEASUREMENT TECHNIQUES AND RESULTS 89
4.4.1 Proposed measurement approach for carbon fibre samples 89
4.4.2 Test configurations and procedure for surface characterisation 90
4.4.3 Resistance Calculation Procedure 92
4.4.4 Cross-ply sample 97
4.4.5 Resistance profiles on composite surfaces 97
4.5 VOLUME CHARACTERIZATION 102
4.5.1 Test configurations for volume characterisation 102
4.5.2 Impulse circuit 103
4.6 VOLUME CHARACTERISATION RESULTS 105
4.7 TWO-WIRE MEASUREMENT OF QUASI-ISOTROPIC PLY LAY-UPS 109
4.8 VARIABLE ALTERNATING CURRENT CIRCUIT 110
4.9 TWO-WIRE RESISTIVITY MEASUREMENTS FOR CROSS-PLY LAMINATES 113
4.10 NON-DESTRUCTIVE ELECTRICAL CHARACTERISATION UNDER LIGHTNING IMPULSE CURRENTS OF LESS 100A 114
4.10.1 Concentric ring electrode tests 114
4.11 CONCLUSIONS 121
MECHANISMS OF DAMAGE PROPAGATION IN CARBON COMPOSITES UNDER HIGH IMPULSE CURRENT MAGNITUDES AND DC CURRENT 123
5.1 INTRODUCTION: DAMAGE TO CARBON FIBRE COMPOSITE PARTS/STRUCTURES DUE TO LIGHTNING STRIKES 123
5.2 PROTECTING CARBON FIBRE COMPOSITES AGAINST LIGHTNING STRIKES 127
5.3 EXPERIMENTAL PROCEDURE FOR HIGH CURRENT TESTS 129
5.4 IMPULSE CURRENT TESTS (UP TO 350 A) 131
5.5 METAL RING SAMPLES SUBJECTED TO 350 A IMPULSES 132
5.6 CHARACTERISATION OF CFRP PANELS UNDER WAVEFORM D LIGHTNING STRIKE 136
5.7 MECHANICAL TESTS ON WAVEFORM-D-IMPACTED SAMPLES 142
5.8 MICROSCOPIC DAMAGE ANALYSIS 145
5.9 SIMULATIONS OF MULTI-LAYERED CARBON FIBRE COMPOSITES 149
5.9.1 Simulations without aluminium fasteners 149

5.9.2 Simulations with an aluminium fastener *152*
5.9.3 Current distribution in CFRP panels in the presence of fasteners *153*
5.10 THERMAL DAMAGE DUE TO PROLONGED DIRECT CURRENT APPLICATION 156
5.11 CONCLUSIONS 160
CONCLUSIONS AND FUTURE WORK 162
6.1 CONCLUSIONS 162
6.2 FUTURE WORK 166
REFERENCES 168

Chapter 1

INTRODUCTION

1.1. Background

With the on-going quest towards more lightweight aircraft and better fuel efficiency, the demand is greater from the aerospace industry to replace conventional materials with composite equivalents. Owing to their high strength to weight ratio, carbon-fibre-reinforced plastics (CFRPs) are already well established and the 20% increase in fuel efficiency that they offer has resulted in substantial fuel savings. The anisotropic electrical conductivity of CFRPs, which is high along the fibres but minimal across them, stems from the arrangement of the different components, with conducting carbon fibres in different orientations reinforced with epoxy to fulfil mechanical strength requirements. This leads to complex electrical phenomena under different external conditions. Anisotropic electrical conductivity also accounts for the unpredictable behaviour of CFRPs under lightning strikes and the inevitable damage that arises. The resistivity of CFRP materials is 1000 times higher than that of aluminium, such that a CRFP sample will dissipate 1000 times more energy than an equivalent one made of aluminium for the same lighting current magnitude. The risk of lightning-induced damage is, therefore, much greater for CFRPs as the electrical charge is less readily dissipated. This damage may involve thermal decomposition of the epoxy layers, melting and burning, de-lamination, and vaporisation of the resin. A thin protective metal layer (typically 20-μm thick) is commonly coated on CFRPs to dissipate lightning current and to prevent its penetration into the material. However, this layer also makes the material and, hence, the aircraft heavier.

A key objective is, therefore, to design CFRP components and structures with effective lightning protection without compromising their other attractive properties for the aerospace industry, principal among which is their lightweight nature. Understanding the electrical behaviour of these materials is indispensable in this context and involves characterising their electrical properties (primarily their electrical resistance) under different modes of energisation. Ultimately, a detailed study of effect of lightning currents is required.

This thesis also investigated the effect of lightning current on residual mechanical strength in carbon fibre composites. Important observations were that low-level lightning currents up to 350A do not cause any significant damage. However, lightning currents in the kA range can do.

1.2. Aims and objectives

The purpose of this work was to characterise the low-voltage, low-current behaviour of carbon fibre composites using cost-effective, electrical-based methods and to understand the effects of lightning strikes. The primary objectives were:

- To develop cost-effective techniques only requiring the attachment of surface electrodes to study material behaviour in the multi-layered carbon composites used in the aerospace industry.
- To investigate the effects of different electrical contacts on the studied materials using different electrode connection methods.
- To develop new techniques to study the effect of lightning currents on the behaviour of composite materials.
- To analyse the mechanical strength degradation of carbon fibre composites under lightning impulses of Amperes range and Lightning strikes in the kA range. These affect

both the mechanical and electrical performance of the composite components and structures.

1.3. Contributions of this thesis

This thesis investigates the bulk electrical properties of aerospace multi-layered carbon composites. This thesis also examines the effect of lightning strikes on multi-layered carbon fibre composites. The novelties of this work are as follows:

- New surface characterisation methods were adopted to study the behaviour of anisotropic multi-layered carbon fibre composites, with electrodes attached only to the surface, avoiding (except for high-current testing) the need for embedded electrical contacts.
- The bulk properties of the materials were measured as energised by AC, DC, and impulse currents to characterise their behaviour. The bulk properties were then used to characterise the electrical equivalent circuits for a large range of samples, including diagonal layers and cross-ply arrangements.
- Numerical models were developed using finite element theory to study the effects of different energisation modes on the behaviour of the material. These models were solved using the advanced research computing facility at Cardiff University.
- Microscopy studies have been performed on the internal structure of carbon fibre composites which were subjected to lighting impulse and prolonged direct current injection. These studies reveal independent resin and carbon fibre layers in the materials destined for aerospace applications.

1.4. Characterisation of the behaviour of different carbon composites

The electrical behaviour of composites with different ply lay-ups and composed of different materials was studied using two-wire and four-wire measurement techniques. For the two-wire measurements, the terminal voltage includes the contact resistance of the wires and the voltage drop along the sample in the direction of current flow. The direction of measurement is always indicated with respect to the orientation of the top layer, regardless of the orientation of those underneath. As will be shown later, the top layer, oriented at 0° by definition for most ply lay-ups, was configured to facilitate bulk resistance measurements using the two-wire technique.

In the four-wire setup, two electrodes are used for current injection while the remaining two are used for voltage measurement. The distance between the electrodes is varied according to the sample type and dimensions. The electrodes can be prepared using either silver paint or silver evaporations in a thermal vacuum chamber, and placed along the entire perimeter of the samples. Gap electrodes are used for measurements in the thickness direction, with the outer electrode used to inject current and the inner electrode used to record the voltage.

Resistance measurements in the thickness direction can be performed according to the ASTM D257 standard (referred to as ‘concentric ring electrode’ tests in the following). The gap ‘g’ between the top electrode and the sample should be at least twice the sample thickness, whereas the bottom (or ground) electrode is in contact with (and covered) the surface.

The samples can be energised using direct, alternative, and impulse currents. The behaviour of the samples can then be characterised under direct currents of 0–1 A and under alternating currents of 0–1 A at 50–100 kHz. If the voltage and current waveforms are captured using a digital storage oscilloscope, the phase angle between the voltage and the current can be

determined from the offset between the waveforms. In addition, for the impulse study, energy dissipation can be measured at peak current intensity using a waveform typical of lightning strikes. The total energy dissipation E, can be determined from the integral of the product of the voltage, V and the current I:

$$E = \int_0^\infty VI \, dt \tag{1-1}$$

1.5. Material and ply lay-ups

Aerospace grade carbon composites were investigated, namely the M21/T800s, M21/T700s, and HTS/977-2 carbon composites.

1.6. Thesis Layout

This chapter motivates the development in this work of methods and techniques to study the behaviour of carbon-fibre-reinforced composites for aerospace applications. This thesis is divided into seven chapters, references are numbered in square brackets and correspond to a full list at the end of the thesis. The content of each main chapter is summarized as follows.

Chapter 2: Structure and electrical resistance of carbon-fibre-reinforced plastics (CFRPs): A review

Chapter 2 is a survey of the existing literature on this topic and compares the approaches developed by other researchers in this context with those used and developed in this thesis. The electrical characterization methods investigated by other researchers are reviewed. The review provides an insight into areas not investigated and published before such as the mechanical strength degradation of carbon composites impacted under low current lightning impulse of Amperes range.

Chapter 3: Potential and Current Distribution in Carbon Composite Panels: Numerical Modelling and Laboratory Tests

Chapter 3 presents the numerical models developed to simulate the behaviour of multi-layered carbon fibre composites. The numerical models initially were developed for two layered panels. After preliminary numerical modelling, actual lightning strike boundary conditions were incorporated into the model. Under lightning strikes, existence of shared equi-potentials was found, termed as 'twisting' by other researchers. Other configurations numerically modelled comprised through thickness resistance study of samples on which electrodes were made using guard electrode. Voltage profiles were obtained along horizontal and vertical paths.

Chapter 4: Electrical Characterization: Surface and Volume Resistance Study

Chapter 4 explains in detail how the samples and electrodes were prepared to measure the surface and bulk/volume properties of carbon composite materials. This chapter also discusses the laboratory equipment and setup used in this investigation for the three different energisation modes (viz. via direct, alternating, and impulse currents) and terminal voltage measurements. This chapter also presents the experimental results including electrical conductivity obtained from low voltage measurements under different energisation modes.

Chapter 5: Mechanisms of damage propagation in carbon composites under low direct current and high impulse current magnitudes

Chapter 5 discusses the results of tests performed on the samples under low (Amperes) and high (kA) intensity currents. The mechanical strength degradation and the micro structural assessment due to damage caused to carbon composites for each current range is also

discussed in this chapter. This chapter also reports the effect of continuous direct current injection into carbon composite obtained from a real aircraft structure such as the T- joint.

Chapter 6: Conclusions and Future Work

Chapter 6 summarizes the goals achieved in this work and outlines potential avenues for future work in this field.

Chapter 2`

STRUCTURE AND ELECTRICAL RESISTANCE OF CARBON-FIBRE-REINFORCED PLASTICS (CFRPs) - A REVIEW

2.1 Introduction: Material construction

Carbon fibre materials have proved particularly popular in the aerospace industry since the beginning of the century. The improved tensile strength and rigidity of the carbon fibre materials typically employed in engineering stems from the incorporation of the carbon fibres in a polymer (e.g. epoxy) matrix [1]. The resulting composites have unique properties and perform better, particularly under loading, than the individual components. This explains their current attractiveness and their widespread use in industry.

Since the fibres support most of the load, reinforcement notably improves the fatigue resistance of a material. As explained by Langley [1], the main advantage of carbon fibre composites over conventional materials is that the carbon fibre component can be tailored within the structure to meet design requirements. This tailoring enables more cost-effective material utilization.

Clyne and Hull [2] discuss different fibre-packing arrangements. In unidirectional lamina, the fibres are aligned parallel to each other, arranged in a hexagonal or square lattice in which

each fibre has a circular cross section of the same diameter. As shown in Figs. 2–1 and 2–2 respectively, the carbon fibres in an epoxy matrix can be roughly circular with an irregular surface [3], or woven in a laminate [4] (a laminate is a bonded stack of lamina with different orientations), as shown in Fig. 2–2.

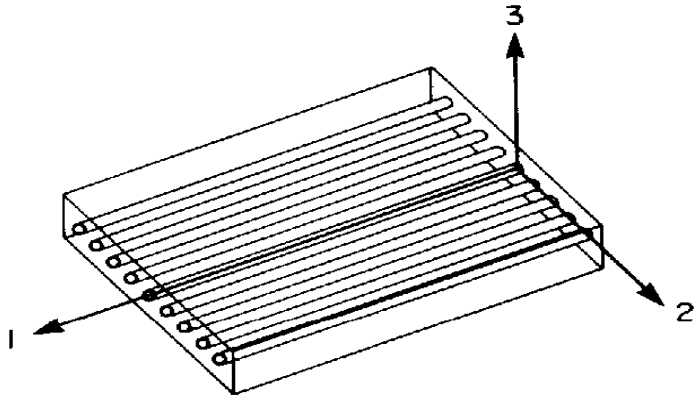

Fig. 2-1. Schematic of an aligned-fibre laminate [3] and the corresponding axis system used in this work.

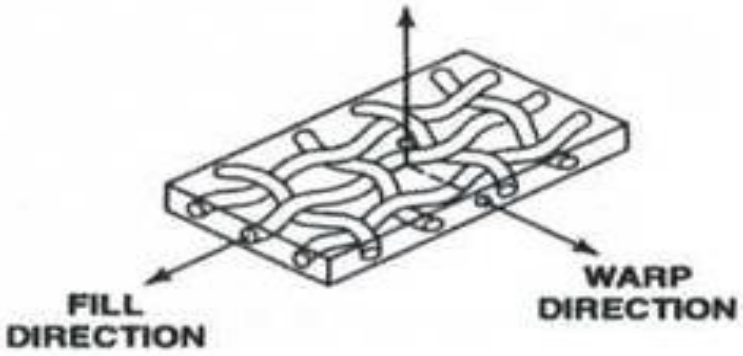

Fig. 2-2. Schematic of a woven-fibre laminate [4].

Graphite epoxies are generally treated as linear elastic materials because most of their strength and stiffness stems from their linear elastic fibres [5].

Fig. 2–3 shows the laminate structure of a CFRP. The fibre orientation varies between subsequent lamina. Lamination typically enhances the mechanical strength of the material; it can, therefore, be used to match the structural requirements of particular applications.

Understanding the factors governing the structural integrity of carbon fibre composites requires a detailed study of their internal arrangement.

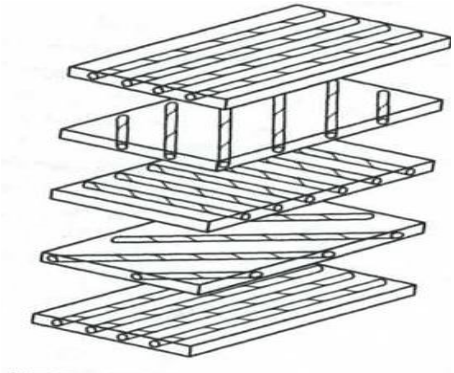

Fig.2-3. Schematic un-bonded view of the arrangement of the different layers in a typical CFRP laminate [5].

Angelidis et al. [6] discuss the effects of different structural arrangements on the properties of carbon-fibre-reinforced composites, whose electrical resistance can be adjusted and whose carbon fibres form a sensing network. These authors investigated the effects of mechanical strain on the electrical resistivity of both unidirectional and multidirectional CFRP laminates. They found that the plies in multidirectional laminates provide alternative paths for current flow, ensuring uniform potential distributions through their resistivity. In contrast, in unidirectional CFRP samples, the applied strain was found to alter the resistivity and geometry of the fibres resulting in less uniform current flow.

Although low-modulus carbon fibres were used in their work (i.e. T300-class materials with a resistivity of 17 $\mu\Omega\cdot m$), Angelidis et al. [6] highlight the fact that data on the piezoresistance of T300 fibres are lacking. There are, therefore, no standard datasets available with which to authenticate the use of this type of fibre. Importantly, however, the authors define conditions (previously unclear) for which either large positive or negative piezoresistances can be expected for CFRPs.

Angelidis et al. [6], thereby, have set important benchmarks for the current demands from industry for investigations of the effects of mechanical strain on the electrical resistance of CFRPs. Indeed, since the electrical resistivity of CFRPs can be 1000 times that of aluminium, the former are far more susceptible to damage from lightning strikes. This topic is discussed in the following section.

2.2 Structural and electrical properties of carbon fibre composites

Morley has used graphite crystals to model the characteristics and applicability of carbon fibre composites [7]. Graphite layers bond via van der Waals forces with a spacing of approximately 0.335 nm. Graphite is, therefore, a thermal and electrical insulator perpendicular to the layers, its anisotropic properties stemming from the differences between its in-plane and out-of-plane bonding. Graphite has respectively a high and low elastic modulus parallel and perpendicular to the carbon planes. This directionality accounts for the inhomogeneity and anisotropic nature of the carbon fibres in carbon fibre composites. Air pockets can also form in graphite owing to its porous structure [8].

The aforementioned anisotropy makes the overall mechanical properties of carbon fibre materials different parallel and perpendicular to the graphene sheets. As a consequence, the physical properties of these materials vary as a function of the number of fibre lay-ups and their orientation, as well as with their fibre to epoxy resin ratio. Differences in fibre lay-ups affect the resistivity of the overall material in particular directions. Lodge [9] has tabulated the typical resistivity of carbon-fibre-reinforced plastic materials with different lay-ups (Table 2-1).

The work performed by Saleem et al. [10] is of particular interest. These authors prepared composites using thermoplastic polymers—polyetheretherketone (PEEK) and

polyethersulphone (PES)—and carbon fibres. The mechanical, thermal, and electrical properties of these composites were studied as a function of material composition to analyse the effects of carbon fibres on the overall properties of the composites. Higher values of the storage modulus (used to quantify the mechanical properties) were obtained when carbon fibres were included. An increase in the thermal and electrical conductivities of the composites was also observed. The former also increased with the temperature and filler concentration.

Table 2-1: Typical resistivity of carbon-fibre-reinforced plastic materials with different lay-ups [9].

Lay-up	**Resistivity [Ω·m]**			
	0°	**45°**	**90°**	**Through-thickness**
0°	2.5	-	1000	>1000
0°/90°	5	120	5	>1000
±45°	8–16	5	8–16	>20000
0°, ±45°, 90°	3.6	3.35	3.6	900
Woven cloth	3.8–6.3	-	3.8–6.3	>20000

Saleem et al. [10] also determined the electrical conductivity of the composites using the percolation threshold. This parameter is indicative of the conductive bridges that form in the composites. In the PEEK/CF and PES/CF composites, the percolation threshold occurred at CF concentrations of 35 wt% and 10 wt%, respectively.

It should be noted that Saleem et al. [10] only studied the properties of the composites that improved following the addition of carbon fibres or by using different matrices. They did find, however, that the PEEK composite becomes brittle after mixing because of its increased crystallinity. These authors did not focus on factors that could affect the strength and other properties of the CFRPs. These factors are very useful in predicting the behaviour of these

composites under specific conditions. This topic is discussed in greater detail in the following section.

2.3 Factors affecting the strength of carbon fibre composites

The popularity of carbon fibre composites in industry stems from their attractive mechanical properties, which generally include their high strength, high stiffness, and low weight. Research is on-going in this context to better understand the factors that degrade, or conversely, improve the strength of these composites.

Carbon fibre composites are corrosion resistant. Nonetheless, Heath [11] found that exposure under various environmental conditions leads to the rapid degradation of the strength of these materials. Following 2000 h of exposure at 70°C and 100% relative humidity, shear strength, flexural strength, and flexural thickness of the samples had degraded by 40%, 25%, and 5%, respectively.

Heath also reports an additional problem arising for carbon fibre composites in contact with aluminium alloys that the metal corrodes in the presence of a salt solution (electrolyte). Furthermore, his results demonstrate that carbon fibre composites are readily eroded by rain or sand. Specifically, under standard test conditions and a rainfall rate of 25.4 mm/h, a 500 mm^2, 3.81-mm thick piece of carbon fibre laminate is completely eroded in 15 min. In comparison, 20 h are required under the same conditions for the complete erosion of a copper specimen of the same thickness. A nickel or neoprene coat is, therefore, essential to enhance resistance to erosion of carbon fibre composites. Heath's conclusions and findings [11] are extremely important regarding the effects of the environment on the strength of CFRPs.

Heath also investigated the lack of robustness of carbon fibre composites [11], which precludes their use in manufacturing structures, such as leading edges and windscreen frames.

Moreover, carbon fibre composites do not attach well to fasteners, such as bolts and rivets commonly used to make mechanically coupled joints in aircraft structures.

Howell [12] has shown that two crucial factors leading to the degradation in strength of carbon fibre composites are their moisture content and mechanical loading. Reid [13] verified this result by showing that the loading level and initial sample temperature both affect the degradation in strength of CFRPs.

2.4 Fasteners

Composite structures carrying high structural loads are mechanically fastened together using metal fasteners. This results in corrosion due to the difference in the electrical conductivities between the composite and the metal. Galvanic corrosion is the most common when steel or aluminium fasteners are used. Titanium fasteners, lighter than other metal fasteners, have been proposed as a solution to this problem. Their high cost as well as the sophisticated machining that is required for their manufacturing has prevented their extensive use. Composite fasteners have also been proposed in this context [14], but their relatively poor fatigue resistance has proved problematic. Indeed, Starikov and Schön [15] compared the fatigue resistance of titanium and composite fasteners and showed that the former performed better than the latter. Because of bolt fractures, the composite fasteners failed under cyclic shear loading at lower level than the titanium fasteners did. The use of fasteners to join composite parts clearly remains an issue.

2.5 Structural processing of Carbon fibres

The high tensile strength, and in general, the mechanical properties of CFRPs, stem from the presence of reinforced carbon fibres within the composite material. Carbon fibres support

most of the load in CFRP structures, improving their fatigue resistance [15]. Furthermore, the high thermal conductivity of the carbon fibres prevents the thermal degradation that usually occurs when plastics (e.g. epoxy) are subjected to cyclic loading.

Carbon naturally occurs in three basic forms, namely diamond, graphite, and fullerene. Diamond is isotropic and an insulator, whereas graphite and fullerenes are both electrical conductors [16]. Fig. 2–4 shows the structure of graphite, with layers of carbon atoms, known as graphene, interspaced 0.335 nm from one another. Within each plane, the carbon atoms are covalently bonded, forming a two-dimensional hexagonal network [17].

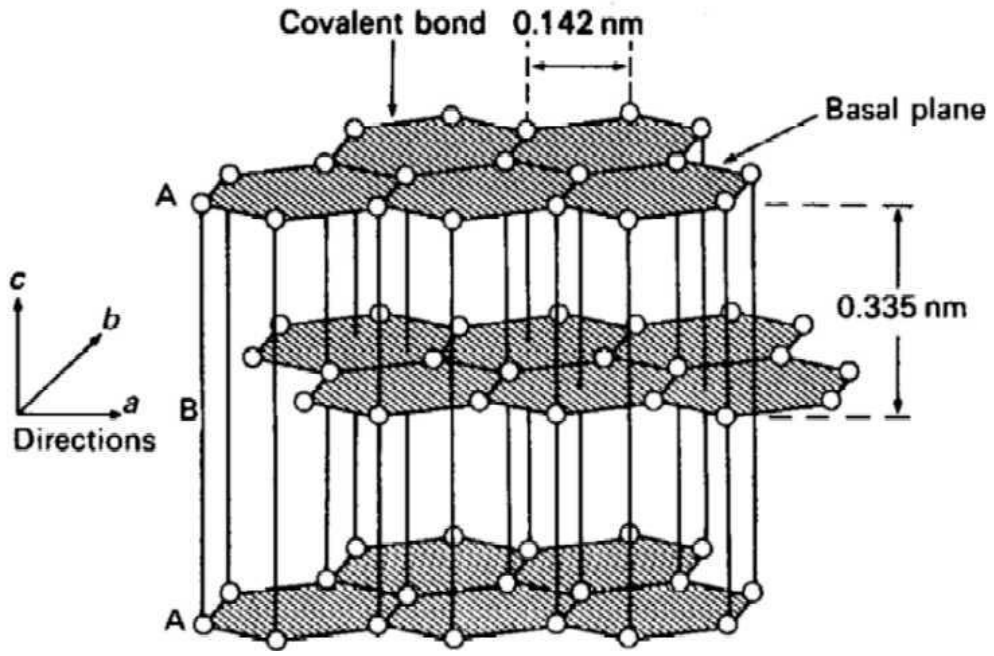

Fig. 2-4. Schematic showing the layered structure of graphite [17].

Carbon fibres are made of graphite. Commercially, they are manufactured using one of three basic precursors, organic polymers namely rayon (a cellulose fibre), polyacrylonitrile (PAN), and pitch. Pitch-based fibres are generally manufactured from petroleum asphaltene or coal tar, and rayon is manufactured from naturally occurring polymers. However, PAN is the most popular for the production of high-strength carbon fibres [18]. Polyacrylonitrile precursor fibre is a linear polymer that contains 68% carbon. These precursor fibres are converted to carbon fibres via a series of transformation steps, as detailed in the following steps.

First, the PAN fibres are heated in air at 200–230°C, for pre-oxidation and stabilization. The fibres are then carbonised and heat treated in an inert environment, first at ~1000–1500°C, and then at ~2000–3000°C [18] to stabilise the structure through a process known as graphitisation. The mechanical and electrical properties of the carbon fibres are primarily related to the heat treatment temperature and their microstructure.

Carbonization results in the formation of a hexagonal network that is subsequently aligned with the fibre axis at an angle of 20° [19]. This network stabilises and increases the tensile strength of the fibres. In the last transformation step, the graphitisation of the carbonised fibres, the fibres are stretched out and aligned, which improves their mechanical properties owing to the better orientation of the planes with respect to the fibre axis. The use of PAN is favourable in this context as its oxidization yields polynaphthyridine, which facilitates graphitisation.

Ideally, the carbon fibres should be crystalline. However, the fibres may contain impurities and the arrangement and orientation of the crystals affect its structural properties. Detailed knowledge of the microstructure of the carbon fibres is, therefore, crucial. Diefendorf and Tokarsky [20] propose that the basic unit of carbon fibres consists of undulating ribbon-shaped layers, as shown in Fig. 2–5. Increasing the elastic modulus of the individual fibres increases the thickness of these layers.

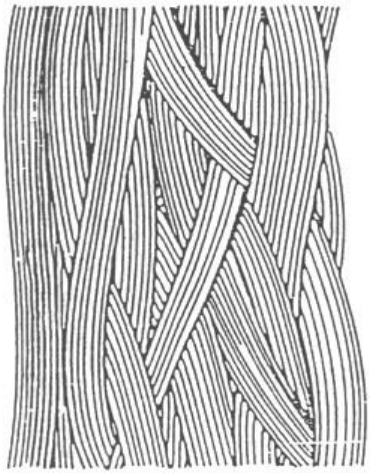

Fig. 2-5. Schematic representation of the ribbon-shaped, layered structure of PAN-based carbon fibres [20]

Guigon et al. [21] studied the evolution of PAN-derived carbon fibre structures during the transformation process. The authors showed that the structure consists of folded and creased sheets of layered planes linked at their boundaries. Below 800°C, the structure consists of short carbon layers (approximately 10 Å long), which accumulate to form a disordered columnar structure. This columnar structure subsequently increases in length up to a temperature of 1500°C, above which it is converted into wavy or wrinkled ribbons that persist up to 2100°C. With further increases in the temperature, the carbon fibres form a stiff three-dimensional crystal network [19].

The electrical conductivity of carbon fibres increases with the heat treatment temperature used during processing. Indeed, treating the fibres at higher temperatures improves the uniformity of their graphite structure. Watt and Perov [22] have investigated the effect of the heat treatment temperature on the electrical resistivity of carbon fibres, as shown in Fig. 2–6.

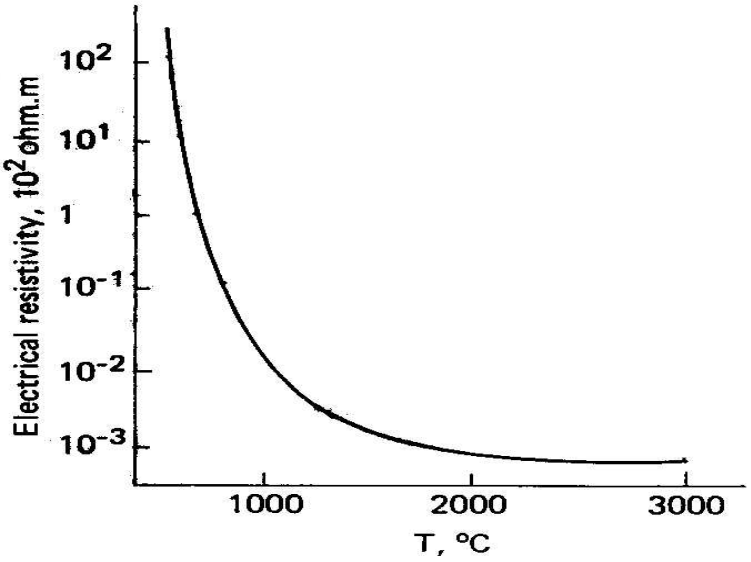

Fig. 2-6. Electrical resistivity of carbon fibres as a function of the heat treatment temperature used during their preparation [22].

2.6 Electrical Properties of Resin

As stated at the beginning of this section, the other component of CFRPs is the polymer matrix. Polymers are electrical insulators because they lack free electrons for conduction. The resistivity of the polymer used in CFRPs, epoxy resin, is particularly high, ranging from 7.34 $\times 10^{11}$ Ω·m to 1.25 $\times 10^{13}$ Ω·m [23]. The polymer matrix is weaker than the carbon fibres and is the first to incur damage under various environmental conditions. Epoxy resin typically evaporates under high currents or voltages. Although this is still a matter of debate in the literature, carbon fibres are thought to shield and protect the inner epoxy layers from the penetration of high currents. Epoxy matrices also tend to crack, especially under load. These cracks then propagate, further weakening the structure. Epoxy is also subject to thermal decomposition (pyrolysis) under lightning strikes, in particular.

The electrical conductivity of CFRPs is anisotropic and is highest along the fibres, which facilitate current flow. The longitudinal conductivity of CFRPs is, therefore, always greater than their transverse and through-thickness conductivities. Typical values for the longitudinal electrical conductivity range from 5×10^3 S/m to 5×10^4 S/m, whereas the transverse conductivity ranges from 10 S/m to 100 S/m [24]. The conductivity of each ply in CFRPs is dependent on several parameters, notably the fibre type, orientation of the plies, and the volume fraction they occupy. This information was used by Grimberg et al. [24] to determine an anisotropic conductivity tensor, $\bar{\bar{\sigma}}$, that correlates the overall conductivity of a CFRP with its directional conductivities, with σ_L being the longitudinal and σ_T being transverse conductivity respectively:

$$\bar{\bar{\sigma}} = \begin{pmatrix} \sigma_L cos^2(\theta) + \sigma_T sin^2(\theta) & \frac{\sigma_L - \sigma_T}{2} sin(2\theta) & 0 \\ \frac{\sigma_L - \sigma_T}{2} sin(2\theta) & \sigma_L sin^2(\theta) + \sigma_T cos^2(\theta) & 0 \\ 0 & 0 & \sigma_{cp} \end{pmatrix} \quad (2\text{-}1)$$

The cross-ply conductivity, σ_{cp}, is the result of the interaction between the fibres of adjacent plies and is typically half the value of the transverse conductivity [24].

2.7 Longitudinal resistance

As reported by Angelidis et al. [6], when current is applied to unidirectional CFRP laminate materials, the electron flow is maximum in the direction parallel to the fibres. Carbon-fibre-reinforced plastics can, therefore, be modelled as a matrix of resistors parallel to the fibres. In this model, the longitudinal resistivity, ρ_c, of CFRPs for current flow in the longitudinal direction (parallel to the fibres) is given by, where ρ_f, is the resistivity of the fibres and V_f, is the fibre volume fraction.

$$\rho_c = \frac{\rho_f}{V_f} \tag{2-2}$$

In the parallel resistor model shown in Fig. 2–7, each fibre is represented by a resistor [25].

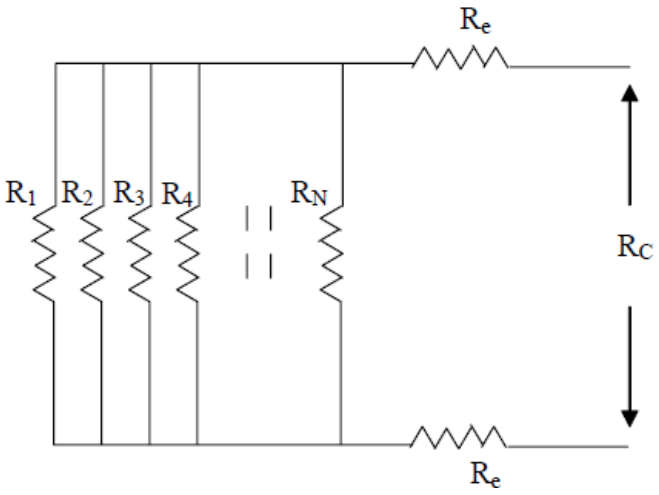

Fig. 2-7. DC circuit diagram showing the parallel resistance model of electrical conductivity in carbon-fibre-reinforced plastics [25]

Therefore, the total resistance of the fibres which is R_f, divided by their number, N, yields the resistance of the composite, R_C in the longitudinal direction:

$$R_C = \frac{R_f}{N} \tag{2-3}$$

The electrical resistance in the longitudinal direction can be measured using a pair of electrodes. Furthermore, if the cross-sectional area of the fibres,A_f, is known, then the resistance of the fibres, R_f, can be obtained from, resistivity of the fibres, ρ_f, and the distance between the electrodes, L.

$$R_f = \frac{\rho_f L}{A_f} \tag{2-4}$$

The number of fibres, N is given by the relation

$$N = \frac{A_c V_f}{A_f} \tag{2-5}$$

Where, A_c , is the area of composite, V_f is the fibre volume fraction, and A_f, is the area of the fibres.

Substituting Eqs. (2-4) and (2-5) into (2-3) yields the resistance of the composite, R_c, in terms of ρ_f, fibre resistivity, area of the composite, A_c, and distance between the electrodes L.

$$R_c = \frac{\rho_f L}{A_c V_f} \tag{2-6}$$

Finally, including the contact resistances of both the electrodes, and the probes, R_e gives

$$R_C = \frac{\rho_f L}{A_c V_f} + 2R_e \tag{2-7}$$

These equations are valid for unidirectional laminates only. For multidirectional laminate materials, fibre breakage under different conditions (e.g. loading or damage) does not necessarily imply a reduction in current flow within the composite because broken fibres continue to carry current via contacts with unbroken fibres in the vicinity. The length over which a broken fibre is able to form these contacts has been dubbed the 'electrical ineffective length' by Park et al. [26]. Therefore, although it is valid for undamaged or unloaded CFRPs, the parallel resistance model does not fully account for the different phenomena occurring therein under load or if the fibres incur damage. As shown in Fig. 2–8, additional features need to be added to the model to make it more realistic, in particular, the electrical ineffective length, δ_e.

This model is composed of discrete cells whose resistance is independent from that of the others. For example, if a fibre (represented by a resistor) breaks within a cell in this model, the current will continue to flow through the circuit as long as the break is not longer than the electrical ineffective length, typically the distance between the fibres. The electrical

ineffective length, which accounts for the behaviour of CFRPs under mechanical loading, is discussed in detail in Section 2.9.

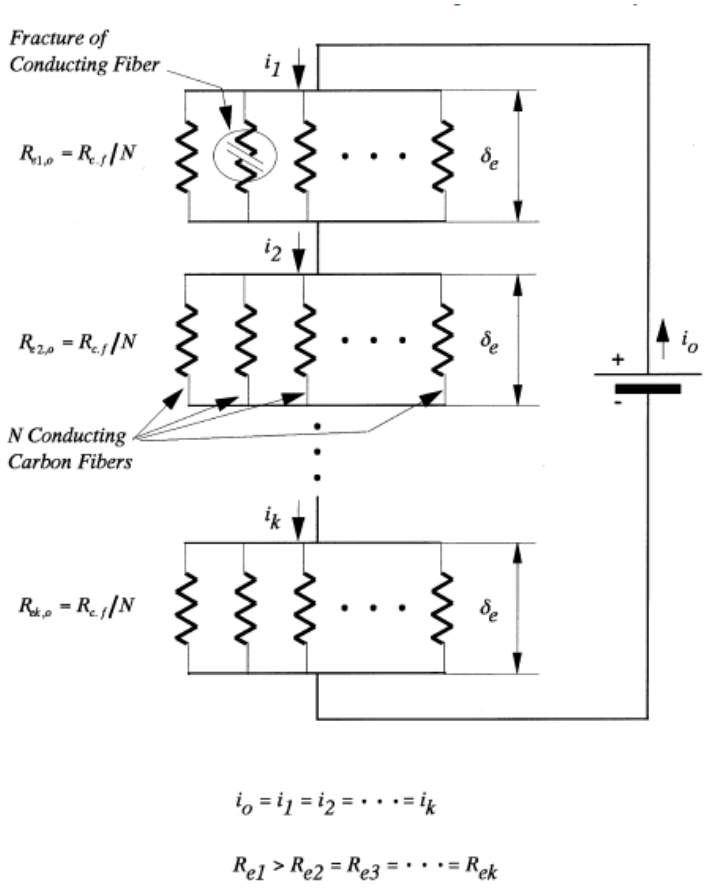

Fig. 2-8. Diagram of the DC circuit used to model electrical conductivity in carbon-fibre-reinforced plastics, with parallel arrays of resistors used to model the electrical ineffective length, δ_e [26].

2.8 Transverse resistance

The phenomena governing the transverse resistance can be described using effective medium theory (EMT) or percolation theory. In the first of these, an effective medium is used to represent the average effects of random resistors. Therein, the effects of external fields applied to a random resistor network are assumed to be equal to the effects of internal fields [27]. Effective medium theory provides reliable estimates of the effective conductivity when the conductivities of the different components of a material are similar. When these conductivities differ substantially, however, the values obtained using EMT are not reliable.

In contrast, percolation theory is a statistical method that can be used to predict conduction in polymeric composites by considering the volume content of conducting material in the composite [28]. According to percolation theory, the conductivity is given by σ,

$$\sigma = \sigma_0(\vartheta - \vartheta_c)^t \tag{2-8}$$

where σ_0 is the conductivity of the conducting phase, the exponent, *t*, is the rate of conductivity change [28], and ϑ_c is the critical volume fraction of the conducting constituent, known as the percolation threshold above which the composite is conductive. In other words, for a composite material to be conductive, the concentration of conducting fillers must be at or above the percolation threshold.

Weber and Kamal [29] have modelled the electrical conductivity of polymer composites reinforced with carbon fibres using theories both with and without percolation. As stated above, without percolation, the conductivity is described in terms of fibre orientation and length and other parameters related to their microstructure. The authors of [29] used Monte Carlo simulations to calculate the fibre concentration required to reach the percolation threshold.

As illustrated in Fig. 2–9, Weber and Kamal also compared different models for the electrical conductivity in two-phase systems with conducting particles, including one based on percolation theory. Among these, the Bueche model, which considers conducting particles in a non-conducting matrix, predicts that, at some critical concentration, the resistivity decreases sharply. The authors also examined the Nielsen model, which can be used to model both the electrical and thermal conductivities of two-phase systems, and the McCullough model, which can be used to predict the electrical conductivity in all principal directions. Fig. 2–9 shows that the McCullough model agrees with the experimental data obtained for an

aluminium powder-polyester composite. The Ondracek model and effective medium theory were also investigated.

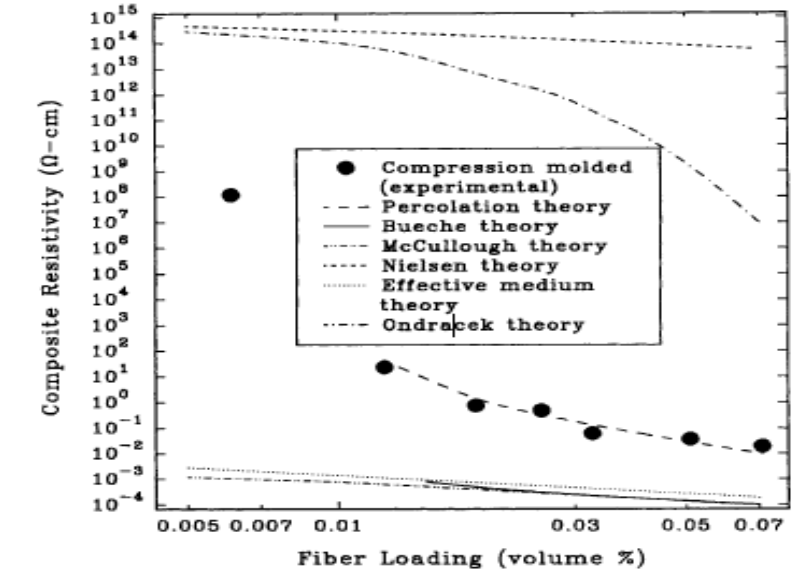

Fig. 2-9. Composite resistivity as a function of fibre loading as measured experimentally for an aluminium-powder polyester composite, and as predicted using various theoretical models [29].

2.9 Measuring the electrical conductivity of carbon-fibre-reinforced plastics

Experimentally, the two-probe method is most commonly used to measure the electrical resistance of CFRP panels. The resistance is measured using a digital multimeter. The two-probe method is simply based on Ohm's Law. To measure the conductivity of rectangular composite specimens, plate electrodes are used.

Excellent bonding between the electrodes and the composite is crucial to obtain accurate conductivity measurements. Moreover, for rectangular composite panels, the current density should be uniform. It is worth recalling that CFRPs are orthotropic and, as a consequence, their conductivity, σ, has to be calculated separately in each direction:

$$\sigma = L/(RA) \tag{2-9}$$

Where L is the length between the electrodes, A is the area of the electrodes, and R the resistance of the composite panel. The contact resistance that arises from imperfect bonding between the electrodes and the sample surface is a significant drawback of the two-probe method. Therefore, the resistances measured in this way include the resistances of the meter, electrodes, and the wires as well as the contact resistance due to imperfect bonding. The resistance of modern high-resolution multimeters is generally negligible. The electrodes are made of metal and their resistance is also negligible. However, the contact resistance cannot be accounted for and is a large source of uncertainty. As discussed in the following section, an alternative approach for high-accuracy measurements is the four-probe setup.

2.9.1 Four-probe resistance measurements

For the four-probe method to be applicable, the current density between the electrode pairs used to measure the voltage should be uniform to ensure that the resistance follows Ohm's Law. As shown in Fig. 2–10, the four-probe method uses two electrodes pairs, one (outer) pair used for current injection and the other (inner) pair used for voltage measurements. The resistance – and thereby the conductivity – can then be calculated using Ohm's Law [30].

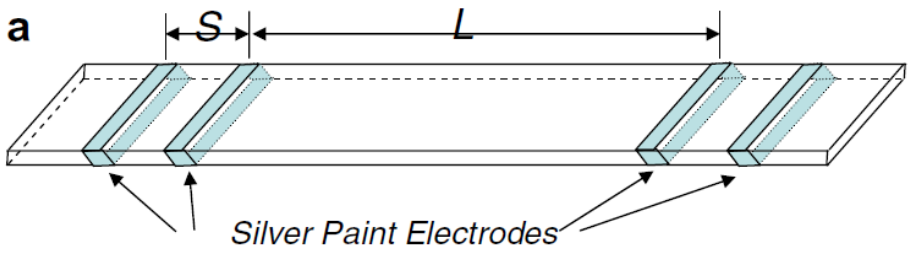

Fig. 2-10. Schematic of the four-probe method for electrical resistance measurements [30]

The four-probe method avoids contact resistance effects. The spacing between the electrodes has to be carefully adjusted to ensure a uniform current density between the voltage

electrodes. Indeed, measurements performed with a non-uniform current density are inaccurate.

2.9.2 Four-probe measurements of potential change

In this method, grounding one of the current-injection and one of the voltage-measurement electrodes allows the contact resistance to be calculated from the potential measured using the remaining voltage electrode.

Artificial neural network and normalised response surface techniques are based on the voltage change method. The voltage change method avoids the effects of contact resistance; however, the values obtained using this approach are dependent on the size of the investigated sample and are, therefore, specific to the particular composite panel under study.

2.9.3 Advantages of four-probe resistance measurements

Although problems can arise for anisotropic samples, the four-probe resistance method is preferable to the other aforementioned methods as the experimental protocol does not need to be adapted for particular composite samples. This approach can be used for composite panels whose material properties are known, whereas the values obtained with the voltage change method depend on the location of the current and voltage electrodes. As described in the previous section, the electrical response with the voltage change method varies from sample to sample. Four-probe resistance measurements are, therefore, preferable. Highly anisotropic samples are nonetheless problematic, even with this approach such that it is unclear when the four-probe method is valid and when it is not.

2.9.4 Multi-probe method

The multi-probe method follows the same principle as the four-probe method but now an array of electrodes is used on both sides of the composite panel, as shown in Fig. 2–11.

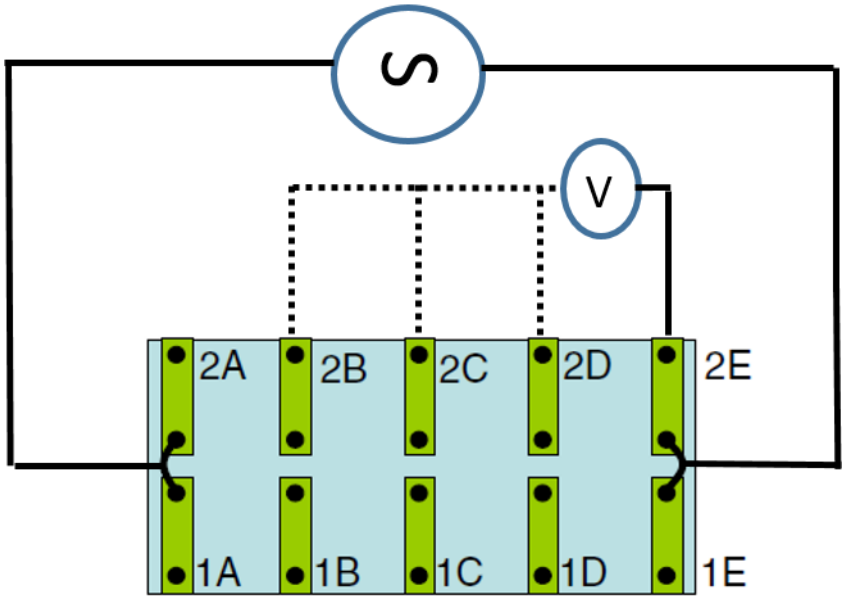

Fig. 2-11. Schematic of the multi-probe method for electrical resistance measurements [30]

A constant current is injected at electrodes 1A and 2A. The electrodes on one side are grounded (1E and 2E), and the potential is measured with respect to the grounded electrodes across all electrode pairs.

2.10 Electrical response of carbon-fibre-reinforced plastics under mechanical loading

Park et al. [31] have investigated the effects of tensile loading on single carbon fibres. The configuration used by these authors for their tests is shown in Fig. 2–12. The electrical resistance of isolated carbon fibres (in this case T700s-type fibres were used for the study) was measured using a digital multimeter. A direct electric current of 0.1 mA was generated and injected using electrodes connected through silver paste.

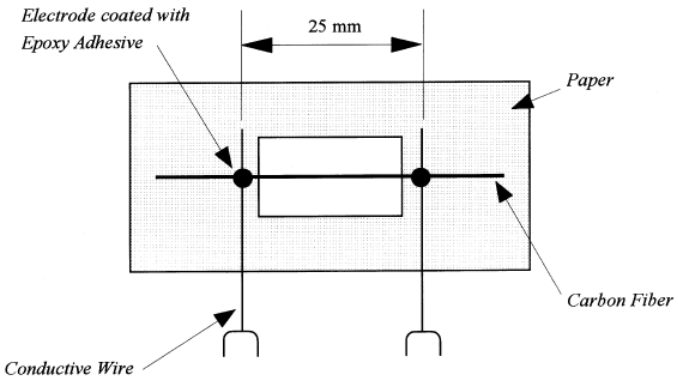

Fig. 2-12. Schematic of the experimental setup for the tests on single carbon fibres performed by Park et al. [31]

Using a crosshead speed of 0.05 mm/min, the resistance of the fibres was obtained as a function of the applied stress σ, and the initial resistance of the fibres R_0. The resistance, R, varied linearly with the strain up to the fracture point, according to:

$$\frac{\Delta R}{R_0} = \propto \frac{\sigma}{E} \tag{2-10}$$

Fig. 2–13 [31] shows that the resistance of the carbon fibres increases with the mechanical stress applied.

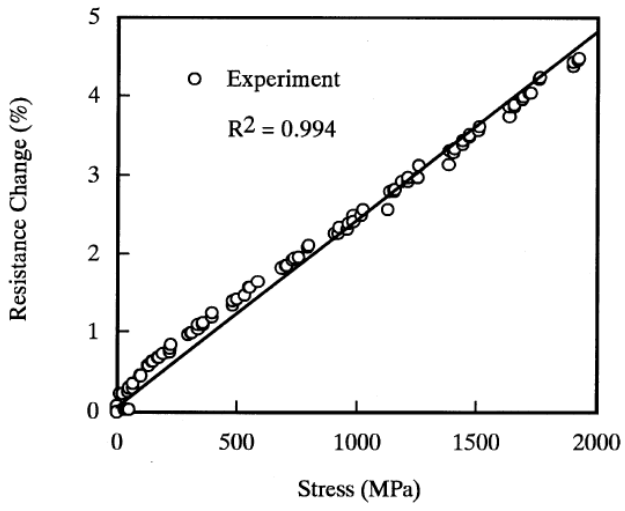

Fig. 2-13. Increase in electrical resistance of isolated T700s-type carbon fibres with the mechanical stress applied [31].

Conor and Owston [32] studied the electrical response of strained carbon fibres of different grades. The electrical resistance was found to vary among unstrained fibres of the same grade but of different diameters. Furthermore, the electrical resistance of the fibres was found to increase under strain, and for certain fibres, this change was permanent. The authors related this change to the degree of misorientation in the fibres. The same authors performed another investigation of isolated carbon fibres of different grades, this time involving electrical noise, which made measurement difficult, expressing the electrical resistance change as a function of the mechanical strain applied [33]. For most of the fibres, the resistance increased linearly with the strain for values above 0.1%. Interestingly, the authors noticed that the electrical response of certain fibres depended on the duration and rate of increase of the applied strain. To explain their results, the authors postulated that two conduction paths were available for the current in these samples, one direct and the other indirect. As illustrated in Fig. 2–14, the current flows directly between B1 and C1 (a direct path) but indirectly from B2 to C2 (an indirect path).

The longitudinal resistance of the fibre is characterised by the conduction through bonds C1 and B1, while the transverse resistance reflects the transfer of charge through bonds C2 and B2. The direct path offers the lowest resistance, whereas the indirect path has a comparatively high resistance because it is longer.

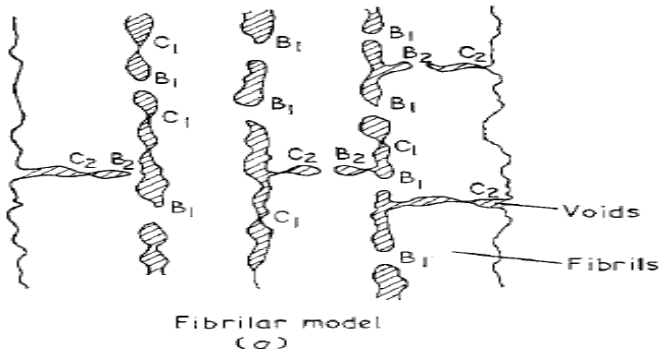

Fig. 2-14. Schematic model of electrical conduction paths in carbon fibres [33].

With reference to Fig. 2–14, if strain is applied to the fibre, bond B2 will be brought under tension, while shearing will occur at bond B1. In both cases, the electrical resistance will increase. The contact pressure on C2 will increase but the pressure on C1 will decrease. The contact resistance from the fibre extremities will also increase the overall resistance. The C2 bond is initially under pressure due to residual stress from neighbouring fibres. It will open under strain, however, leading to further increase of the electric resistance. Since the conductivity of CFRPs reflects that of the constituent carbon fibres, this applies to the electrical conductivity anisotropy of CFRPs.

In this work, M21/T800s-type carbon fibre composites similar to the material portrayed in Fig. 2–15, were imaged. The resin gaps do not affect current flow in the longitudinal direction but hinder flow in the transverse direction. The current takes the least resistant route by splitting into paths that differ according to the orientation of the fibre. Fig. 2–16 shows transmission electron microscopy images of the M21/T800s-type composite.

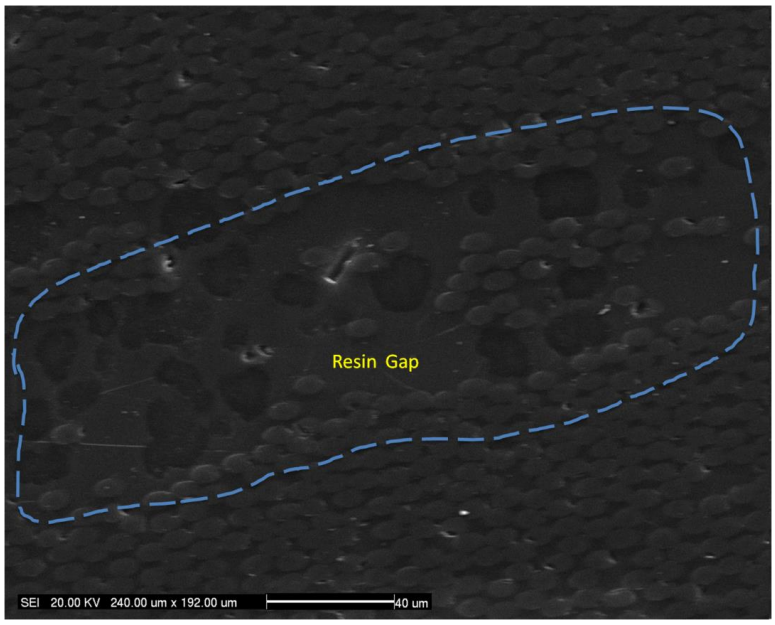

Fig. 2-15. Scanning electron micrograph of resin gaps in a M21/T800s-type composite.

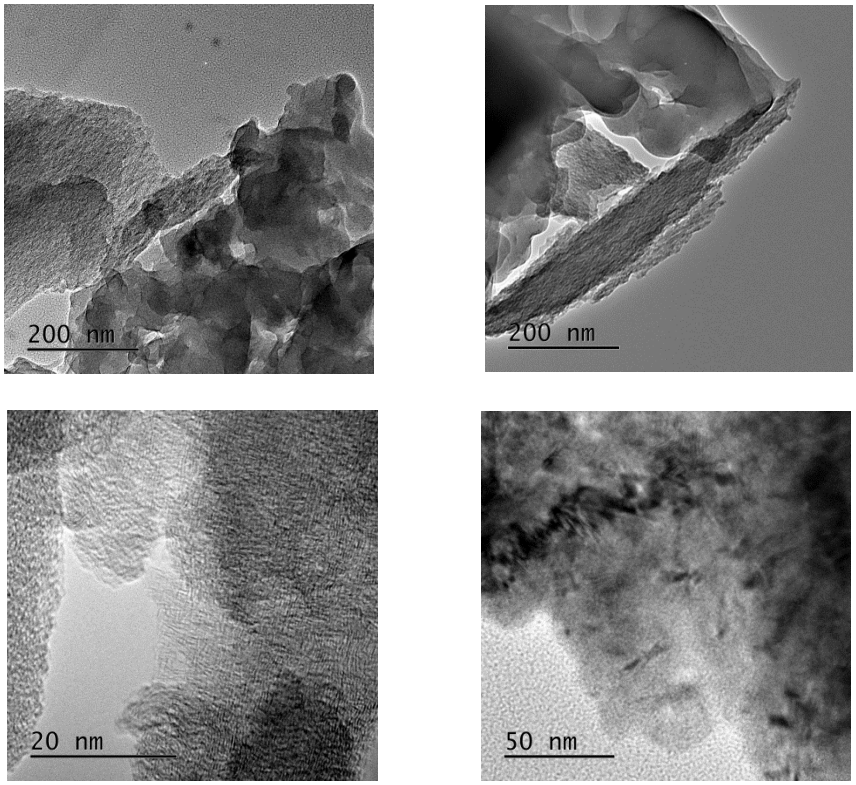

Fig. 2-16. Transmission electron micrographs of M21/T800s-type carbon fibres.

Owston [33] draws attention to the time dependence of the electrical resistance of carbon fibres, which is a result of their behaviour under mechanical strain. Mechanical strain tends to pull the fibres out of the composite, resulting in de-bonding with the polymer matrix and reduced fibre-fibre contact. This de-bonding propagates over time and is accelerated by heating, further lowering the contact level between fibres. As a consequence, the electrical resistance of carbon fibres under mechanical strain increases over time. The piezoresistance of carbon fibres is expressed in terms of the gauge factor (GF):

$$GF = \frac{\Delta R}{R_0 \varepsilon_L} \tag{2-11}$$

where R_0 is the resistance at zero strain and ΔR is the increase in the resistance resulting from an applied strain, ε_L. Eq. (2-11) describes the gauge factor arising from changes in resistance. The gauge factor due to geometrical deformations is given by:

$$GF = (1 + 2\vartheta) \tag{2-12}$$

The density of electrons per unit volume in a given material also affects its resistance under loading, such that [33]:

$$\frac{\Delta R}{R} = 2\varepsilon_{L+}{\varepsilon_L}^2 \tag{2-13}$$

Combining Eqs. (2-11) and (2-13) gives:

$$GF = 2 + \boldsymbol{\varepsilon_L} \tag{2-14}$$

The gauge factor, therefore, increases with the applied strain from a minimum value of 2. For carbon fibres, the gauge factor can be used to estimate their piezoresistance. In T300 carbon fibres with low elastic moduli, for example, the GF is typically between 2 and 3 for applied strains of 0.3–0.5% [34].

2.11 Electrical resistance to memorize maximum load

As described above, CFRPs consist of electrically conductive carbon fibres embedded in an insulating epoxy resin. Studying non-linear electrical responses in CFRPs under load can provide information on defects present in the composite or on any damage incurred. This information is extremely useful in the context of determining the maximum load that a CFRP panel in an aircraft can endure in flight. Indeed, the loading history of a CFRP panel can be estimated from residual electrical resistance measurements performed a posteriori on the panel [34].

These studies are also interesting in terms of improving the lightning resistance of composite panels. Measurements such as the ones described in this section can be used to detect damage caused by lightning strikes and to better understand the mechanisms through which the damage propagates to the rest of the aircraft structure. Electrical resistance measurements

could potentially be used for post-flight structural health monitoring of CFRP panels from aircrafts damaged in flight.

Various methodologies have been proposed in the literature to achieve this goal; however, most of these methods are analytical and focus on particular types of panels. The challenge is to develop a reliable and accurate methodology that is also generally applicable to any kind of composite panel.

The electrical response of CFRP panels can be studied both with and without loading. Indeed, because an aircraft is subjected to various types of loads during flight, each loading class must be applied separately to characterise the specific electrical response to that load.

The electrical response of individual carbon fibres in CFRPs is linear for all loads until the fracture point is reached. When a fibre breaks, the electrical response becomes stepwise. Hence, the electrical response depends strongly on any damage incurred by the CFRP structure. A pre-requisite, therefore, for studies of the electrical response of CFRPs is an in-depth understanding of the nature and the extent of damage therein.

In this context, it is worth clarifying why electrical resistance measurements are more useful post-analysis techniques than the sensors or mechanical approaches typically used for damage detection and to study the loading history. The main reason is economic, in that the mechanical techniques and sensors required are expensive both financially and in terms of the time needed to scan an entire aircraft. Furthermore, some of these approaches can only detect damage locally and not over an entire structure. In contrast, electrical resistance measurements make CFRPs ‘self-sensing’, that is, able to detect damage themselves. External techniques are thereby no longer required, saving both time and money. Currently, however, electrical resistance measurements are not reliable enough for online aircraft damage monitoring and additional studies and verifications are required.

Okuhara and Matsubara [35] have been developing a CRFP able to memorize its maximum strain level as quantified by the residual resistance from fibre fracture—this being irreversible. For the tensile tests performed in their study, the resistance returned to the initial value after unloading, highlighting inadequate strain retention in the CFRP studied. However, a pre-stressed composite was able to retain its resistance even under low levels of applied strain. The ability of the composite to memorize the maximum strain applied was also demonstrated via bending tests performed on a concrete beam incorporating the composite. The authors observed that the pre-stressed composite successfully memorised the crack mouth opening displacement even after the closure of the crack after unloading.

The anisotropy of CFRPs complicates electrical resistance measurements. As mentioned above, the electrical conductivity of CFRPs is high in the fibre direction but the cross-ply conductivity (i.e. in the transverse direction) is much lower as the current transits only through fibre-fibre contacts between adjacent plies. The conductivity varies according to the composition and inner structure of the material in terms of the fibre/filler volume fraction and the ply angle of the different layers.

2.12 Mapping Electrical Conductivity using Electrical Resistance

Schueler et al. [36] show how mapping the electrical conductivity of damaged CFRPs can be used to detect holes in the sample. The method they propose involves comparing voltages at different electrodes recorded with and without holes in the samples and requires prior knowledge of the position and size of the hole. In the analytical model, the authors have developed their four-electrode detector (two for current injection and the other two to measure the voltage, see Fig. 2–17) and assuming infinite conductivity along the fibres, the transverse position of the hole is revealed as the probe is moved perpendicular to the fibre direction. As illustrated in Fig. 2–17, a voltage increase in the hole-containing sample across

any pair of electrodes indicates that the hole (or some portion of it) is situated within the studied area between the electrode pair.

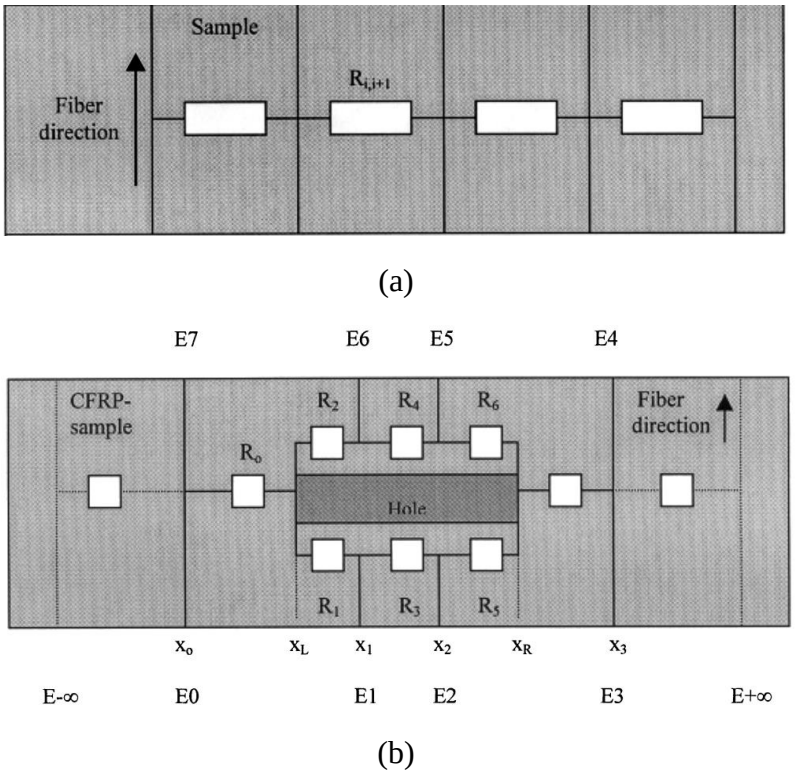

Fig. 2-17. Schematic outline of the method based on a resistor network model proposed by Schueler et al. [36] to detect holes in carbon-fibre-reinforced plastics (CFRPs), which involves comparing resistance measurements performed with a four-electrode setup on unidirectional CFPRs (a) undamaged and (b) with a hole.

The technique used by Schueler et al. [36] for damage detection in CFRP samples is known as electrical impedance tomography (EIT) and is commonly used in other domains, notably to study human skin and oil-bearing rocks.

2.13 Effect of Mechanical Load on Electrical Resistance

Ogi et al. [37] have developed interesting models to predict the resistance and piezoresistance of CFRPs under mechanical loading at different temperatures. The models take as inputs the initial gauge factor and the temperature coefficients, expressed as functions of the off-axis

angle. The resulting resistances and piezoresistances agreed well with experimental data. In particular, negative values for the temperature coefficients were obtained, likely as a result of contact resistance in the fibres.

Wang and Chung [38] discuss the need to sense strain during dynamic loading. The authors explain the key difference between strain and damage sensing, namely that the first is reversible and should, therefore, be sensed in real time, while the latter is not and can be detected a posteriori. Placing strain sensors inside the composite degrades its mechanical strength. Therefore, Wang and Chung [38] suggest using the electrical resistance of CFRPs to self-sense strain. As illustrated in Fig. 2–18, the electrical resistance of CFRPs increases under strain owing to reduced fibre-fibre contact.

In contrast, Wang and Chung [38] present a new electromechanical effect whereby the longitudinal resistance decreases and the transverse resistance increases due to longitudinal tension, which produces better aligned fibres and thereby more fibre-fibre contacts. In their study [38], the strain sensitivity of the fibres was high, as quantified gauge factors were in the range of 34–49. Reversing the longitudinal tension also reversed the effect on the resistance. The longitudinal and transverse resistance decreased irreversibly after the first loading cycle because of the irreversible decrease in the degree of alignment of the fibres.

Prasse et al. [39] simultaneously monitored the electrical resistance and acoustic emissions of 16-ply CFRPs that are 25-mm thick and 200-mm long. The electrical resistance was measured using the four-probe method—using pairs of evaporated gold electrodes 10 mm in diameter—and recorded using an impedance analyser (HP 4824A). The acoustic emissions of the samples were measured using a piezo sensor that was attached to the composite and connected to an acoustic emission analyser (LOCAN 320). The experimental setup is shown in Fig. 2–19.

Tensile loads were applied cyclically (two blocks of five cycles) using an MTS 810 machine at a crosshead speed of 1 mm/min. Fig. 2–20 shows the resistance-strain behaviour during the first cycle. The authors report that loading damaged the composite primarily through matrix deformation, cracking, and fibre-matrix debonding [39].

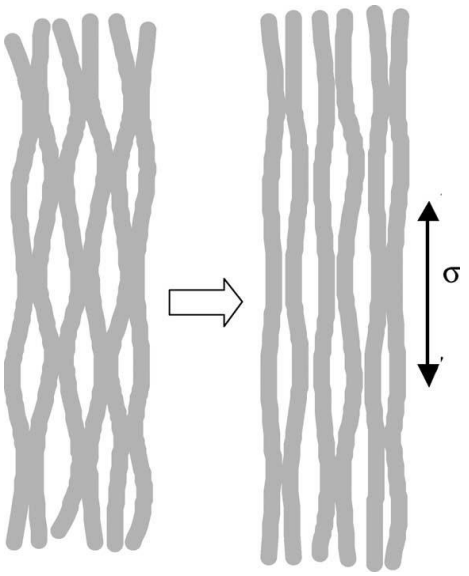

Fig. 2-18. Schematic illustration of the loss of fibre-fibre contacts due to strain [6].

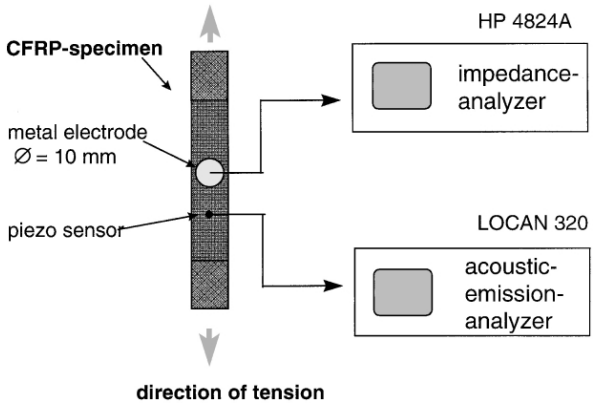

Fig. 2-19. Schematic of the experimental setup for the simultaneous monitoring of the electric resistance and acoustic emissions of a carbon-fibre-reinforced plastic (CFRP) sample under tensile loading [39].

Because loading leads to irreversible damage, when unloaded, the resistance of the studied CFRP was greater than prior to loading. The second block of loading cycles lead to additional irreversible damage. However, whereas the electrical resistance increased after unloading, it decreased under reloading due to formation of new fibre-fibre contacts, the closing of cracks, and the recovery of the electrical network. The authors concluded that the main factors influencing the electrical response of the composite were fibre rupture, the opening and closing of fibre-fibre contacts, the temperature, and most importantly, fibre strain.

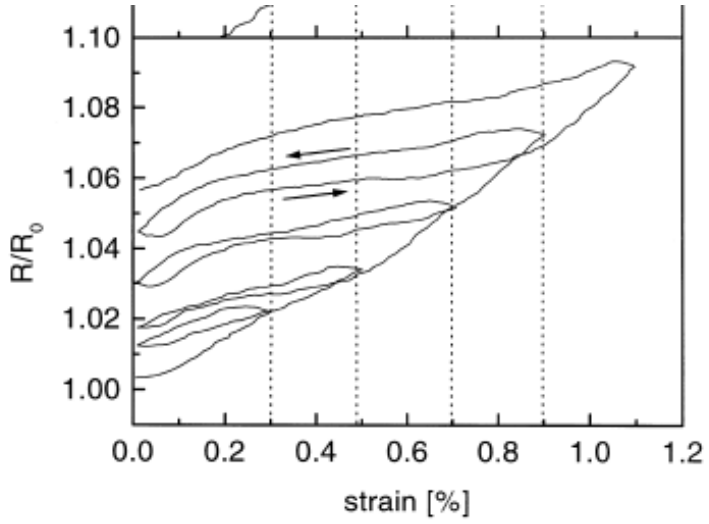

Fig.2-20. Resistance versus strain behaviour reported by Prasse et al. [39] for a cross-ply carbon-fibre-reinforced plastic under tensile loading.

The method used by Prasse et al. [39] could be used to differentiate between CFRP panels stressed for the first time and those previously submitted to strain. Indeed, the previous maximum load could be determined from a characteristic change in the measured resistance-strain curve.

2.1 Electrical resistance as a damage monitoring tool

Curtin has studied many of the features of CFRPs that are of interest to this study, notably their anisotropic resistance with and without damage, from fatigue in particular [40]. These findings can be used to predict the durability and lifetime of CFRP components in aircraft.

Curtin and his collaborators developed various analytical models of the anisotropic electrical resistance of aligned but randomly touching fibres in a three-dimensional array. The predictions compare well with numerical data (Fig. 2–21). The new parameter they introduce, the fibre contact density, $\frac{\beta\delta_{ce}}{L}$, is the ratio of the fibre-fibre contact density and electrical ineffective length of the material, δ_{ce}, and therefore allows the transverse resistance to be expressed as a function of basic material properties, which was not possible prior to this pivotal work. Curtin demonstrates [40] how these models can be used to determine the density of internal fibre-fibre electrical contacts from measured longitudinal and transverse resistances.

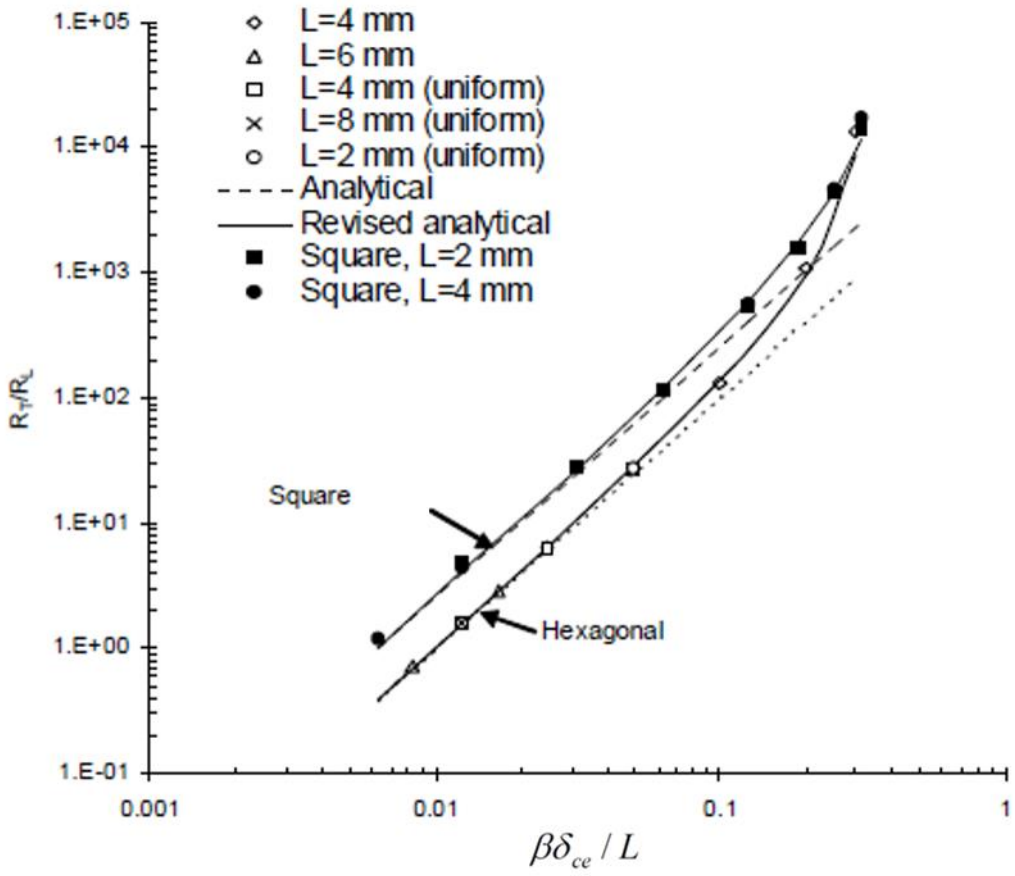

Fig. 2-21. Transverse to longitudinal resistance ratio as a function of the normalised fibre contact density parameter for undamaged composites with two different fibre array types [40].

After studying the anisotropic resistance of undamaged composites, Curtin [40] developed numerical models to predict the variation of the electrical resistance of the composites under mechanical loading as the fibres become damaged, concluding that the transverse and longitudinal resistances vary as a function of strain with the same functional form. Again, the models are in good agreement with simulated data (Fig. 2–22), with different fibre-fibre contact distributions observed. The spread in the numerical data results from variations in the damage parameter, ξ, which is approximately 1.5 for longitudinal damage and 0.96 for transverse damage [40].

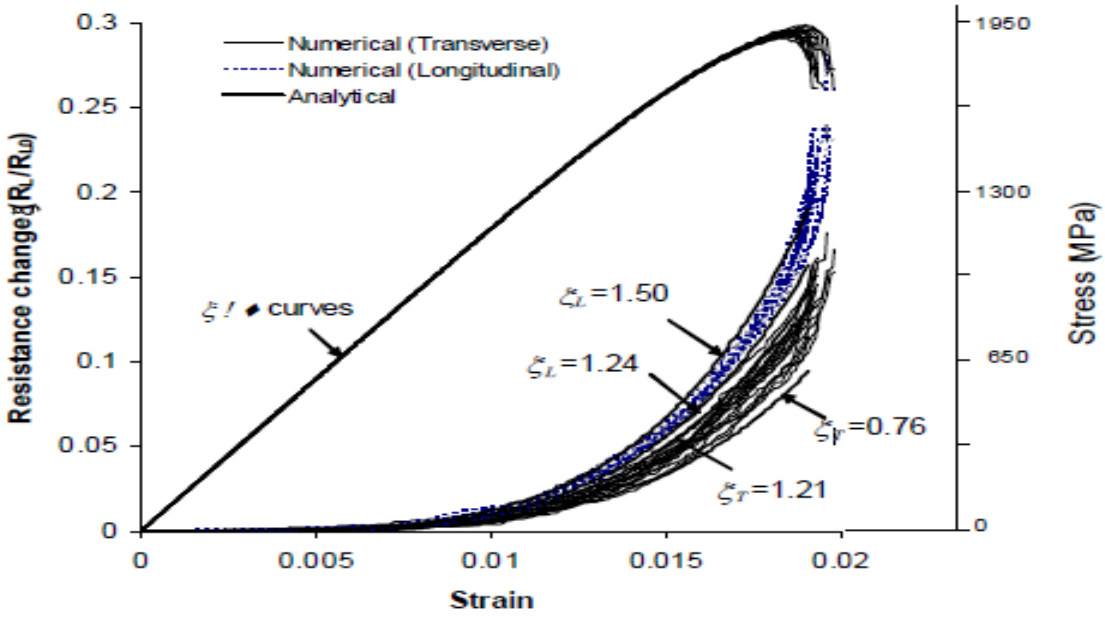

Fig. 2-22. Comparison of analytical and simulated data for the change in longitudinal and transverse resistance under loading for 30 different random fibre-fibre contact distributions [40].

Curtin went on to investigate the reliability of measured electrical resistances for predicting the current damage state and the remaining strength of the material [40]. He used the Weibull statistical probability distribution function to describe the electrical resistance as a function of the applied strain. For longitudinal resistance, the Weibull modulus increases as the CFRP samples approach the end of their lifetimes, suggesting that the damage and strength

estimates obtained in this way are accurate. For the transverse resistance, however, Curtin noted that the estimates are less reliable, as illustrated in Fig. 2–23.

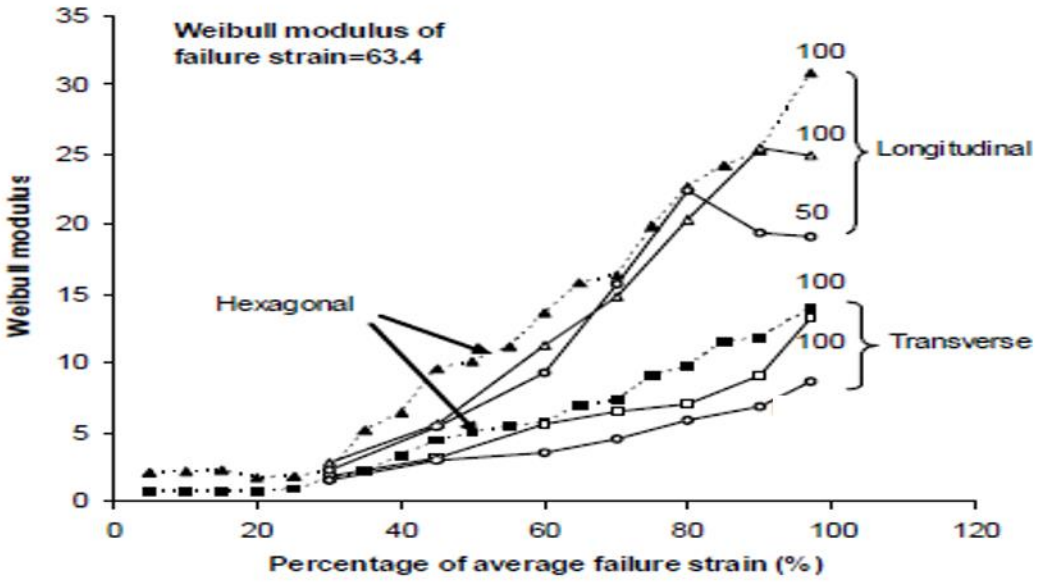

Fig. 2-23. Weibull moduli of the longitudinal and transverse resistance distributions as a function of the applied strain [40].

In the same report, Curtin also predicts the electrical resistance response to damage under fatigue loading, modelling the latter using Paris' law. Curtin concludes that underlying fatigue crack growth is due to pre-existing fibre flaws. The numerical model developed in this study was verified against experimental data for the fatigue of T700s carbon fibres, successfully predicting the correlation between changes in resistance and stiffness. Fig. 2–24 demonstrates the good agreement between the model-predicted longitudinal resistance and the values simulated numerically for the constant-amplitude loading at different strains of materials with different densities of internal fibre contacts.

The remaining strength (fatigue lifetime) of CFRP structures and panels can be estimated as proposed by Curtin [40]. Fig. 2–25 highlights the inverse correlation predicted between the fatigue lifetime and the change in resistance measured for the composite.

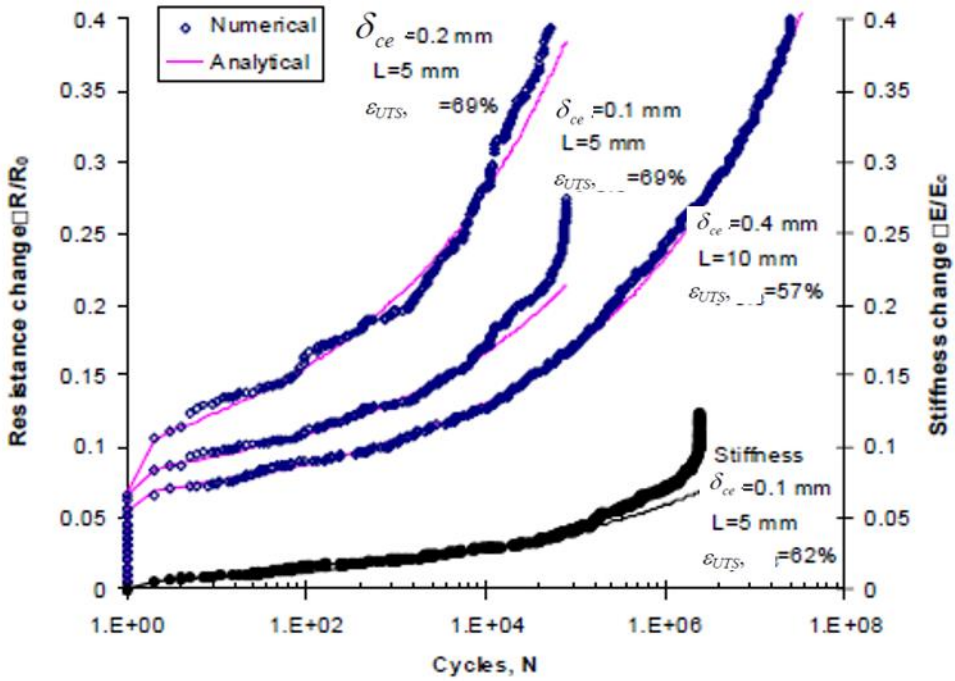

Fig. 2-24. Comparison of numerical and analytical data for the change in longitudinal resistance under loading as a function of the number of loading cycles, for composite materials with properties as indicated on the figure [40].

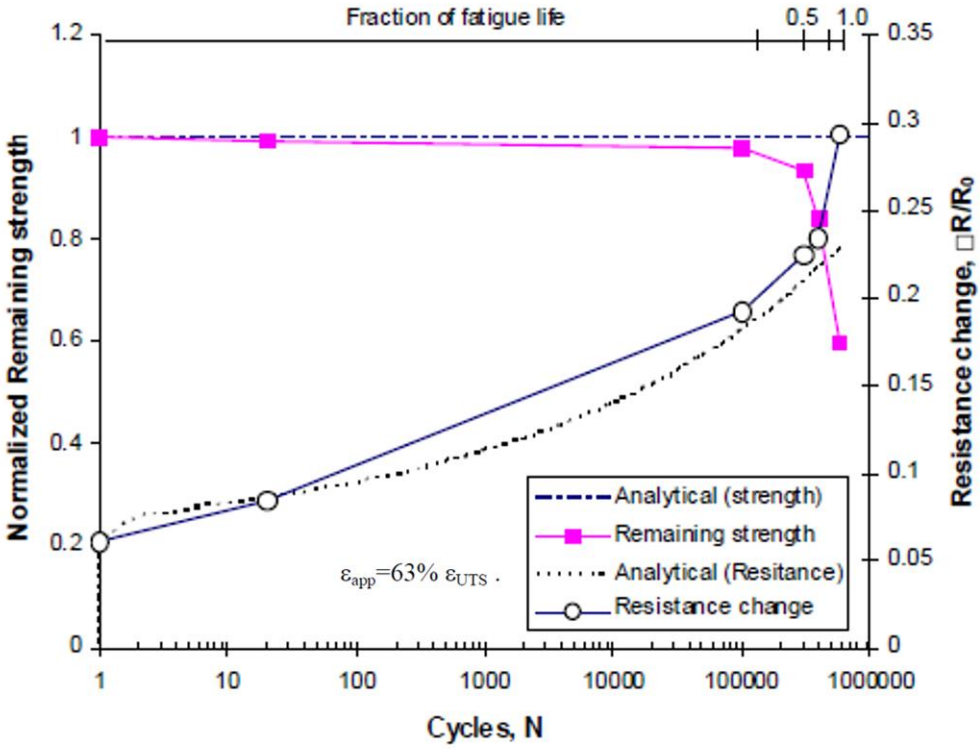

Fig. 2-25. Analytical models of the remaining strength of carbon-reinforced-plastic samples and their corresponding change in resistance under loading, versus the number of cycles for an applied strain at 63% of the ultimate tensile strength [40].

Based on the above discussion of the literature, electrical resistance measurements appear promising for damage detection and strain monitoring in CFRP structures and panels. The measurements can be applied in various ways, notably to estimate the maximum load experienced by a structure during previous loading cycles, and to detect and classify the damage incurred by CFRP structures.

2.2 Conclusions

This chapter has presented a review of the literature on carbon fibre composites and electrical characterisation methods, focusing on two- and four-probe methods used to characterise the behaviour of materials under mechanical strain. For the approaches envisaged for this study of CFRPs, the four-probe method is the setup that avoids errors arising from the resistance of the measuring device.

Numerous, theoretical, experimental, and computational studies have been performed over the past decade. This extensive review of the literature reveals that fatigue damage and the associated lifetime of the material can be correlated to electrical resistance measurements, which can also be used to estimate the prior loading history of a given sample. The literature on the use of electrical resistance as a damage assessment tool was also discussed. The electrical resistance approach is not only more cost-effective than conventional methods, it is also the only technique that allows the strain to be monitored in real time, which is clearly preferable to simple damage monitoring.

Following this review of the literature, the behaviour of carbon fibres under load, and the mechanisms of electrical conduction therein, Chapter 3 presents numerical models of the conduction processes within CFRPs based on the concepts developed in this chapter.

Chapter 3

POTENTIAL AND CURRENT DISTRIBUTION IN CARBON COMPOSITE PANELS: NUMERICAL MODELLING AND LABORATORY TESTS

3.1 Background

According to Scientific American, every commercial aircraft is hit by lightning once per year on average. A standardized lightning current waveform is shown in Fig. 3–1. The waveform consists of four components. Component A is the initial stroke with a peak current of 200 kA and a duration of approximately 500 μs. Component B is the intermediate stroke with a current of 2 kA that lasts for a few milliseconds. Component C is relatively long, with charge being transferred at 200–800 A for 0.25–1 s. Finally, component D consists of a sharp current increase and a short restrike at 100 kA.

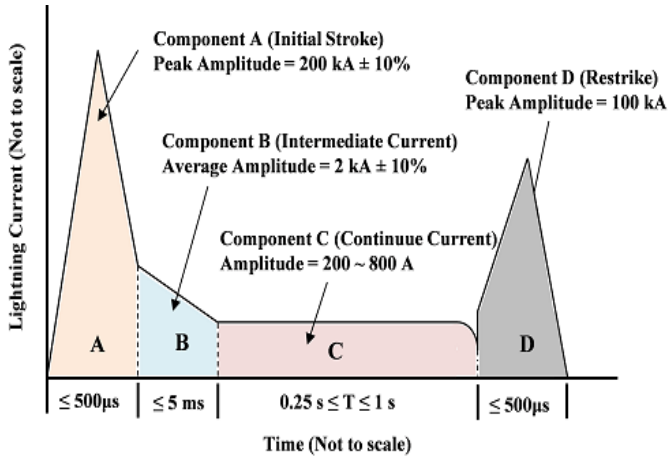

Fig. 3-1. Current vs. time profile of an idealised lightning current waveform [41].

Lightning has both direct and indirect effects on aircraft. The direct effect is physical damage caused in the vicinity of the strike, namely the melting, puncturing, and splintering of the aircraft's skin [42]. The indirect effects stem from electrical interference between the lightning current and the aircraft's equipment [43]. Fig. 3-2 shows the areas of the aircraft in which the direct and indirect effects of lightning strikes are expected.

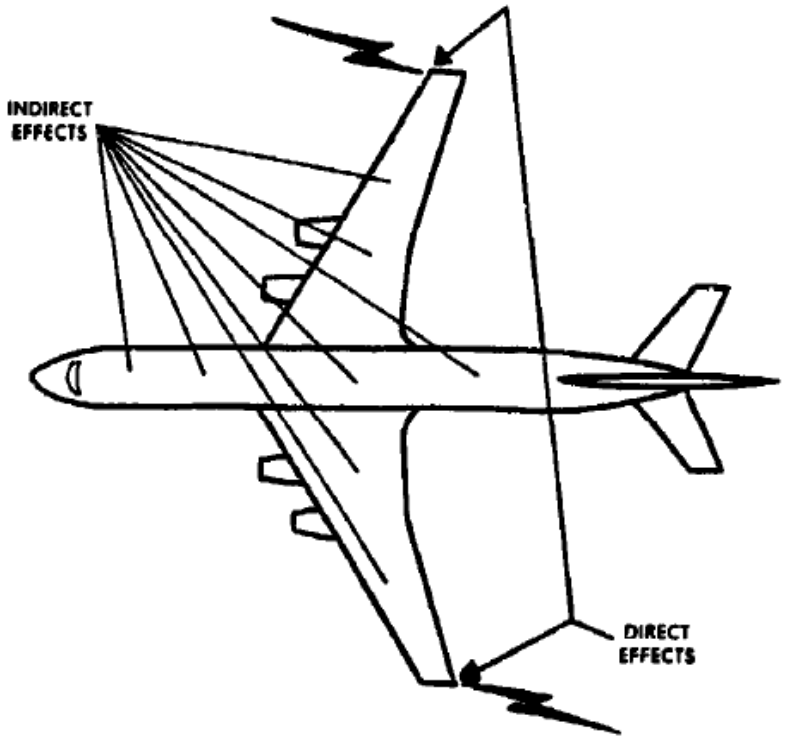

Fig. 3-2. Schematic showing the areas in which the direct and indirect effects of lightning strikes to aircrafts occur [42].

In the following sections, the direct and indirect effects of lightning strikes on metallic and non-metallic aircraft structures and components are discussed.

The use of fibre-reinforced plastics in aircraft components and the use of solid state components in the electrical power systems—two recent advances in aircraft design—both make lightning strikes more hazardous [42]. Fibre-reinforced plastics are used instead of

conventional materials because of their higher strength to weight ratio. However, they are less effective electromagnetic shields. The risk of induced voltages in the electronic wiring of aircraft with CFRPs components is, therefore, higher. Furthermore, solid state components in electric power systems are more susceptible to the indirect effects of lightning strikes such as transient overvoltages. It is very important to be aware of which aircraft parts are most susceptible to lightning strikes. Therefore, the aircraft is divided into different zones [44], which is discussed in the following section.

3.2 Lightning attachment zones

Defining lightning zones on aircraft is useful to ensure full protection from direct and indirect lightning effects. The different zones are listed in Table 3–1 alongside the different current and voltage waveforms that affect them.

Phillpot [46] defines the different lightning strike zones of an aircraft as follows:

Zone 1: Areas on the surface of the aircraft where the probability of the initial lightning strike is the highest, including its entry and exit locations. The surfaces in zone 1 also carry current to zone 3.

Zone 2: Areas on the surface of the aircraft where current from the initial strike is most likely to be swept. The surfaces in zone 2 also carry current to zone 3.

Zone 3: Areas on the surface of the aircraft not in zones 1 or 2. These areas can nonetheless carry substantial lightning currents through direct conduction between the attachment points.

Furthermore, as described in [46], zones 1 and 2 are further divided into regions A and B, where the probability is respectively low and high for the lightning arc to remain attached, as described below.

Zone 1A: Areas on the surface of the aircraft where the probability is low that a flash remains at its initial attachment point. Typical examples include protruding nacelles and leading edges.

Zone 1B: Areas on the surface of the aircraft where the probability is high that a flash remains at its initial attachment point. These include wing tips, the tail, and some trailing edges.

Zone 2A: The swept stroke zone in which the probability of a flash remaining attached is low, i.e. the mid-chord regions of wing surfaces that are aft of an engine.

Zone 2B: The swept stroke zone in which the probability of a flash remaining attached is high, i.e. the wing trailing edge aft of zone 1A.

The ED-84 report [47] also defines zone 1C as follows.

Zone 1C: The transition zone for the first return stroke. Areas on the surface of the aircraft where a reduced-amplitude return stroke is most likely to occur during lightning channel attachment, with a low probability of a flash remaining attached.

These zones are depicted for a transport aircraft in Fig. 3–3.

Table 3-1. Aircraft lightning zones and the voltage and current waveforms that affect them [45].

Aircraft Zone	Voltage Waveform(s)	Current Component(s)
1A	A, B, and D	A, B
1B	A, B, and D	A, B, C, D
1C	A	B, D
2A	A	D, B
2B	A	D, B, C
3		A, B, C, D
Lightning Strike Model Tests	C	

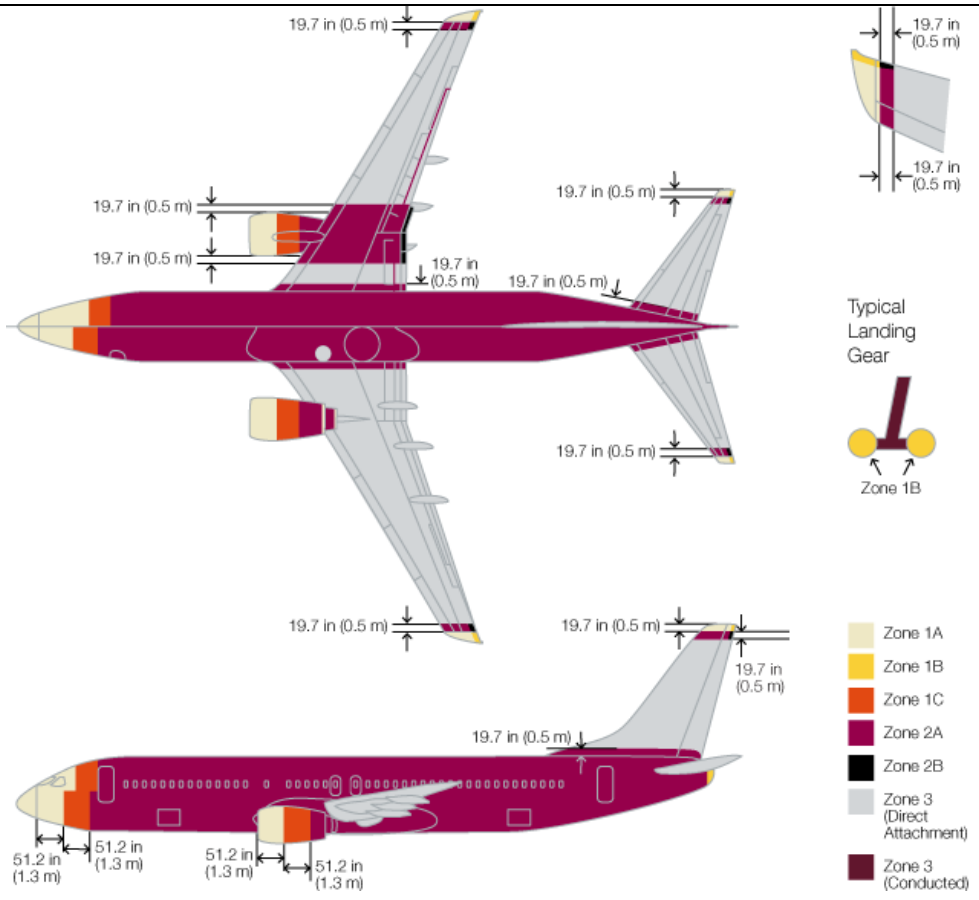

Fig. 3-3. Schematic showing lightning strike zones on a transport aircraft [48].

Approximately 90% of lightning discharges to an aircraft are initiated by the aircraft itself [49]. According to Uman and Rakov [49], these flashes occur at an altitude of 5-6 km in summer under normal electric field and atmospheric current flow conditions. The authors [49] estimate that the resulting damage can be so severe as to lead to the destruction of the aircraft, although such events are not common. Furthermore, the authors draw attention to two major lightning incidents initiated by large rockets launched from Earth: the Saturn V vehicle of NASA's Apollo 12, which completed its mission, and the US Air Force's Atlas-Centaur 67, which was damaged. Chapter 5 discusses in detail the types of damage that carbon fibre composite parts and structures can suffer because of lightning.

3.3 Direct effects of lightning on aircraft

All-metal (typically aluminium) aircraft suffer less damage from lightning strikes (relative to carbon fibre materials) due to the high electrical conductivity of their (metal) components, which ensure that the lightning current is efficiently dissipated. Nonetheless, lightning has been reported to cause pitting and melting, deformation due to magnetic fields, resistive heating, pitting at structural interfaces, shock waves, and overpressure in all-metal aircraft [42].

Pitting and melting through holes occurs for aircraft skins with a thickness of 1 mm or less. However, at the trailing edge, the lightning channel may have a higher dwelling time and may cause melting even through thicker metal skins. Magnetic field damage is proportional to the duration of the current stroke and to the square of its amplitude. The damage induced may be understood using the basic laws of current flow. The wiring within a structure experiencing a lightning strike can indeed be represented by a series of parallel conductors that attract one another when current flows through them, resulting in the crimping of any

wires present. Resistive heating can also be damaging if the cross-sectional area of the wires used is too low to support the current flow.

Feraboli and Kawakami have compared samples impacted by drop weights (100 J) and by lightning (~kA) [50].

Larsson et al. [45] classify aircraft lightning strikes in two groups: those that are triggered by the aircraft (the most frequent) and those that occur when the aircraft intercepts a natural lightning channel. The ED-84 report defines the different direct and indirect effects of lightning [47]. Direct effects encompass the local physical effects of lightning strikes, namely dielectric puncturing, blasting, blending, melting, burning, and vaporising. On the other hand, damage is classed as indirect if it results from the temporary increase in voltage or current in the aircraft's electrical circuits or any other conductive components. The four voltage components of an idealised lightning strike waveform are depicted separately in Fig. 3–4.

3.4 Definition of Voltage Waveforms

In waveform A, the voltage increases at a rate of 1000 kV/μs (± 50%) until the test object is punctured. The voltage then decreases down to zero at an unknown rate. Voltage waveform B is the electrical industry standard for dielectric testing, namely a waveform with a rise time of 1.2 μs (± 20%) and a decay time to half amplitude of 50 μs (± 20%). The rise and decay times of this waveform are assumed not to be interrupted by the puncture or the flashover of the test object. Voltage waveform C is chopped, with breakdown occurring at 2 μs (± 50 μs). The magnitude of the voltage breakdown is unknown. Voltage waveform D rises between 50 μs and 250 μs, allowing time for streamers to develop in the test object. This waveform is expected to lead to higher strike rates in lower probability regions. Fig. 3–4 shows an idealised lightning current waveform in full, consisting of components A, B, C, D; multiple

stroke and multiple burst waveforms are also shown. A multiple stroke consists of components A and D/2, whereas the multiple burst waveform is a series of H components.

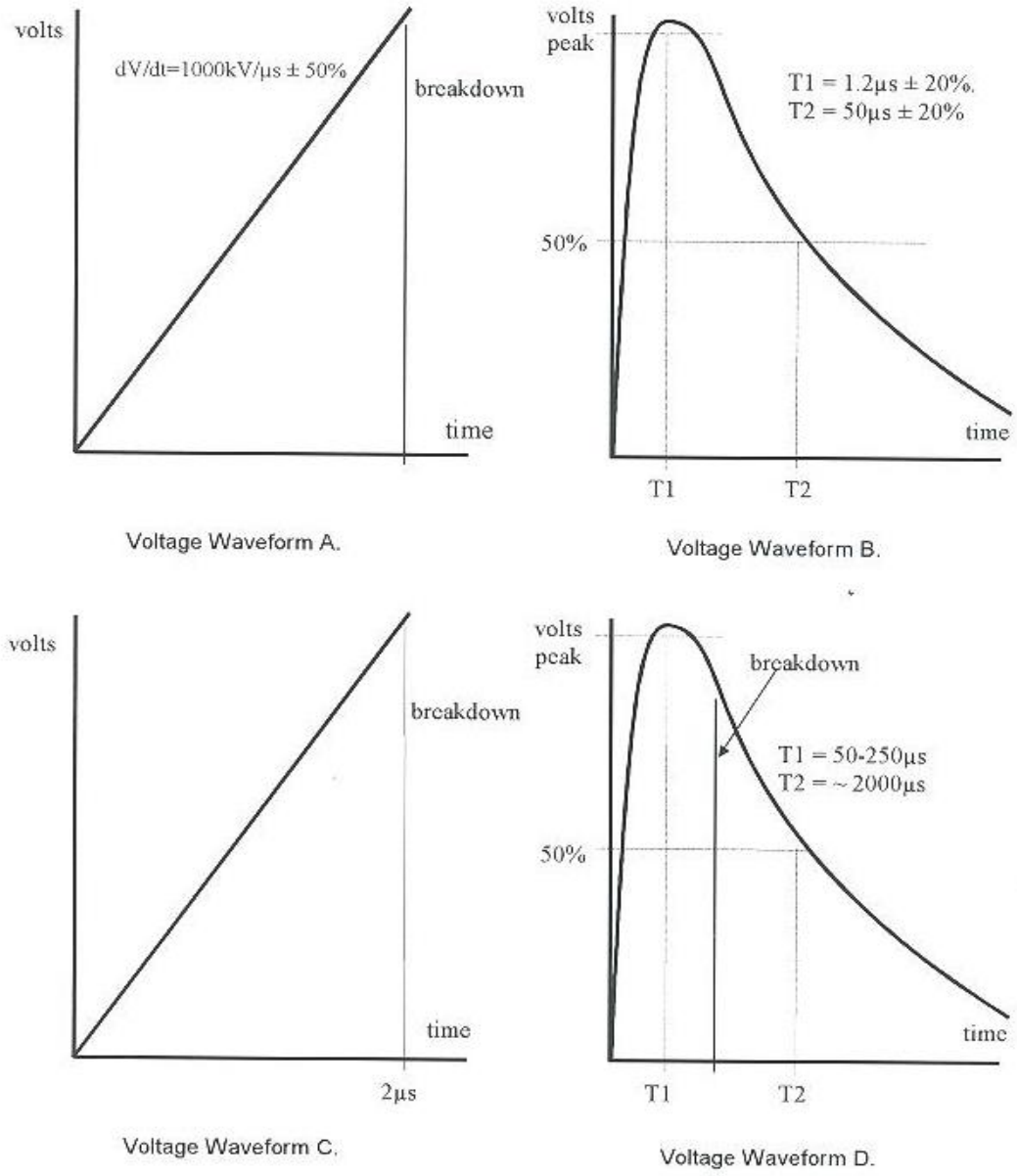

Fig. 3-4. Voltage waveform components for an idealised lightning strike [47].

All the components (A–D) can cause direct damage but only components A and D, with multiple stroke and multiple burst waveforms are involved in the indirect effects. Component A is associated with the initial strike and occurs more frequently in aircraft flying at lower altitudes. This component has high negative or positive first return stroke values. Component

B consists of current transfer at intermediate levels and to some initial negative return strokes and re-strikes. Component C involves extended current transfer and relatively low intensities, and is followed by re-strikes for negative cloud-to-ground lightning strikes and return strokes for positive cloud-to-ground lightning flashes. Although components B and C can be considered as current bridges between components A and D and have lower peak amplitudes, they transfer more charge in total.

3.5 Single-layered panel—numerical modelling

Simulations were performed for a square CFRP panel 2.2 m^2 in area and 0.25 m thick. Two aluminium electrodes were also simulated, one on the top surface to inject the lightning impulse and one on the bottom, which was grounded. Equipotentials were computed along with the current lines. The following lightning impulse was applied:

$$V(t) = 1000 * (e^{(-\propto t)} - e^{(-\beta t)}) \tag{3-1}$$

where

$$\propto = \frac{1}{68.2 \times 10^{-6}}\ s^{-1} \tag{3-2}$$

$$\beta = \frac{1}{0.402 \times 10^{-6}} s^{-1} \tag{3-3}$$

t=0.1e-9 to 50 e-6 s (time step=0.1μs) (3-4)

Fig. 3-5 shows the voltage profile of the applied lightning impulse as a function of time. Table 3-2 gives the electrical conductivity and relative permittivity of the simulated material and those of aluminium.

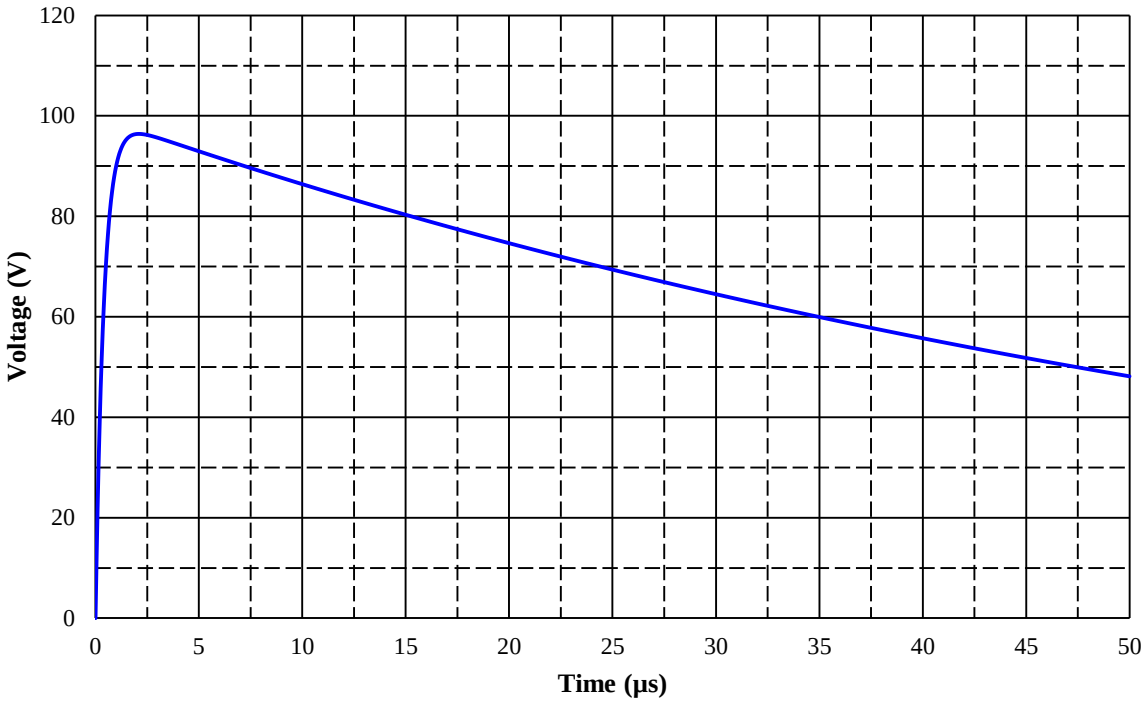

Fig. 3-5. Voltage vs. time profile of a lightning impulse.

Table 3-2. Properties of the simulated carbon-reinforced plastic compared with those of aluminium.

Material	Electrical Conductivity S/m $[\sigma_x, \sigma_y, \sigma_z]$	Relative Permittivity ε_r
CFRP	[2000,20,20]	1
Aluminium	3.447×10^7	1

The electrical conductivity tensor for the CFRP material characterises its anisotropy in this respect, with, as discussed in Chapter 2, a high electrical conductivity in the *x* direction (along the fibres), 100 times greater than that in the other two directions (across the fibres). The full anisotropic conductivity tensor is:

$$\sigma = \begin{pmatrix} 2000 & 0 & 0 \\ 0 & 20 & 0 \\ 0 & 0 & 20 \end{pmatrix} \tag{3-5}$$

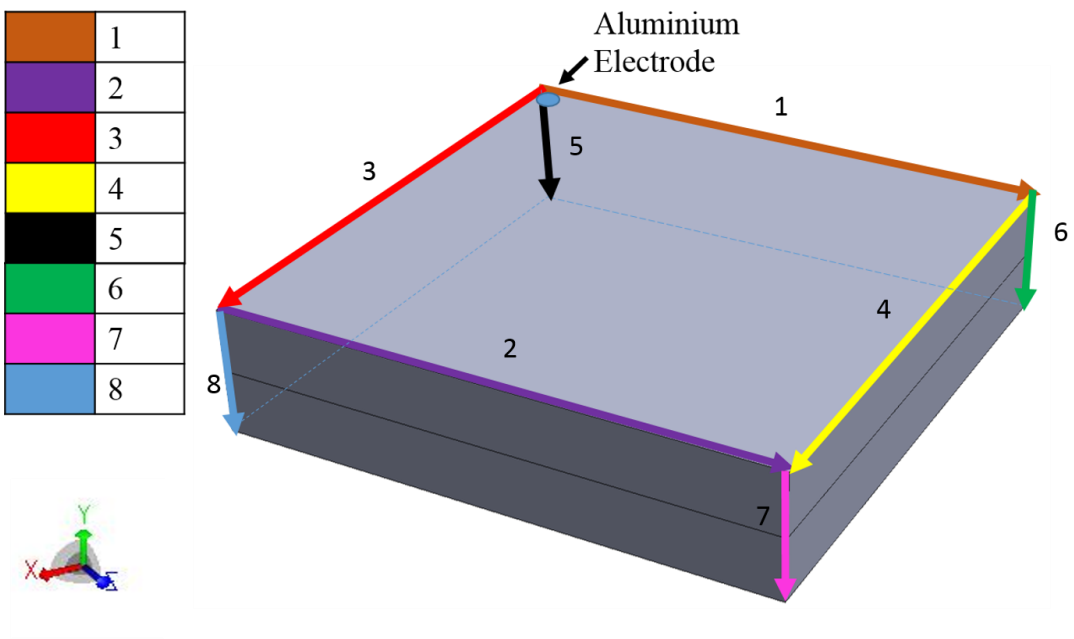

Fig. 3-6. Schematic illustration of the simulated one-quarter panel showing paths along which voltage profiles were computed

The geometric model used here to simulate single-layered CFRPs is shown in Fig. 3–6. Only one-quarter of the geometry was modelled because the problem is symmetric along the *x* and *y* axes.

The model was meshed using 4570 tetrahedral elements using the physics-controlled meshing option in COMSOL. The equipotentials were calculated during rise time, peak time, and fall time. For a time on the impulse front of approximately 0.5 µs, the voltage was approximately 700 V, with a similar value predicted for a fall time of 24.1 µs. However, for a peak time of 2.1 µs, the voltage was approximately 960 V. For each time interval, equipotentials were plotted at approximately 50% of the voltage level to investigate its arrangement and spread throughout the panel. The equipotentials were found to be most concentrated in the *x* direction, along which the electrical conductivity is highest, while the spread in the voltage was minimal in the other two directions, along which the conductivity is 100 times lower.

The voltage in the simulated panel, therefore, behaves as expected based on the electrical conductivity of the CFRP.

3.6 Modelling a two-layered panel

A two-layered panel was also modelled and simulated using the same material properties as described in Table 3-2. The dimensions of the panel were identical to the one shown in Fig. 3-6 except for the thickness, which was increased to 0.5 m because two 0.25 m layers were used. Again, two aluminium electrodes, one on top (lightning impulse injection point) and one on the bottom (grounded) of the panel were used. The top layer was oriented at 0°. For the bottom layer, the rotated coordinate system option in COMSOL was used to rotate the *x*-axis by 90°. COMSOL uses Euler angles to define the rotated coordinate system. For a 90° rotation, the Euler angle α is equal to $\pi/2$. A total of 8277 tetrahedral mesh elements were used for these simulations. A parametric study was performed to investigate the effects of decreasing electrical conductivity in the *y* and *z* directions, from 20 S/m down to 5 S/m. The shared equipotentials were found to occur at 50% of the instantaneous voltages. These equipotentials, described as 'twisting' [63] in some studies, are merely shared equipotentials that occur at 50% of the applied voltage, and demonstrate that the voltage inside the studied CFRP is distributed in a resistive manner.

As can be seen in Fig. 3-7 (a) with a maximal voltage at the electrode of ~700 V, the shared equipotentials indicate a voltage of 350 V; similarly, (see Fig. 3-7 (b)) with a peak time voltage maximum of 963 V, the shared equipotentials are at 481 V. These results indicate that the studied CFRP is reliably represented as a simple matrix of resistors, in agreement with the literature discussed in Chapter 2.

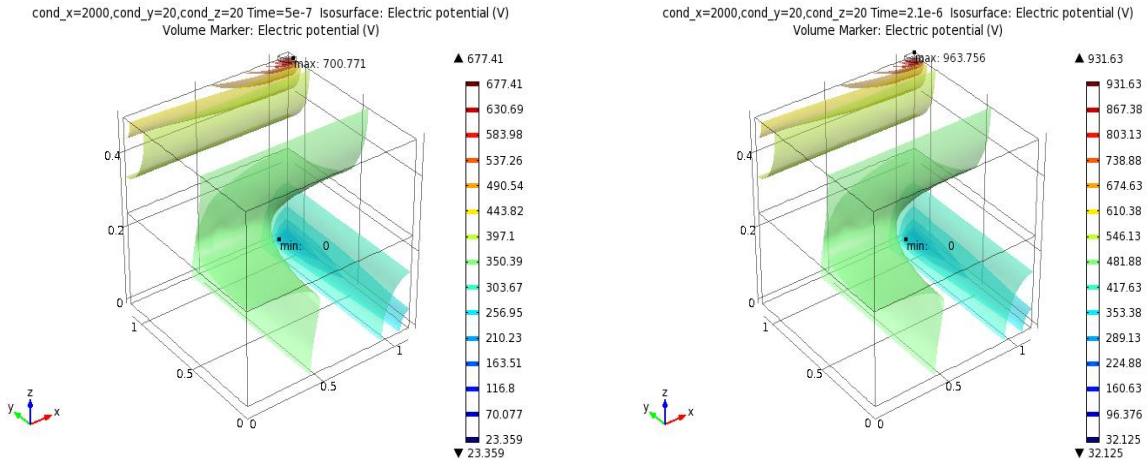

(a) shared equi-potential surface at 0.5 µs (b) shared equi-potential surface at 2.1 µs

Fig. 3-7. Simulated equipotentials in a quarter panel showing (a) shared equi-potential surface at 0.5 µs for two layered CFRP model and (b) shared equi-potential surface at 2.1 µs for two layered CFRP model

To verify the observations, a normalised voltage distribution was applied in the model along different edges such that the resulting graphs for the front, rise, and tail of the impulse coincided with each other. Along path 1, which starts at the lightning impulse injection point and runs across the surface of the electrode (see Fig. 3-6), the voltage decreases by about 50% from the maximum (see Fig. 3-8 (a)). For path 2, (see Fig. 3-8 (b)) the voltage decreases from approximately 70% to 30% of the maximum level from beginning to end. For path 3, (Fig. 3-8 (c)) which is similar to path 1, the voltage level starts at 1 on the electrode surface and decreases by approximately 50% moving away from the injection point. For path 4 as shown in Fig. 3-8(d) along the edge of the sample, the voltage level remains constant at ~50% of the maximum. Down path 5 in Fig. 3-8 (e), through the two layers of the modelled CFRP, the voltage decreases from 1 to 0.3. Similarly, for path 6 in Fig. 3-8(f), the voltage is 0.5 initially and decreases to 0.3 moving downward. For path 7 (see Fig. 3-8(g)), the voltage remains constant at 0.5. For path 8 in Fig. 3-8(h), on the opposite side of the sample from path 6, the voltage decreases from 0.7 to 0.3 V. The edge path voltages are crucial to understanding the effects of lightning strikes. These results suggest that, even at their edges,

the voltages experienced by carbon composites under lightning strikes are quite low, with the values recorded here varying from 1 V to 0.6 V.

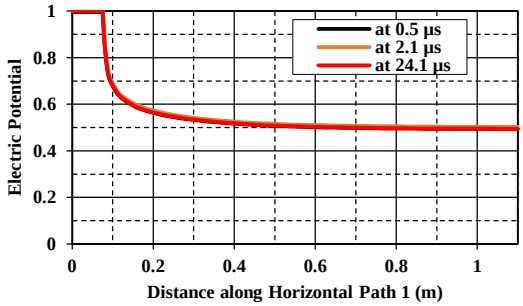

(a) Voltage Profile along Horizontal Path 1

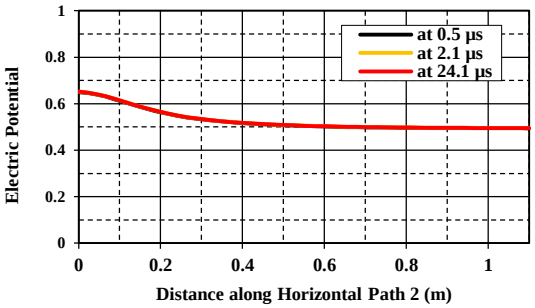

(b) Voltage Profile along Horizontal Path 2

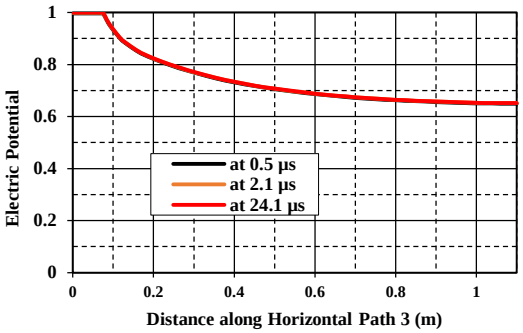

(c) Voltage Profile along Horizontal Path 3

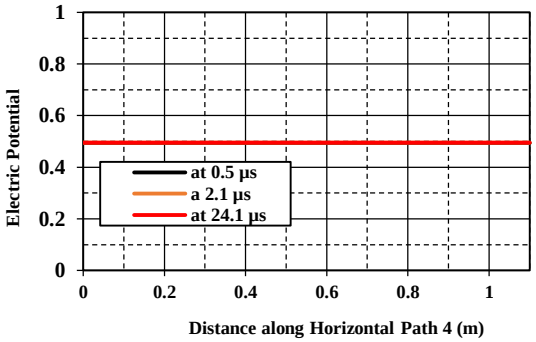

(d) Voltage Profile along Horizontal Path 4

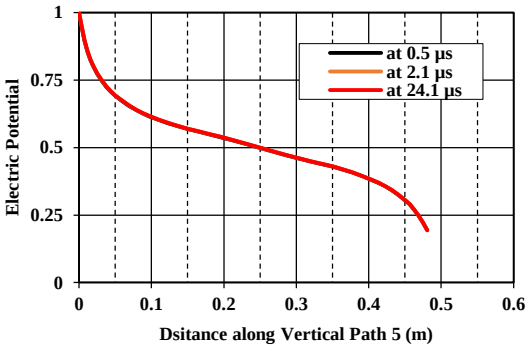

(e) Voltage Profile along Horizontal Path 5

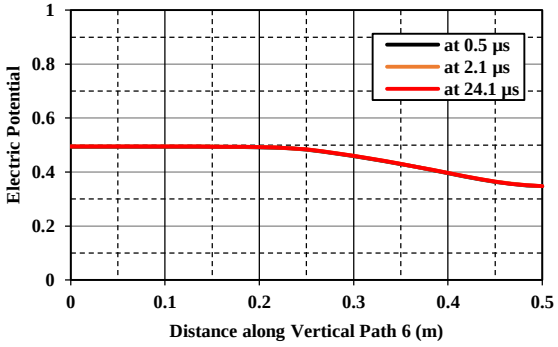

(f) Voltage Profile along Horizontal Path 6

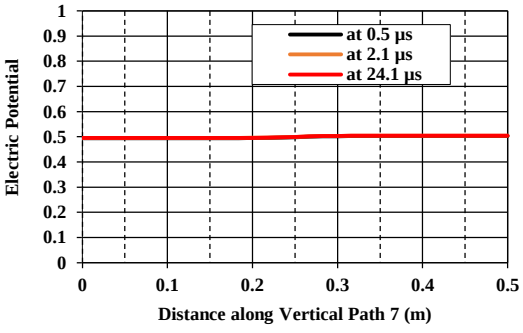

(g) Voltage Profile along Horizontal Path 7

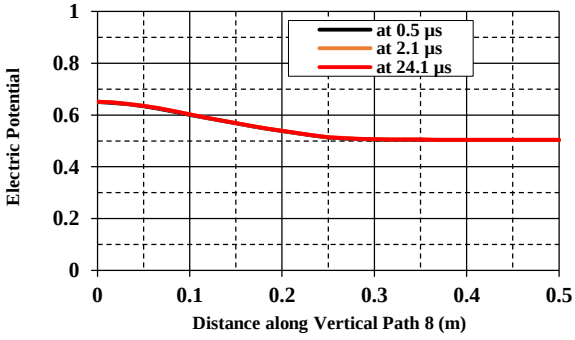

(h) Voltage Profile along Horizontal Path 8

Fig. 3-8. Voltage Profiles along paths 1-8 as shown in Fig. 3-6 for the simulated one quarter CFRP panel

3.7 Modelling the experimental panel structure

Structural experiments (see Section 3.9) were performed on flat, square (55 cm^2) CFRP panels as supplied by the aerospace industry and as represented in Fig. 3-12. One-quarter of a panel such as these was modelled. Instead of grounding the electrode fixed on the bottom surface of the panel, the entire aluminium frame, to which the panel was attached, was grounded. The top aluminium electrode was then used to inject the lightning impulse D with a magnitude and shape governed by Eq. (3-1). This configuration is more realistic than the one described in the previous section because it is representative of the actual experimental setup. The panel was 4.5 mm thick with 16 plies, and 40295 tetrahedral elements were used for meshing. Based on the results of the simulations for the two-layered panel, the panel was divided into two layers, each 2.25 mm thick.

The same normalised voltage profiles were obtained as those described in the preceding section, verifying that the voltage inside the actual test CFRP structure is distributed resistively. The model was then extended to encompass the whole CFRP structure since it cannot be assumed that the results obtained on one quarter of the sample are representative of the panel as a whole. Two such full-panel simulations were performed, with and without metal bolts inserted along the edges, in view of producing a more realistic model for larger panels, approximately one-half-metre long. As shown in Figs. 3–9 and 3–10, the shared equipotentials occur at 350 V, 50% of the maximum, and are concentrated in the four corners of the panel. Comparing these two figures also reveals the same shared equi-potentials as described for the quarter-panel.

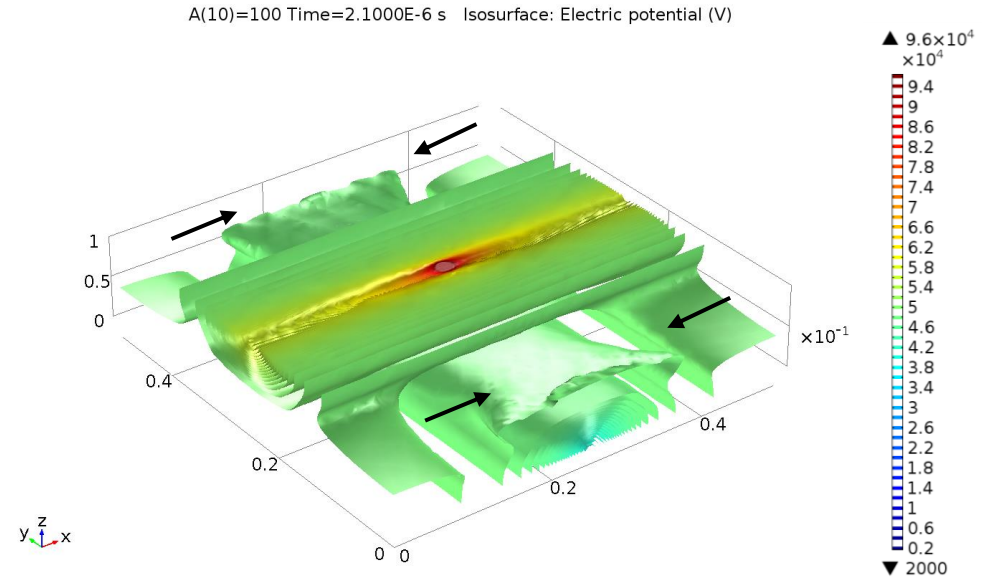

Fig. 3-9. Simulated isopotential surfaces at 2.1 µs over a full composite panel with arrows highlighting the contraction of equipotentials at its edges.

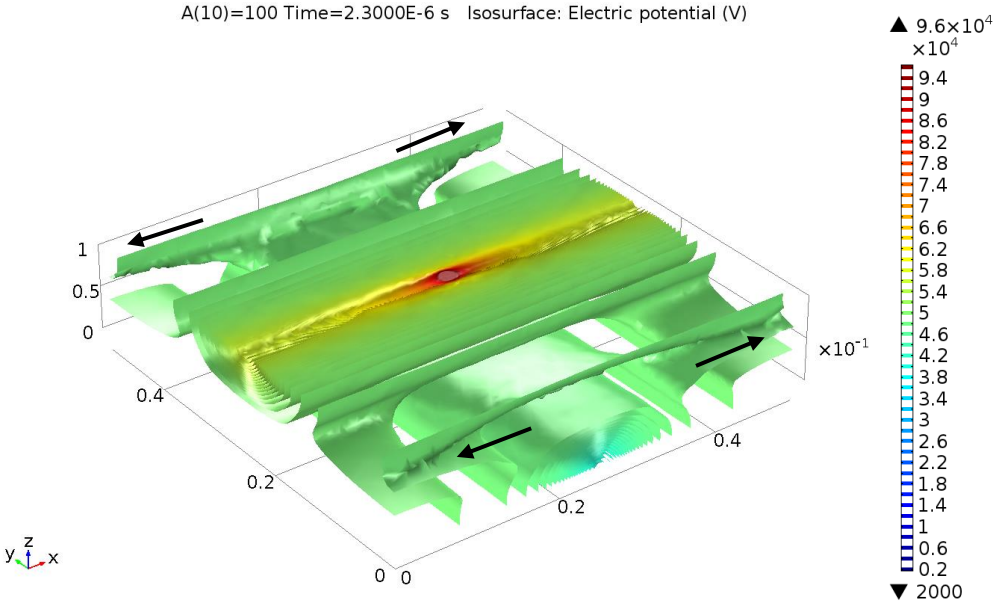

Fig. 3-10. Simulated isopotential surfaces at 2.3 µs over a full composite panel with arrows highlighting the expansion of equipotentials at its edges.

For simulations of the full panel (see Figs. 3–9 and 3–10), the equipotentials are at 350 V, which is exactly 50% of the potential at the injection electrode. The equipotentials at the edges contract just after the peak time (2.0 µs, see Fig. 3–9 at 2.1 µs) and expand at 2.3 µs (Fig. 3–10). Thereafter, the equipotentials move upwards towards the top layer, reversing

their direction of movement. However, during the rise to peak time, they move from the top to the bottom layer. The electrical conductivity values used for this simulation were obtained from [51]. A quarter-panel model cannot be used to estimate events in other parts of the same panel. Therefore, to extract the detail of events in a full panel, it is important to model the problem in its entirety using realistic geometry and boundary conditions.

The electrical conductivity values also differ in the two simulations performed; for one case, the transverse and through thickness conductivity are equal and, for the other case the values for transverse and through thickness conductivities vary from 165 S/m to 50 S/m. However, both simulations show existence of shared equipotentials.

3.8 Experimental studies of flat panels

The concept of shared equipotentials was verified experimentally using an infrared (IR) camera, Flir A325. As for the simulations, a direct current of 1 A was injected using silver electrodes painted on the top and bottom surfaces of the two-layered [0°,90°] composite panels. Fig. 3–11 shows the resulting current distribution on the surface of the panel. The sample was connected to the source using a top silver paint electrode and a thin flexible wire, another electrode at the bottom of the sample was used as the return electrode. The current spreads out initially from the middle of the top layer oriented at 0° before a shared equipotential is formed. This result demonstrates the resistive distribution of equipotentials in these two-layered carbon composite flat panels. Although the IR experiments were conducted with direct current injection, the patterns obtained are similar to those observed by simulation.

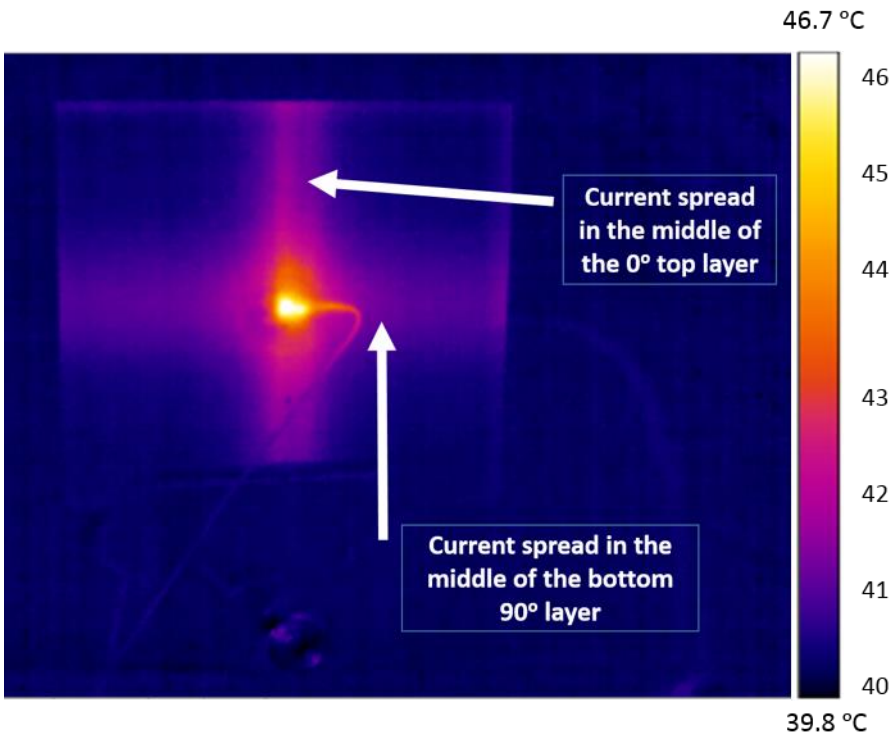

Fig. 3-11. Infrared thermograph of the shared equipotentials on the surface of a [0°, 90°] M21/T800s two-layered panel. The current injection point is located in the middle of the panel, as for the numerical model shown in Fig. 3-11 (I=1 A)

3.9 Simulations of lightning strikes

To accurately model the experimental tests performed in the Cardiff Morgan Botti Lightning Lab (MBLL) shown in Fig. 3–12(a), simulations were performed on thinner panels and with aluminium bolts on their edges (grounded through holes in the panel), as shown in Fig. 3–12(b). The model was solved using a supercomputer at the ARCAA of Cardiff University, initially for a two-layered panel with the bottom layer orientation varying from 0° to 180 °, and then for a multi-layered quasi-isotropic panel. The electrical conductivity properties used were [40000, 165, 50] S/m [51]. An electrode was placed in the centre of the panel to mimic the fuse wire used in the actual tests. The normalised potential distribution is presented herein along two horizontal paths, one diagonal and one vertical.

The normalised potential graphs along paths 1a, 2a, 3a, and 4a in Fig. 3–12 are shown in Fig. 3–13. Along all these paths, the potential distributions are nearly identical for different ply orientations, namely [0°], [0°, 90°], [0°, 45°], and [0°, 135°]. Figs. 3–13 and 3–14 show that, along paths 1a, 2a, and 4a, the voltage is maximum at the midpoint (where the current injection electrode is located) with the increase/decreases on either side mirroring each other.

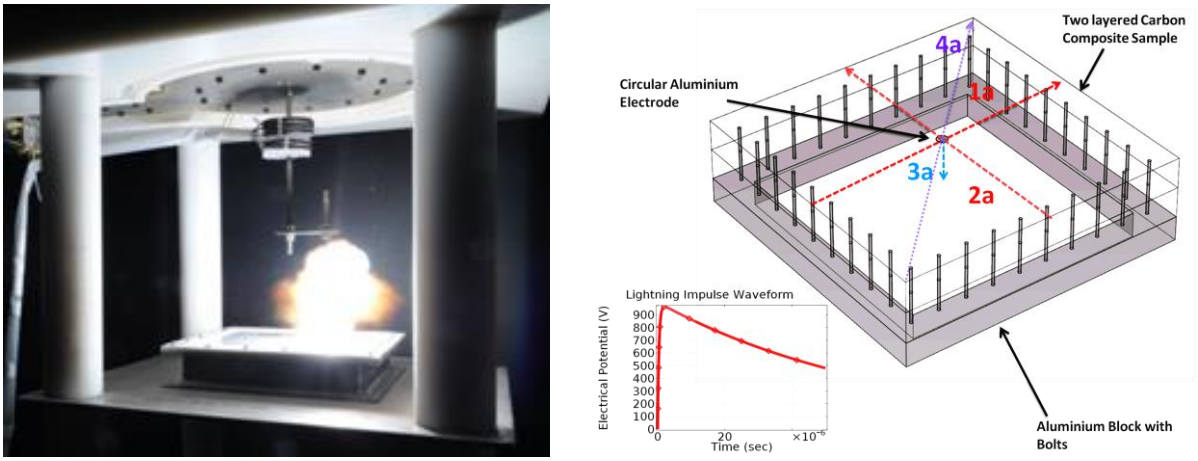

(a) (b)

Fig. 3-12. (a) Lightning chamber during a test in the Morgan Botti Lightning Lab at Cardiff University and (b) numerical model for the entire carbon-reinforced composite panel used to replicate the conditions therein.

Furthermore, it should be noted that carbon fibre pyrolysis in the composites, which occurs in practice, has not been investigated in this PhD thesis. Shared equipotentials are also found for quasi-isotropic lay-ups and cross-ply laminates. For different two-layered ply lay-ups, the shifts in the shared equipotentials occur at different locations. These models provide an estimate of electrical discharges on the edges of CFRP samples and are, therefore, useful for future studies of the edge glow phenomenon in such composites and the behaviour of the material under such extreme conditions.

The coinciding voltage profiles in Figs. 3–13 for paths 1a, 2a, and 4a (obtained for a full panel under actual testing conditions), show again that the potential distribution inside these carbon fibre composites is completely resistive. These simulations provide information about

the voltage distribution both on the surface of the panel and on its inside. The surface distribution, in particular, is key to understanding actual lightning events. Indeed, since during lightning strikes, the potential on the surface of CFRP panels may exceed 1 kV, simulations are required to understand their effects.

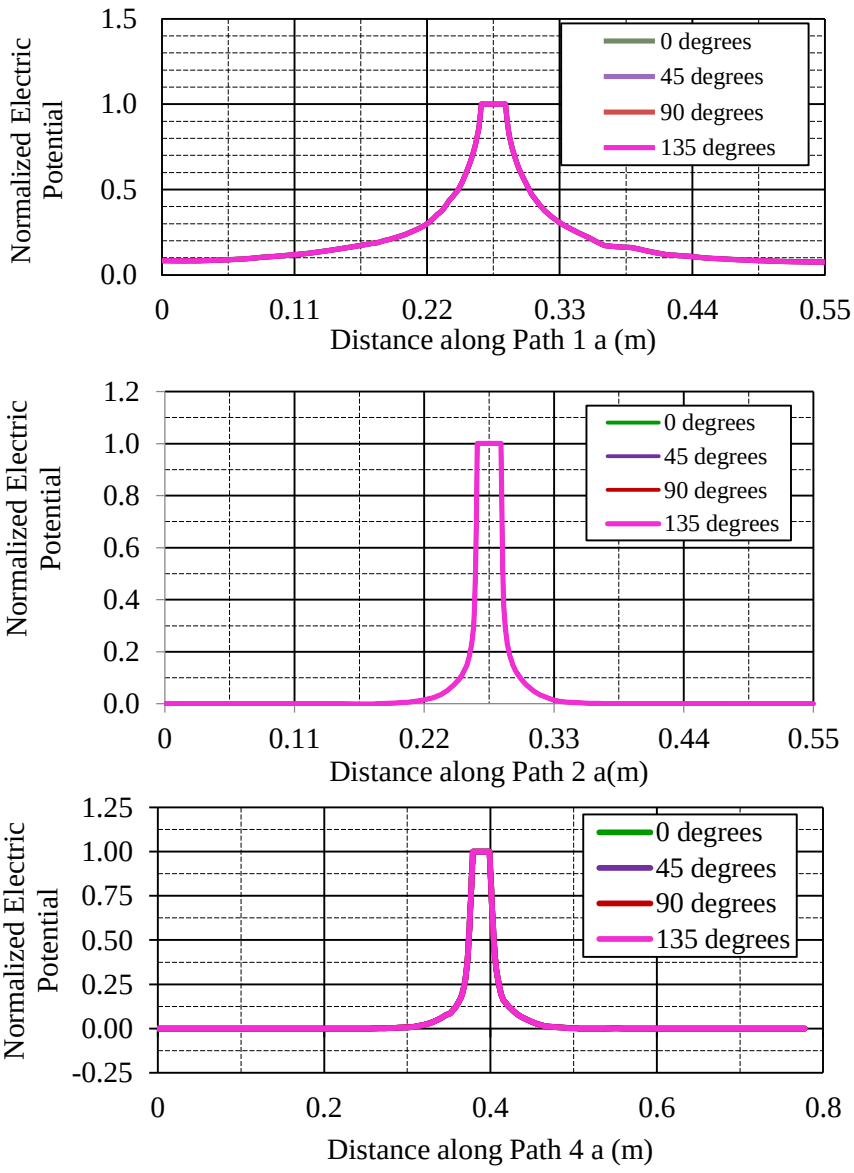

Fig. 3-13. Normalised potential profiles along horizontal and diagonal paths (1a, 2a, and 4a, see Fig. 3-13) for a two-layered carbon-reinforced plastic panel with variable orientation of the second ply.

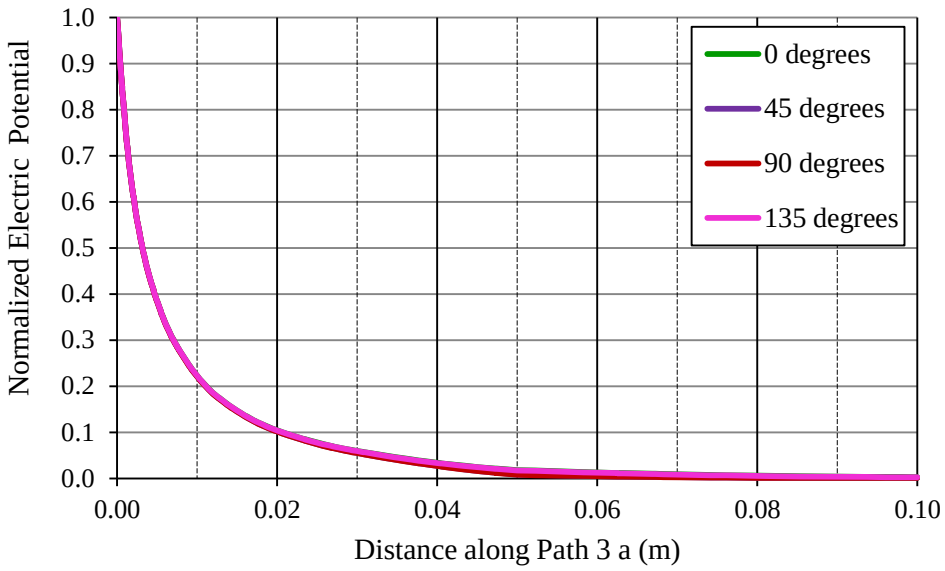

Fig. 3-14. Normalised potential profiles along the vertical path (3a, see Fig. 3–13) for a two-layered carbon-reinforced plastic panel with variable orientation of the second ply.

An important feature of the voltage profile along path 1a is that the potential does not begin at zero or decrease to zero. This is because path 1a follows the fibre direction of the uppermost layer (oriented at 0°), for which the potential is non-zero at the edges. These correspond to the shared equi-potentials described above for the simulations. This result was verified with an infrared camera (Fig. 3–15) for a particular case in which the second ply is oriented perpendicularly to the first one, that is, in a [0°, 90°] arrangement. Fig. 3–16 shows the COMSOL simulation that was performed to further interpret this finding. The IR image in Fig. 3–15 indicates temperature governed by current paths and closely matches the current profiles visible in Fig. 3–16.

3.10 Current and Potential Distribution in Two Layered Panels

The temperature profiles obtained using infrared experiments reveal current paths on the surface of the samples. At this stage, the temperature profile was not recorded for these experiments. Fig. 3-16 shows current distribution across a [0°,90°] sample. The equipotentials in the lower layer are distributed perpendicularly to those in the top layer,

reflecting the [0°,90°] arrangement of the two. Similarly, for [0°,45°], [0°,60°], and [0°,135°] samples, the equipotentials on the lower layer will be oriented respectively at 45°, 60°, and −45°, with respect to those on the upper layer. These results show that the distribution of equipotentials inside the CFRP panel arising from direct current injection is ply-dependent.

These results are highly relevant to the development of real aircraft parts. The panels for modern aircraft are most commonly fabricated using quasi-isotropic and cross-ply composites than with two-layered CRFPs. Thinner panels (~2 mm thick) are typically used for the wings than for the main body of the aircraft. (Note that the distribution of equipotentials in thicker samples was not part of this research progam and has not been investigated in this PhD thesis.)

Since the edges of the plane are grounded (zero voltage), when lightning strikes, damage will primarily occur on the upper side—the one exposed to lightning. In practice, the exposed panels are covered with a 20-μm thick lightning protection layer. The simulations performed here in this arrangement with a peak current of 1 kA show that the equipotentials are concentrated on the surface of the sample and that the current does not penetrate into the composite. However, these results are intensity-dependent with shared equipotentials being observed for higher current intensities.

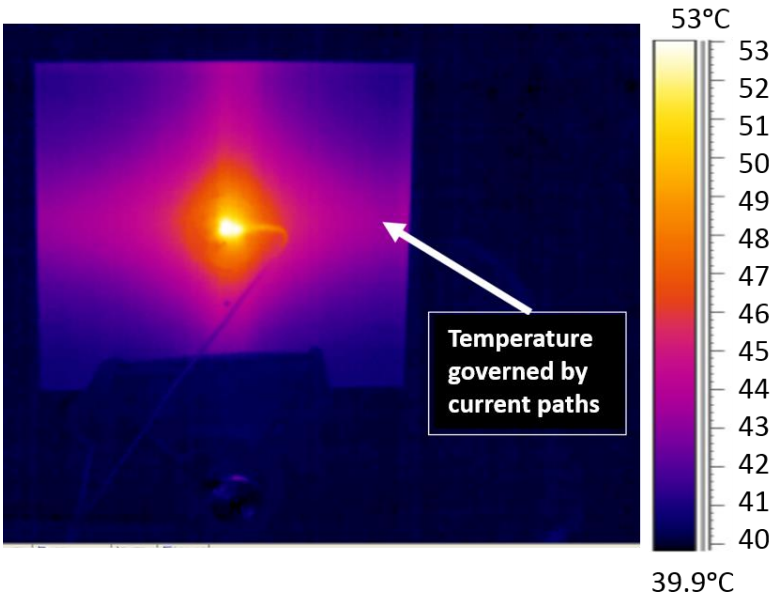

Fig. 3-15. Infrared thermograph of the surface of a [0°, 90°] M21/T800s two-layered panel submitted to a direct current.

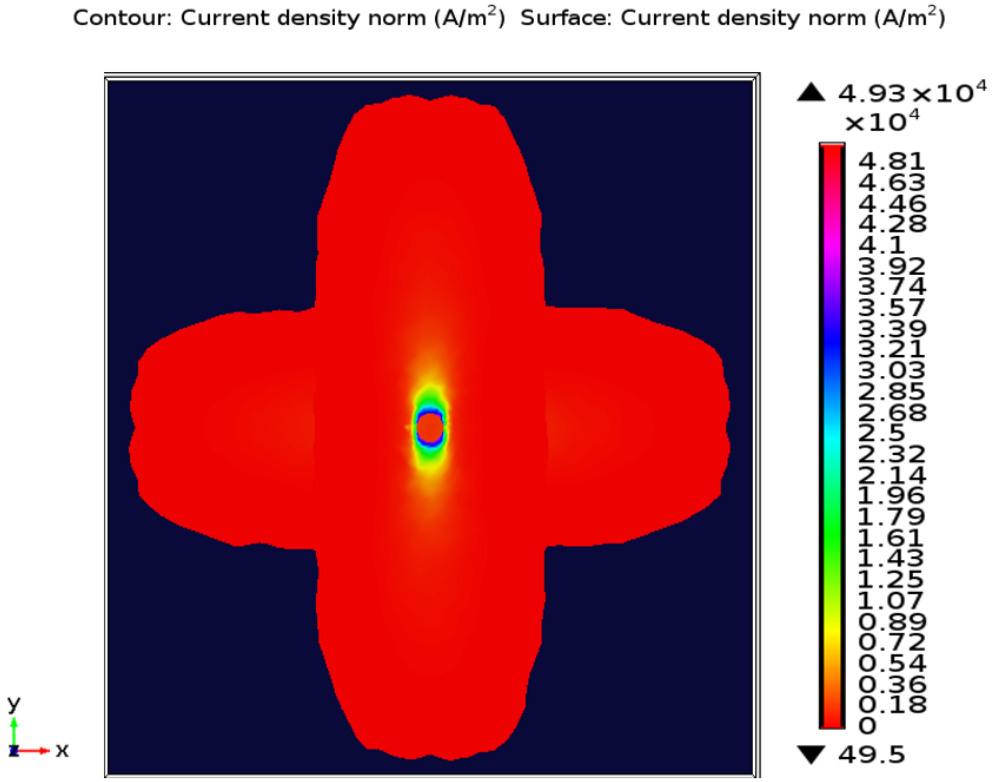

Figure 3-16. Simulated current distribution maps in a [0°, 90°] M21/T800s-type two-layered panel.

Hot spots occur on the surface the panel during DC injection as shown in Fig. 3–15 where the point of current injection reaches 53°C. This is a sign of Joule heating, with the material heating up as current is passed through the panel. The amount of heating that results from current flow depends on the thermal conductivity and thermal coefficient of the sample. According to industry, the thermal conductivity of carbon fibre composites is generally [300, 250, 50] (W/(m. K)). Thermal and electrical conductivity measurements are performed with different setups and a coupled thermal-electrical model for carbon fibre composite is yet to be developed.

Although current and voltage distributions are readily obtained, the actual damage imparted by lightning strikes to CFRPs is difficult to determine using COMSOL simulations. In this study, an estimate is made from simulations performed at intensities ranging from 1 kA to 200 kA at 10 kA intervals. A density of 1.58 kg/m^3 was used with a heat capacity of 1000 J/K—values obtained directly from an industrial partner; the sample was kept at 22°C and recurrent effects were not included in the model.

These electrothermal simulations were used to produce temperature versus lightning current intensity graphs. The temperature output from the simulation is useful in practice to predict the temperature rise in a CFRP for a given lightning current level. These results, therefore, set the foundations for future investigations in this field. Furthermore, the temperature of the sample is clearly crucial in understanding temperature-induced damage in aircraft panels during a lightning strike. However, the experimental setup at the MBLL did not allow experimental verification of the numerical relationships.

Using the above-mentioned parameters, equi-potential surfaces were obtained for a lightning impulse in a two layered sample using COMSOL. For a [0°,45°] sample. Fig. 3–17 shows the potential distribution in the sample after the peak current has been reached. Twisting is

observed in the lower layer (oriented at 45°). The equipotentials move upwards such that the equipotentials shared between the two layers become distorted in the middle of the panel. The equipotentials concentrate in two corners of the panel. The movement of the equipotentials from the upper layer to the lower layer and back reflects the increase in electrical current up to the peak level and its subsequent decrease back to its initial state. The black arrows in Fig. 3–17 show the direction of aggregation and distortion of the equipotentials.

The potential distribution shown in Fig. 3–17 varies as a function of time, with equipotentials changing in potential due to current flow towards the edges of the sample and becoming distorted in the bottom layer. Furthermore, the equipotentials are each more contracted close to the peak time. Note finally that although the thickness of the panel is clearly a critical parameter, at this stage, the effects of thickness on the potential distribution remain to be investigated.

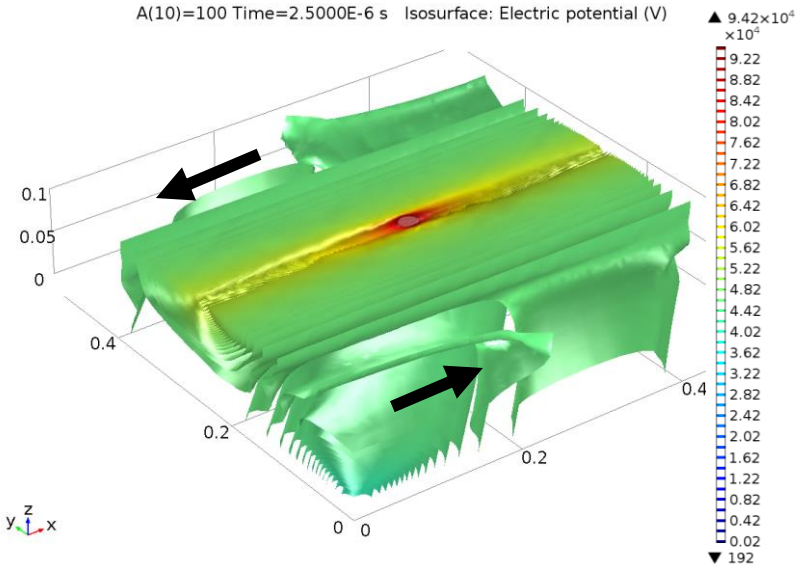

Fig. 3-17. Simulated isopotential surfaces on a full [0°,45°] composite panel after the peak voltage time with arrows highlighting the aggregation and distortion of equipotentials on the edge and bottom layer of the sample, respectively.

3.11 Potential profiles

Additional information can be extracted by plotting voltage profiles along the edges of the sample. Fig. 3–18 shows the resulting voltage profiles and the corresponding numbering scheme used for the edges of the 55 x 55 cm panel (Fig. 3–18 inset). The profiles along edges 1 and 3 are identical except in the [0°,45°] and [0°,135°] two-layered panels, for which the profiles for the two edges are switched; that is, the profile along edge 1 for the [0°,45°] matches that along edge 3 for the [0°,135°] sample and vice versa. The results are similar along edges 2 and 4, which have identical profiles for all two-layered ply lay-ups other than the [0°,45°] and [0°,135°] arrangements, in which the profile along edge 2 is the mirror image of the one along edge 4. For edges 2 and 4, the unidirectional panel (i.e. with both layers oriented at 0°) is the one in which the mid-edge potential maximum is the highest.

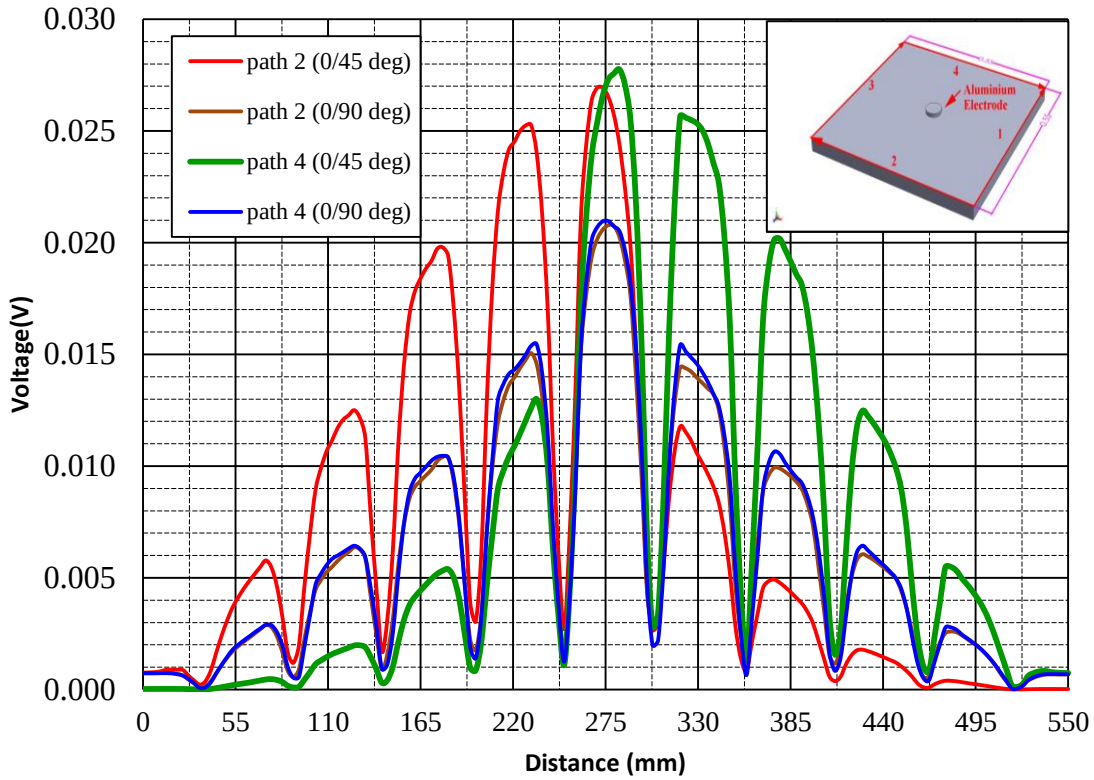

Fig. 3-18. Voltage profiles simulated along horizontal surface edges of half-meter panels with different ply orientations. The geometry of the panel and the numbering scheme used for the edges are shown in the inset.

3.12 Through-thickness potential profiles

Louis et al. [52] have investigated experimentally the through-thickness resistivity and the external factors that govern it in CFRPs. However, only few studies of the through-thickness resistivity have been performed using a guard electrode. A guard electrode test is typically conducted by maintaining a gap between the two electrodes (see Fig. 3–19) placed on the top surface of the sample; the lower electrode (i.e. the third one, the current return electrode) covers the entire surface of the sample. This arrangement avoids fringing effects in the electrical field. The gap ‘g’ is twice the thickness of the sample. This setup was used to measure the current and voltage profiles for samples with four ply lay-ups.

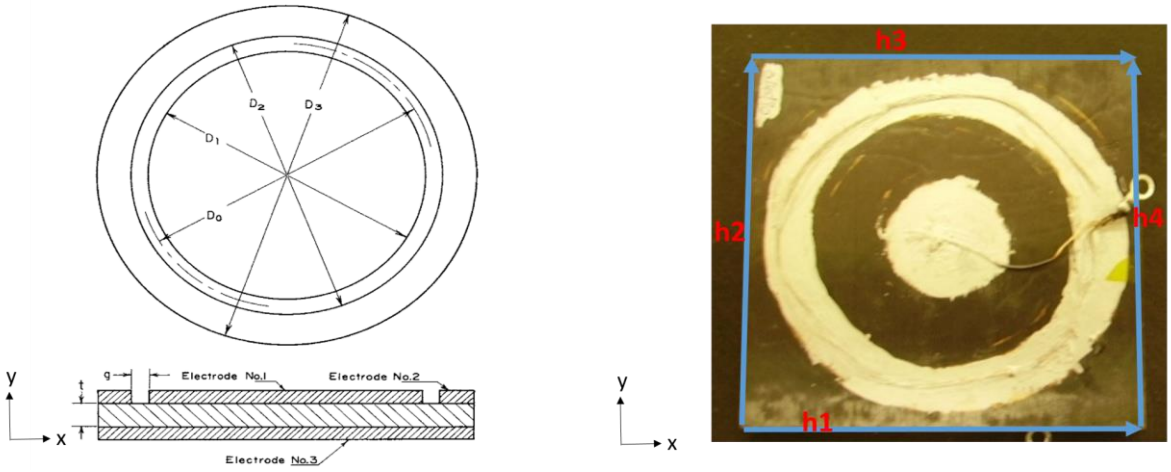

Fig. 3-19. Schematic of the setup used for guard electrode tests according to the ASTM D257 standard (left) and a sample prepared for experiment (right)

For all the samples, electrode No. 1 was 80-mm long and g was 10-mm wide (see Fig. 3–20). Electrode No. 3 covered the entire surface of the sample. Finite element simulations were performed using COMSOL with the resulting current density patterns on the surface of the samples shown in Fig. 3–20. The current densities obtained for the [0°,45°] and [0°,45°,90°]

ply lay-ups are identical. Fig. 3–20 shows that fringing, which would occur if the electrodes were placed directly on the surface of the samples, does not occur with this setup.

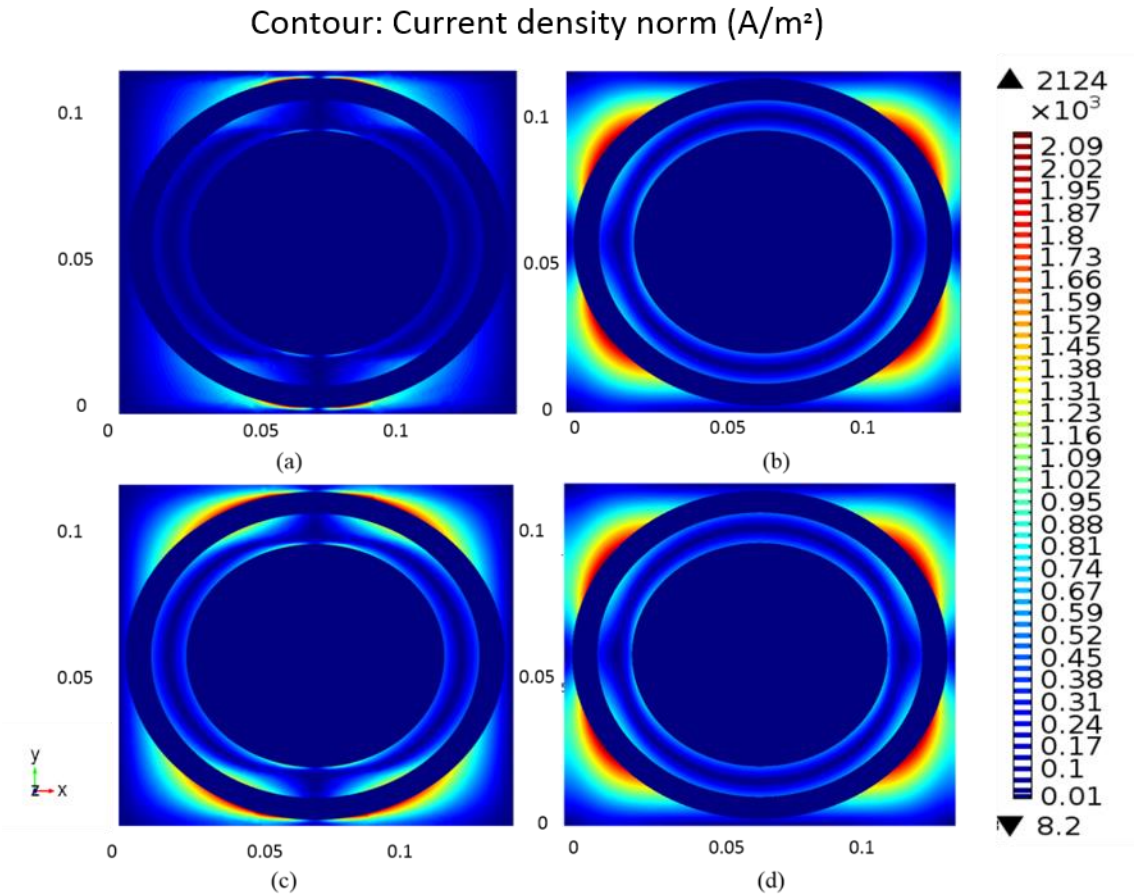

Fig. 3-20. Simulated current density plots on the surface of composite samples (a) 0°, (b) 0°,45°, (c) 0°,90° and (d) 0°,45°,90° lay-ups, with guard electrodes arranged according to the ASTM D257 standard.

As can be seen in Fig. 3–21, along the four edges of the sample (numbered as shown in Fig. 3–19), the electric potential along horizontal edge h4 for the unidirectional sample increases sharply from 0.19 V at its extremities to 0.22, forming a plateau in the middle at a level similar to that recorded across edge h2. For the [0°,90°] sample, the potential varies little along the edges of the sample. Along edge h4 for the [0°,45°] sample, the central plateau is at 0.18 V (similar to the potential measured along edge h2) and the voltage decreases to 0.15 V on both sides. Along edge h1 of the same sample, the electric potential increases from 0.21 V

in the corners to 0.22 V in the middle of the edge, a similar value as recorded for edge h4 of the unidirectional sample.

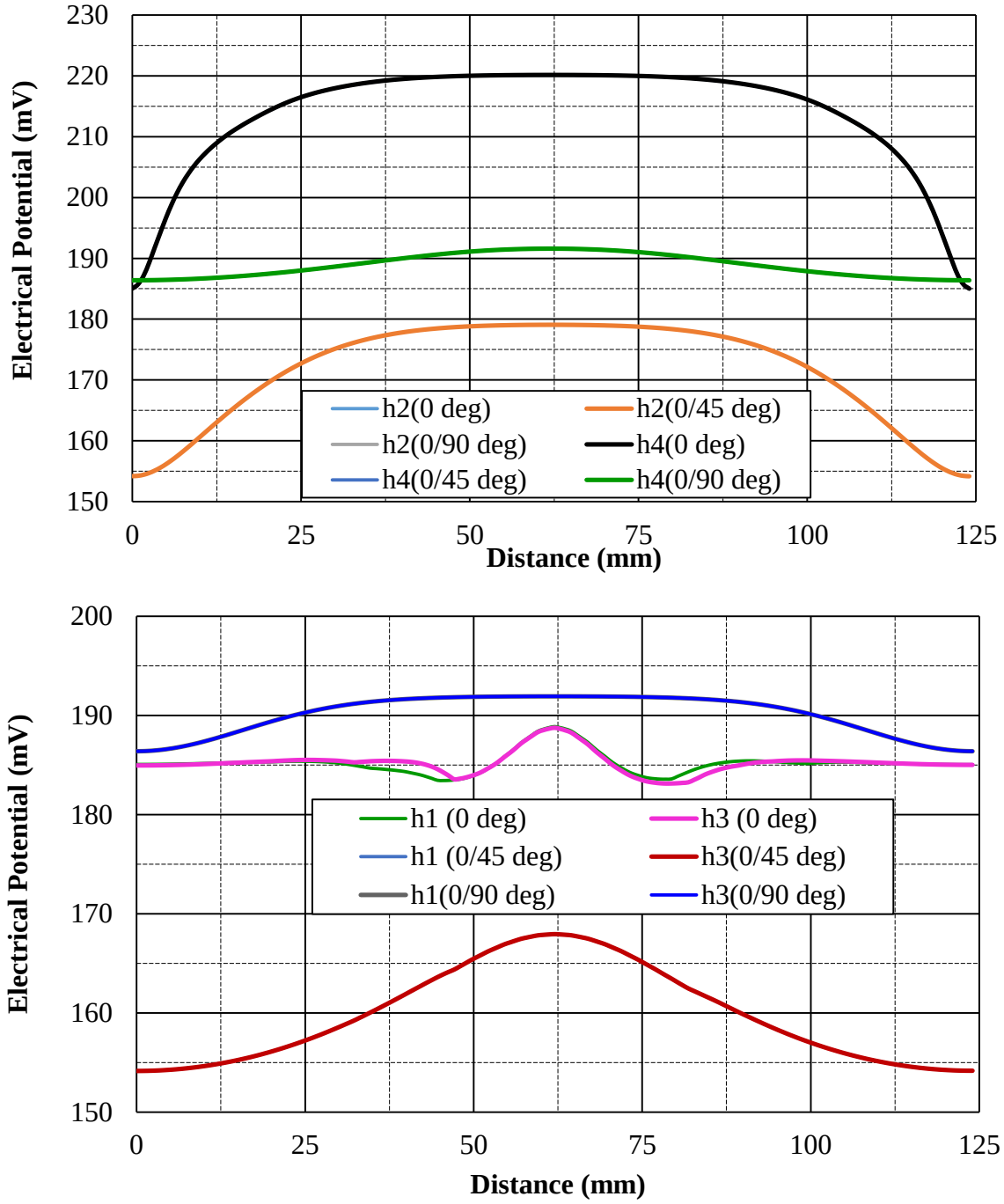

Fig. 3-21. Voltage profiles simulated along the four horizontal edges of composite samples with [0°,0°], [0°,45°], and [0°,90°] lay-ups, with guard electrodes arranged according to the ASTM D257 standard. The numbering of the edges corresponds to the one shown in Fig. 3–19.

The rise in voltage is minimal such that a plateau is not formed. Along edge h3 for the [0°,45°] sample, the electric potential is ~0.15 V in the corners and increases gradually to ~0.17 V in the middle of the edge. For the [0°,45°] sample. Therefore, the horizontal profiles along the four edges differ significantly, whereas with a [0°,90°] lay-up, they are essentially identical.

As simulated in the guard electrode configuration with a current of 200 mA flowing, the vertical profiles at the edges of the samples with each ply lay-up are shown in Fig. 3–22. For the unidirectional, [0°,90°], [0°,45°], and [0°, 45°, 90°] samples, the electric potential in the corners is 0.19 V, 0.21 V, 0.15 V, and 0.32 V, respectively. For each ply lay-up, in contrast with what is observed for the horizontal edges (see Fig. 3–22), the electric potential profiles along the four vertical edges are identical.

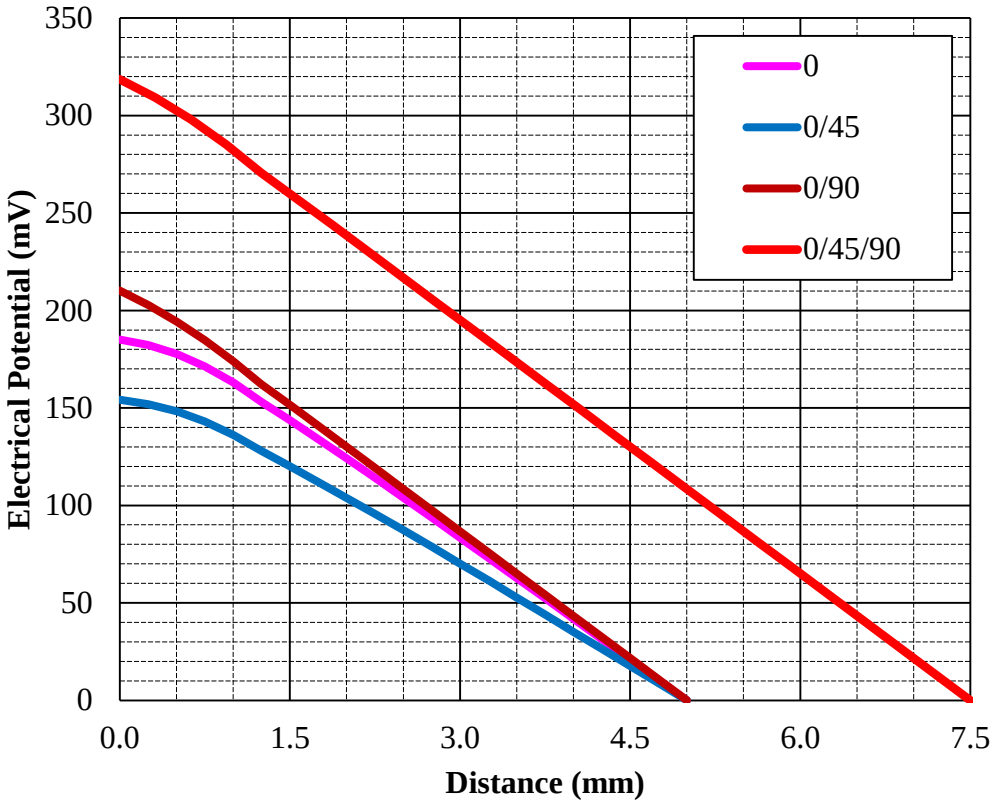

Fig. 3-22. Voltage profiles simulated along the four vertical edges of composite samples with [0°,0°], [0°,45°], and [0°,90°], and [0°,45°,90°] lay-ups, with guard electrodes arranged according to the ASTM D257 standard. The numbering of the edges corresponds the one shown in the inset.

3.13 Embedded electrode design simulation

Simulations were then performed for samples whose specifications matched those obtained directly from the manufacturer. As illustrated in Fig. 3–23, a model was constructed in COMSOL with an embedded electrode, a central fastener, and 8 rivets placed at a radius of 67.5 mm from the centre at angular intervals of 22.5°. The samples were tested under high current intensities. However, the current and potential distributions in the material prior to imposing the high current are also of interest. In these simulations, therefore, the middle fastener and outer metal ring were respectively used as a current injection point and as a current return electrode.

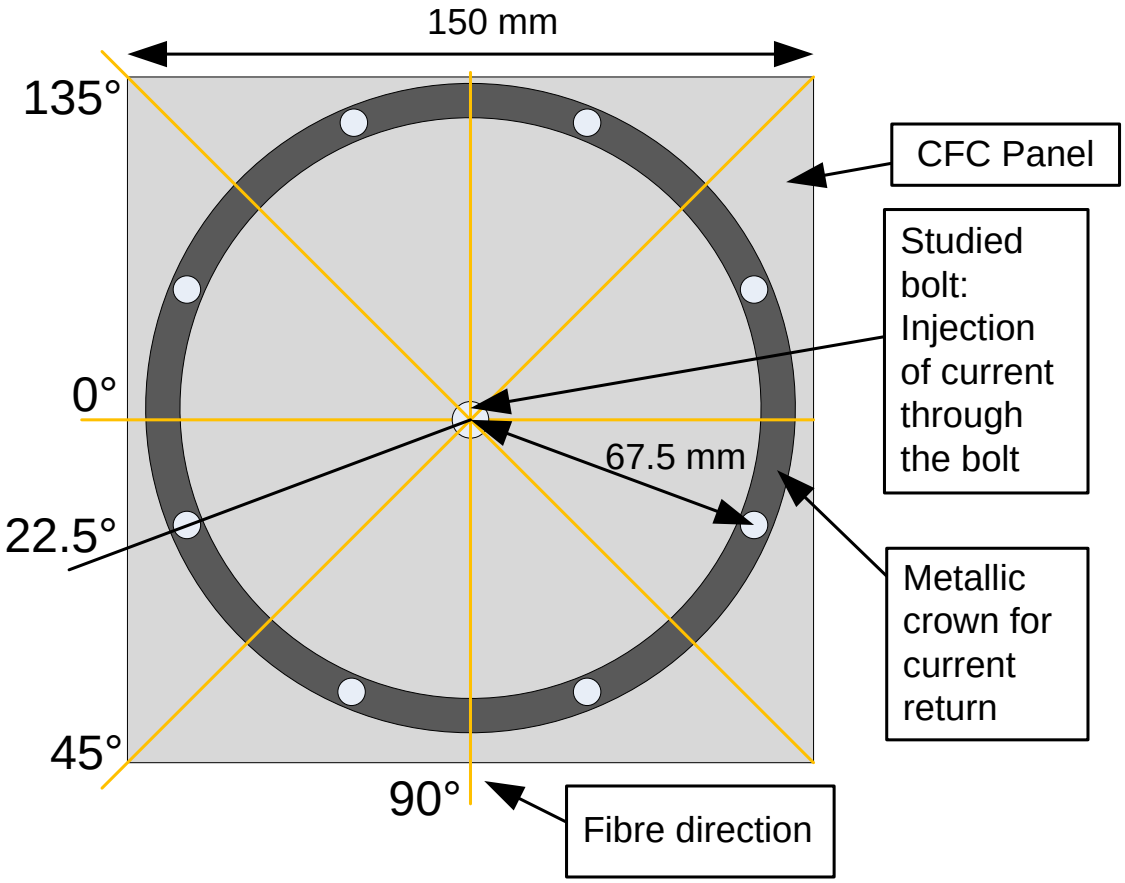

Fig. 3-23. Schematic of the embedded electrode setup with a metal ring used in this study to measure potential and current distribution in carbon-reinforced plastic composites.

Fig. 3–24 shows the simulated current density distributions for quasi-isotropic and cross-ply samples. The surface distribution shows the current spreading in the lower diagonal layer for the quasi-isotropic sample and in the perpendicular layer for the cross-ply sample.

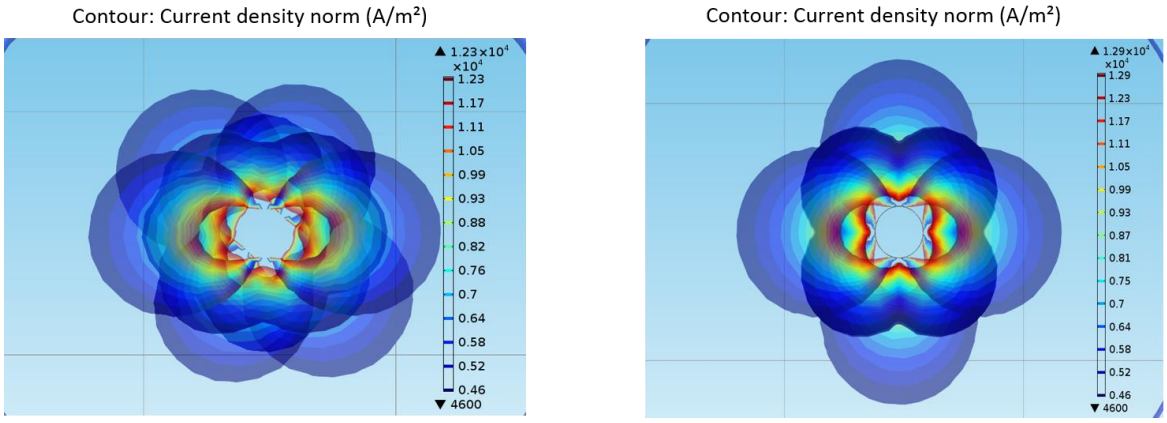

(a) (b)

Fig. 3-24. Current density contour maps (A/m^2) for composite samples with (a) quasi-isotropic and (b) cross-ply lay-ups as simulated under a direct current of 1 A with the embedded electrode setup shown in Fig. 3–23.

Fig. 3–25 shows the horizontal potential profiles along the *x* and *y* directions for CFRP samples with unidirectional, [0°,90°], [0°,45°], and quasi-isotropic lay-ups. As measured on the surface of the sample (z = 2 mm), the potential for the unidirectional panel is zero along *x*. For the same edge, local maxima are observed at 0.08 m and 0.12 m for the [0°,45°] sample, which are attributed to the presence of diagonal layers whose resistivity is high near the panel edges. For the [0°,90°] panel, the voltage maximum is much greater than for the unidirectional panel but the voltage profile is symmetric. The profile for the quasi-isotropic lay-up is also symmetric but the peak voltage is less than 0.005 V. Along the *y* edge, the symmetrical profile for the unidirectional lay-up peaks at ~0.08 m, near the metal ring.

Fig. 3–26 shows the voltage profiles along diagonal paths for various ply lay-ups. For all the samples, the potential profile is symmetric about the location of the fastener, where the voltage is maximal. However, the peak voltages differ amongst the samples, with ~0.31 V,

~0.15 V, ~0.12 V, and ~0.1 V recorded for the unidirectional, [0°,45°], [0°,90°], and quasi-isotropic samples, respectively.

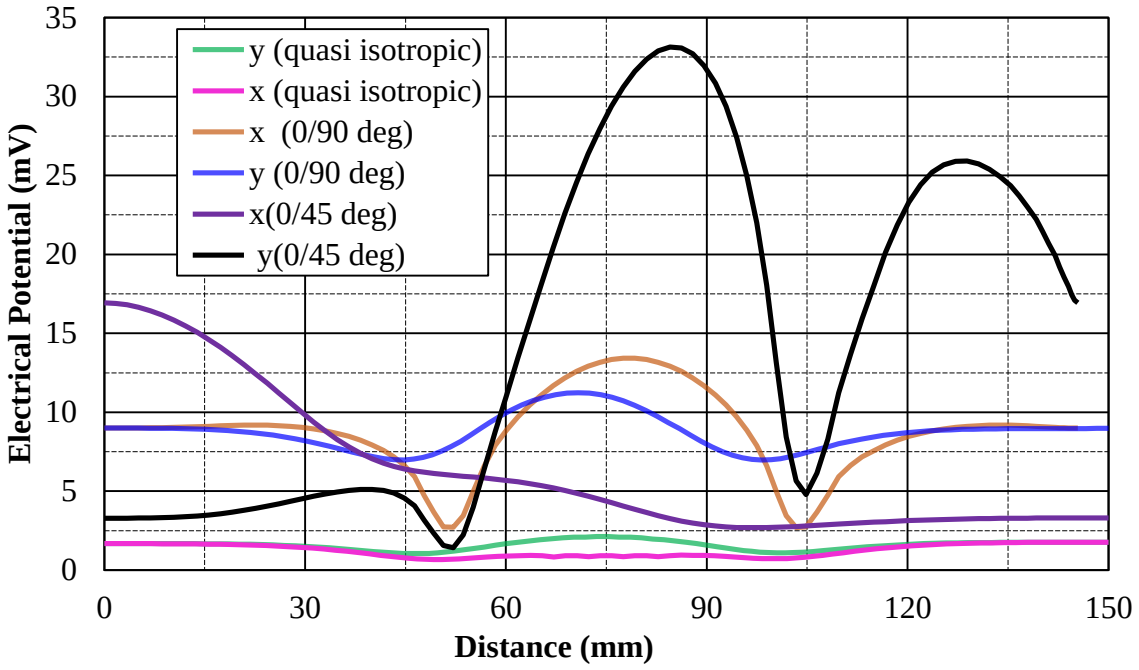

Fig. 3-25. Horizontal surface potential profiles along *x* and *y* for composite samples with unidirectional, [0°,90°], [0°,45°], and quasi-isotropic lay-ups as simulated under a direct current of 1 A with the embedded electrode setup shown in Fig. 3–24.

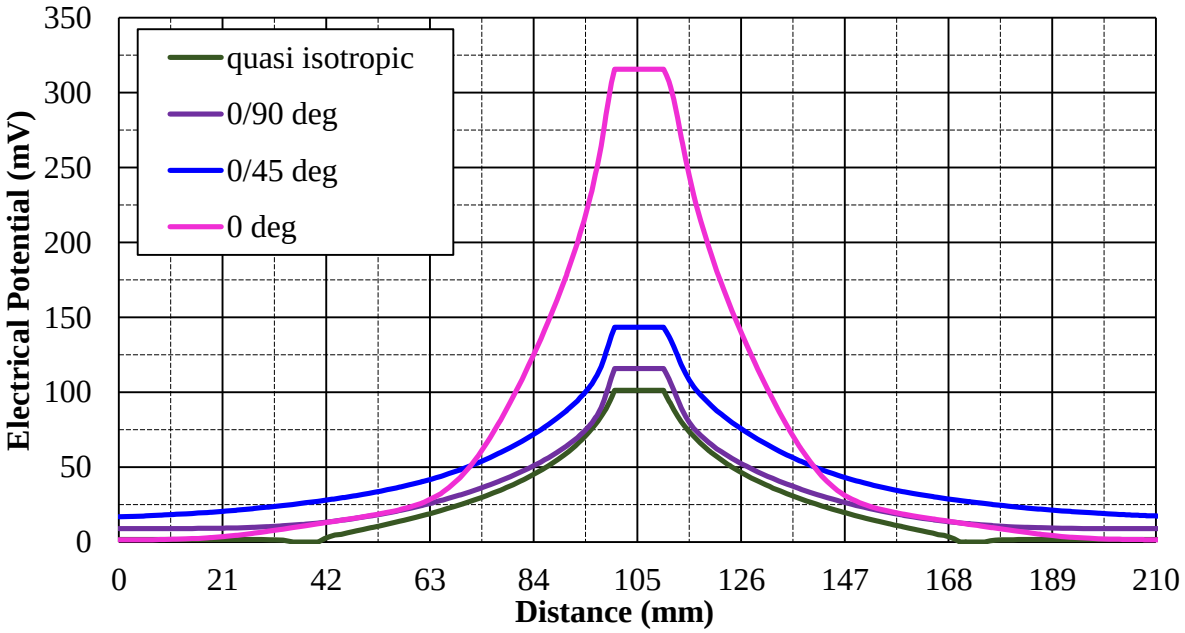

Fig. 3-26. Diagonal surface potential profiles composite samples with unidirectional, [0°,90°], [0°,45°], and quasi-isotropic lay-ups as simulated under a direct current of 1 A with the embedded electrode setup shown in Fig. 3–24.

3.14 Conclusions

This chapter reported simulations—performed for the first time—of CFRP panels under realistic conditions. In particular, the current density profiles in the through-thickness direction were obtained for different ply lay-ups. The published literature on experimental through-thickness studies may be extensive; however, computational models allow current paths to be extracted more readily for such a configuration.

Moreover, a metal ring electrode configuration was also studied at high current intensities for various ply lay-ups, including quasi-isotropic and cross-ply samples. The simulations showed that the voltage profiles differed among the different horizontal and diagonal paths through and along the edge of the samples. Simulations were also performed to obtain these profiles under lightning strike conditions.

Another important finding, discussed in this chapter, was the existence of shared equipotentials in carbon composites in two layer panels, which are shown here to be the result of their resistive behaviour rather than due to unexplained ‘twisting’ of the potentials as has been reported elsewhere. These results were verified and could indeed be compared with those in the literature on the basis of which the ‘twisting’ interpretation was derived. The simulation results obtained in this work show clearly that the material (multi-layered CFRP) behave in a resistive manner.

Chapter 4

ELECTRICAL CHARACTERISATION: SURFACE AND VOLUME RESISTANCE STUDY

4.1 Introduction: two- and four-probe methods

As described in more detail in Chapter 2, the basic difference between two- and four-probe measurements of volume resistance is that the four-probe method minimizes possible inaccuracies arising from contact resistance [53]. Indeed, with a two-electrode setup in which one is used for current injection and the other for voltage measurements, the contact resistance is included in the readings, making them less accurate. In the four-probe method, the voltage is measured at different points relative to the current injection point, eliminating the contact resistance from the results. If, as is the case here, a surface-based electrode configuration is used with the four-probe method, the parasitic resistance recorded will include both the electrode/surface contact resistance and the distortion resistance arising from current spread. This latter contribution depends on how the current is injected—parallel or perpendicular to the top fibre layer—and is, therefore, indicative of the fibre orientation. An important part of this investigation, therefore, concerns measuring the parasitic resistance, Re, defined as the sum of the contact, Rc, and distortion, Rd, resistances. The resistance of each electrode is calculated using potential values obtained from a set of measurement arrays. The contact resistance may not be accurate because the injected current does not flow in totality through the injection path. Instead, and as described by Chung [54], the current is

distributed according to the orientation of the top fibre layer. As a result, with this configuration, the current penetrates non-uniformly into the sample and the current distribution therein is also non-uniform. The potentials measured in the sample are, therefore, not simple functions of the injected current. However, if these values can be related to the current, a set of indicative, apparent resistances can be obtained. Two-electrode measurements of the volume resistance necessarily include the contact resistance of the electrodes such that this component cannot be measured explicitly or calculated. This chapter focuses on different approaches for measuring volume and surface resistances along different directions in various CFRP panels. First, a number of electrode attachment techniques were developed and investigated to explore the most suitable technique for the experimental characterization of the CFRP test samples. To the authors knowledge some of these are new to CFRP testing.

4.2 Abrasion techniques

The top layers of the carbon composites include a resin-rich layer, which needs to be abraded to ensure a good electrical connection to the conductive carbon fibres. This was achieved here initially by hand polishing and then using dry shot blasting and a Vapormatt wet blaster, respectively. Hand polishing was found to be more damaging for the sample surface than the blasting techniques. Wet blasting was chosen among the latter two as it provided optimal resin abrasion.

4.3 Electrode formation techniques `

Two new techniques were employed to form electrodes on the sample surfaces, namely silk screening using conductive silver paint, and photo-etching, as used to prepare printed circuit boards. Photo-etching proved unsuccessful for thicker samples and, since this technique

involves chemical etching and electroplating, whose effects on the microstructure of composite materials are unknown, this approach was only used for one sample. The electrodes on remaining samples were prepared by silk screening.

4.3.1 Silk screening using conductive silver paint

Silk screening involves embossing a pattern/print on a substrate with ink. The substrate is typically a cloth and the pattern to be embossed or printed is in the form of a plastic sheet. The printing ink is spread over the plastic sheet to flow onto the substrate, which is subsequently allowed to dry. Using the same concept, electrodes were silk screened on carbon composite samples. In this case, the ink is a conductive silver paint with an electrical resistivity of 0.5–1.25 μΩ·m, while the plastic sheet is a vinyl label that is easily removed from the sample surface, leaving no residue behind and avoiding ink spread. The pattern on the vinyl label is a simple series of circles 3 mm in diameter and separated by 20 mm (centre to centre). This pattern was punched manually on the vinyl labels.

4.3.2 Open contacts with a spring-loaded configuration

For the initial tests, four square (10 cm^2) samples of type M21/35%/268/T800s composite were prepared as specified in Table 4–1. Their surfaces were manually abraded using a combination of abrasive papers of different grit sizes, rinsed with ordinary tap water, and cleaned with acetone.

Table 4-1. Ply lay-up and thickness of the M21/35%/268/T800s-type composites used to investigate the effects of silk-screened electrodes.

Ply Lay-Up	**Thickness (m)**
[0°]	0.05
[0°,90°]	0.05
[0°,45°]	0.05
[0°,45°,90°]	0.075

The samples were subsequently left to dry. Thereafter, 10 mm strips of punched vinyl labels were directly pasted onto the areas chosen to deposit the electrodes. A conductive silver paint pen was then used to fill the 3 mm diameter holes before carefully removing the masks. Any breaks or smears were immediately removed before the paint could dry. The samples were allowed to dry in open air over night. A printed circuit board with spring-loaded pins to make contacts with the sample surface electrodes was manufactured and placed on top of the sample. The boards were loaded vertically to ensure that all the pins were in contact with the sample surface. This type of contact led to degradation of the electrodes because the silver paint was exposed to air, causing high variability in the results and unequal pressure on the spring-loaded contacts of the circuit board. As illustrated in Fig. 4–1, the indentation of the silver paint by the spring-loaded contacts leads to variable electrical contacts, which is clearly an undesirable effect of this approach.

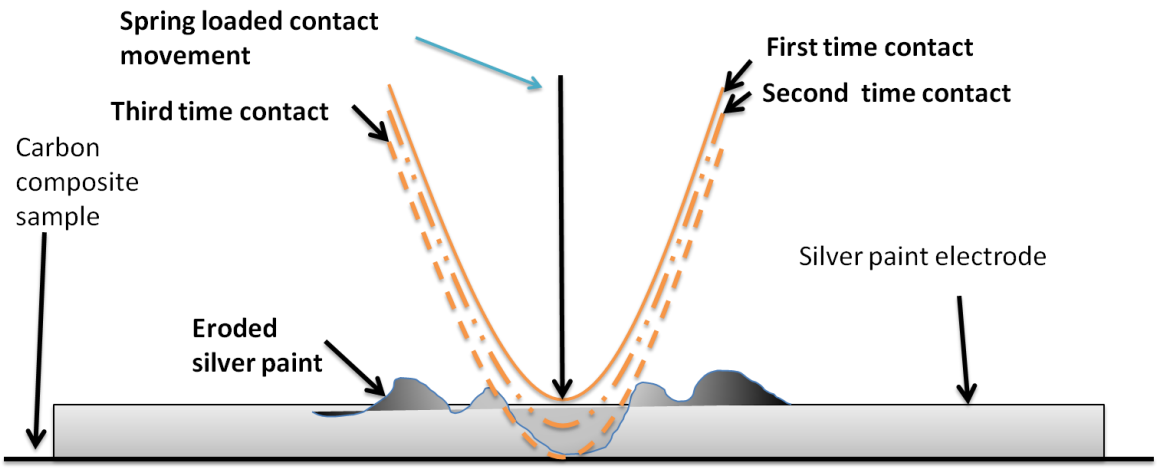

Fig. 4-1. Schematic illustration of the variable electrical contacts due to the indentation of the silver paint electrode caused by the spring-loaded pins from the circuit board used for resistance measurements.

Localised darkening was observed on the contacts. As shown in Fig. 4–2, this degradation resulted in diversion of the current on the sample surface, such that individual measurements were not reproducible. Consequently, the tests on samples in this configuration were interrupted after two measurements.

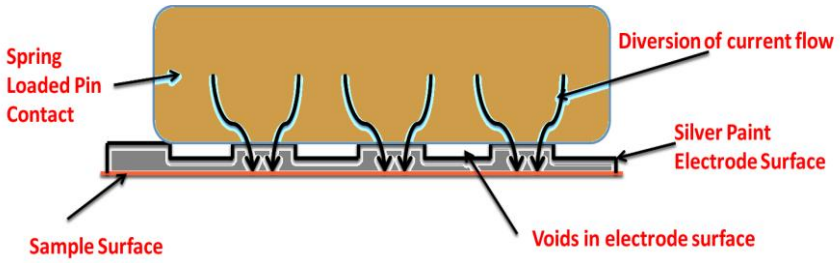

Fig. 4-2. Schematic illustration of the diversion of the current path on the surface of an electrode due to the presence of voids and unequal pin pressure.

4.3.3 Sealed contacts with soldered terminals

Four new samples of the same material were prepared as before in terms of abrasion, cleaning and electrode formation. Thereafter, thin stranded wires were soldered at low-temperature using Lipowitz's alloy to avoid any degradation of the silver paint. (The silver paint used here

can endure temperatures of 177°C for periods of less than five seconds.) Tags were then soldered on the open ends of the wires, and measurements were collected using hooked miniature grabber leads with a maximum current rating of 5 A.

4.3.4 Photo etching

4.3.4.1 Electroplating

Electroplating allows a thin metal layer to be deposited onto a substrate. Todoroki [62] has used this technique to form metal electrodes for the purpose of testing CFRPs. However, the chemical etchant used by this author, persulphuric acid, is highly explosive and its use is prohibited in academic institutions. Todoroki's approach was, therefore, adapted as shown in Fig. 4–3. Electroplating was performed in a copper sulphate bath with copper sulphate crystals at 200 g/l in concentrated sulphuric acid at 30 ml/l to metalize various cross-ply samples. Pure copper electrodes (two anodes and one cathode) were attached to the sample, which was subsequently placed in the electroplating bath.

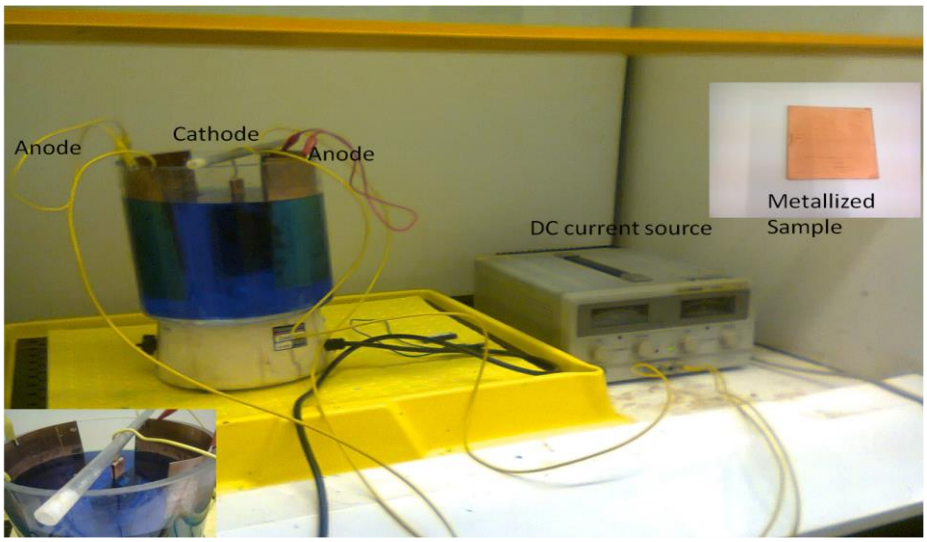

Fig. 4-3. Photograph of the electroplating bath used to prepare photo-etched composite samples.

The electroplated sample, 95 mm × 98 mm × 2 mm in dimensions, was a MTM-28-1-HS-135-35%-RW type composite with a $[(0°, 90°)_4]_s$ cross-ply arrangement. The resin layers on both surfaces of the sample were removed manually using P360-type abrasive paper. The sample was subsequently washed with clear detergent. However, preliminary tests using a variety of techniques (viz. sputtering, soldering, and gluing) demonstrated that good metallic contacts with the sample were seldom achieved.

4.3.4.2 Masking and chemical etching

After metallization, the sample was sprayed with a positive photo-resistive aerosol and placed in an oven at 25°C for at least 12 h. A mask representing a 25-electrode array (each 3 mm wide and 20 mm apart) was printed on acetate. The mask was placed on top of the sample, which was subsequently locked in a UV exposure unit for 4 min for both sides of the sample. The UV light chemically destabilizes the exposed area only and does not pass through the black regions on the mask. Fig. 4–4 shows the resulting sample with the electrodes appearing as green circles.

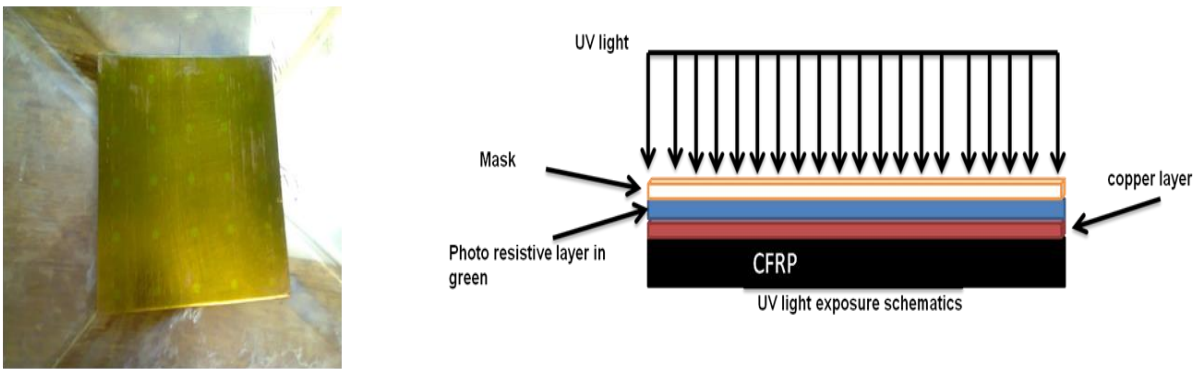

(a) (b)

Fig. 4-4. (a) Photograph of a chemically etched composite sample and (b) schematic of the ultraviolet exposure technique.

The CFRP sample was then placed in a developer solution containing 2% sodium hydroxide. As shown in Fig. 4–5, the areas on the photo-resistive layer previously exposed to UV light reacted with the developer solution and dissolved away, leading to the formation of 25 dots on each side of the sample. The sample was subsequently placed in a solution of ferric chloride ($FeCl_3$) for one hour and periodically shaken to assist the etching process.

(a) (b)

Fig. 4-5. Photographs of (a) a composite sample being dipped in a sodium hydroxide solution, and (b) the sample obtained at the end of the etching process.

Fig. 4–6 shows the texture of the electroplated copper. After removing the copper from the unwanted areas on the sample, acetone was rubbed over the electrode dots to remove the photo-resistive layer and reveal the copper in the dots. To inhibit the oxidation of the copper and to improve subsequent electrical connections, the surface of the sample was dipped in a tin-plating bath for a few seconds.

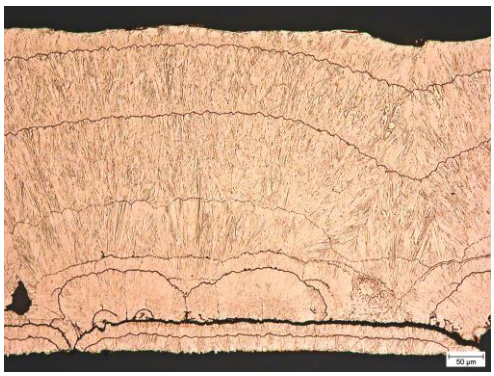

Fig. 4-6. Optical micrograph of the texture of the electroplated copper layer deposited on the surface of a carbon fibre composite.

4.3.4.3 Soldering with Wood's metal—Lipowitz's alloy

Wires were soldered onto the copper-metalized dotted-electrodes using Lipowitz's alloy (otherwise known as Wood's metal). Traditional soldering was not possible because the electroplated electrodes degrade at high temperatures. Lipowitz's alloy has a melting temperature of 70°C and can, therefore, be used for low-temperature soldering. This was conducted with a soldering iron whose temperature was controlled via a variable transformer. The soldering process and an insufficient metal coating caused one electrode to become detached because of poor adhesion between the copper layer and the carbon fibre surface. Tests were performed using the remaining 24 electrodes.

4.3.5 Wire/braid setting with paint

Carbon fibre composite samples for volume conductivity measurements were first prepared by soldering electrodes using Lipowitz's alloy. In comparison, in the conventional technique used by many researchers, the wire is simply placed on the sample and set using silver paint. The wire was, therefore, set with paint along the entire length of the electrode (see Fig. 4–7) instead of being soldered at a single point. When comparing the samples prepared using the two techniques, the samples with thin and flexible electrodes attached had much lower resistances than those soldered in a single point. Samples were also prepared using a thicker, less flexible wire 0.10 mm in diameter (see Fig. 4–8), composed of 64 braided copper strands. A microstructural analysis was then performed to view each connection type.

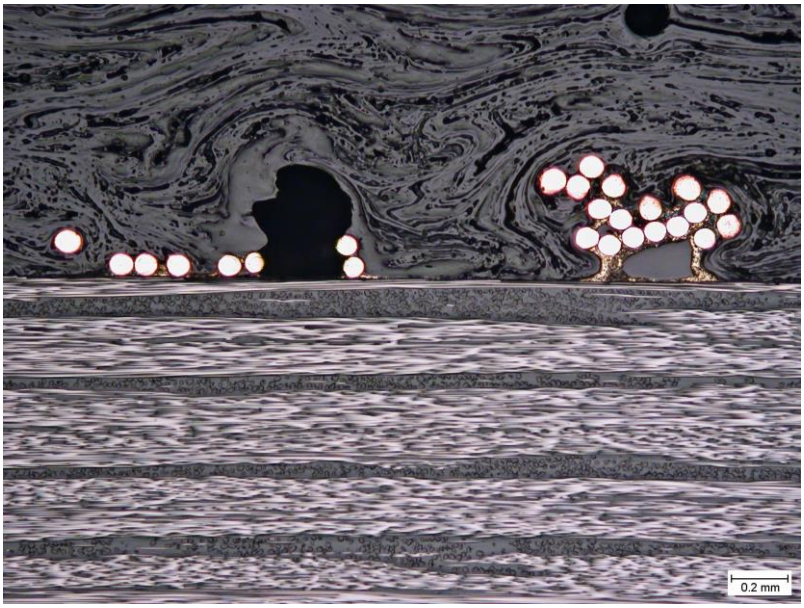

Fig. 4-7. Optical micrograph of copper wires set with conductive silver paint on the surface of a carbon fibre composite.

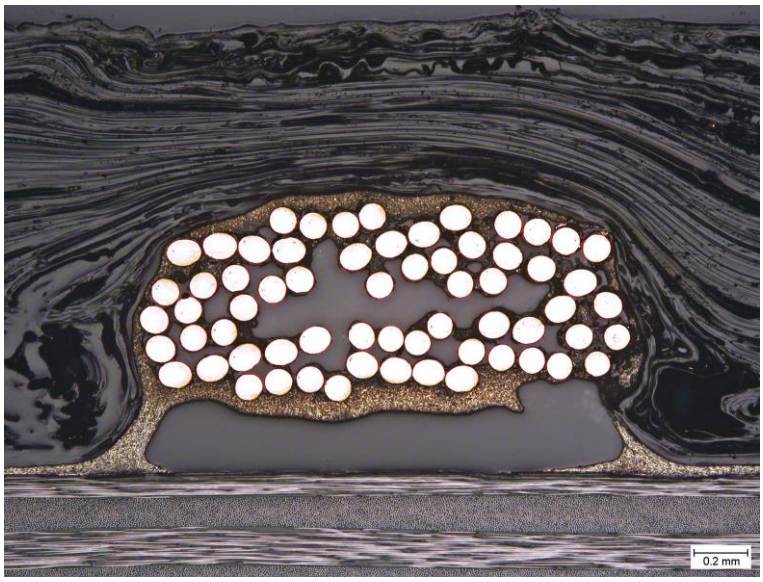

Fig. 4-8. Optical micrograph of a braided copper wire set with conductive silver paint on the surface of a carbon fibre composite.

4.3.6 Thermal vacuum evaporation

Thermal vacuum evaporation is a technique used to deposit ultrathin metal layers on a substrate. The evaporation process is conducted under high vacuum to ensure the clean

deposition of metal particles on the substrate. A thermal vacuum evaporation system consists mainly of a vacuum pump and an energy source. Metal, typically in the form of a wire, is fed into the evaporator and deposited onto the substrate, which is then heated using an electric filament.

In this study, metal layers were deposited by thermal vacuum evaporation onto carbon fibre composites (by Mr. Chris Dunscombe at the School of Physics and Astronomy in a clean room). Layers of copper and silver up to 240 nm thick were deposited on the CRFP samples. Fig. 4–9 shows the texture of one of these copper layers. A tape test was conducted to evaluate the adhesion to the underlying substrate of the copper and silver layers, the latter proving more strongly attached. The copper layers were, therefore, removed by immersing the evaporated samples in acetone. As shown in Figs. 4–10 and 4–11 respectively for the copper and silver layers, these are too thin for the intended application. This technique was, therefore, not used to form resistance-sensing electrodes.

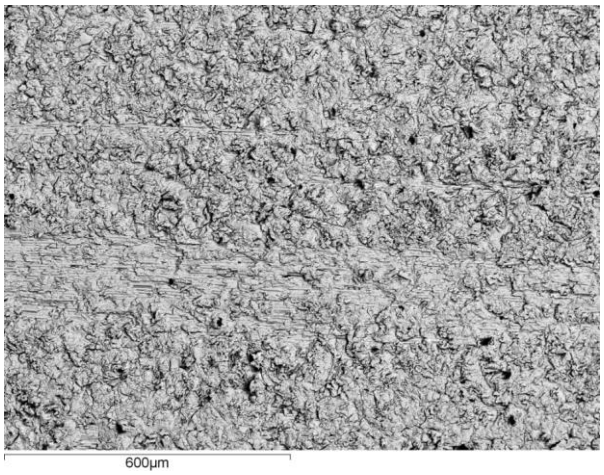

Fig. 4-9. Optical micrograph of a copper layer deposited by thermal vacuum evaporation on the surface of a carbon fibre composite.

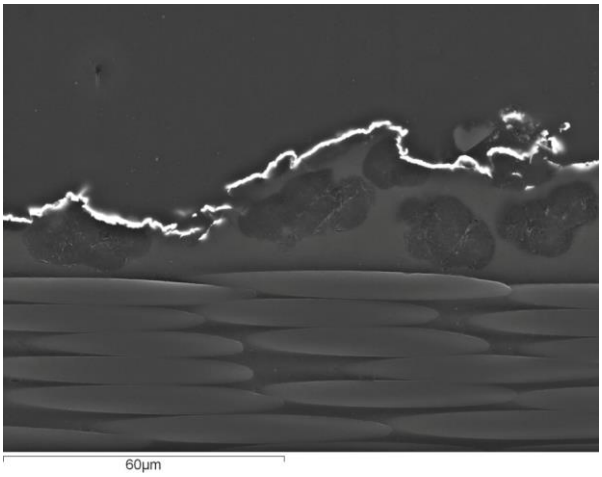

Fig. 4-10. Cross-sectional optical micrograph of a copper layer deposited by thermal vacuum evaporation on the surface of a carbon fibre composite.

Fig. 4-11. Cross-sectional optical micrograph of a silver layer deposited by thermal vacuum evaporation on the surface of a carbon fibre composite.

4.4 CFRP Resistance measurement techniques and results

4.4.1 Proposed measurement approach for carbon fibre samples

In this study, several existing methods were adapted to prepare electrode arrays arranged as shown in Fig. 4–12. These arrays were then placed on the surface of CRFP samples to measure the apparent or terminal parasitic resistance at each node of the array using silver paint and highly thin flexible wire. For terminal measurements of voltage and current, the total apparent resistance measured, R_a, is the sum of the parasitic resistance, R_e, and the material resistance, R_m:

$$R_a = R_e + R_m \quad (4\text{-}1)$$

The parasitic resistance, R_e, is assumed to be composed of a contact resistance, R_c, and a current dispersion resistance, R_d, which accounts for current flowing away from the current injection electrodes to reach a uniform distribution in the material:

$$R_e = R_c + R_d \quad (4\text{-}2)$$

The material resistance, R_m, reports on the portion of the sample in which the current is uniformly distributed over the large surface area between the voltage electrodes.

With this particular conduction mechanism, the resistance components can be distinguished by performing several tests along a line of electrodes (e.g., 1 to 5 in Fig. 4–12) with a variety of current injection points and voltage measurements on the inner electrodes, as illustrated in Fig. 4–13. By combining the results of these different tests judiciously, the parasitic resistance, R_e, can be separated from the material resistance, R_m. This is procedure explained in details in the following sections.

4.4.2 Test configurations and procedure for surface characterisation

To verify that the electrical parameters of carbon composite panels are uniform, resistance measurements must be performed across the entire surface of the samples. Two tests configurations were used in these tests. Configuration 1: Longitudinal (along the fibres) and Configuration 2: Transverse (Perpendicular to the fibres). The electrodes attached to the surface of the sample were numbered in sequence from 1 to 25 (as shown in Fig. 4–12), and measurements were performed in two configurations to visualise the surface potential distribution and calculate the apparent resistance of the composites. In configuration 1, the current is injected across the fibres in the surface layer. The current must cross the high

resistivity resin matrix and, therefore, spreads over a wide area. In the adopted configuration 2, the current is injected along the fibres in the surface layer. The current flows readily along the fibres, which have a lower resistivity than the resin, leading to reduced current spread.

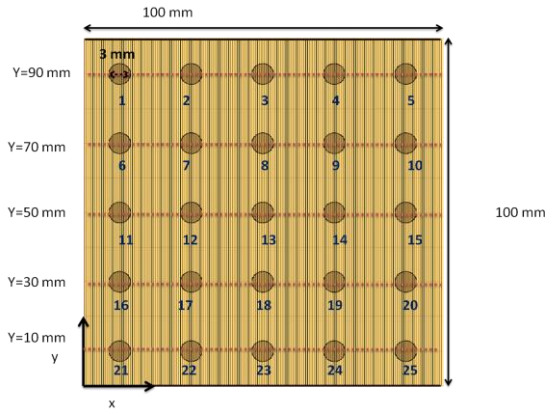

Fig. 4-12. Array of surface electrodes proposed here for resistance mapping in carbon fibre composites.

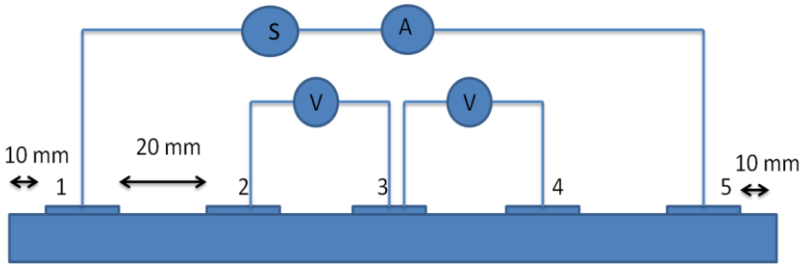

Fig. 4-13. Schematic of the arrangement of the lines of electrodes (1–5) used to map the resistance of carbon fibre composites by four-probe sensing.

Under both configurations 1 and 2 as explained earlier, four datasets were obtained for each line from y = 10 mm to y = 90 mm and from x =10 mm to x = 90 mm (see Fig. 4–12), and eight readings were taken for each line. The measurements taken at y = 90 mm are summarised in Table 4–2 and can be described as follows (Figs. 4–12 and 4–13 show the location of the different electrodes mentioned):

(i) For dataset 1, the current was injected between electrodes 1 and 5, and the differential voltage was measured between electrodes 2 and 3 and between electrodes 3 and 4.

(ii) For dataset 2, the current was injected between electrodes 1 and 3, and the voltage was measured between electrodes 1 and 2 and between electrodes 2 and 3.

(iii) For dataset 3, the current was injected between electrodes 3 and 5, and the voltage was measured between electrodes 3 and 4 and between electrodes 4 and 5.

(iv) For dataset 4, Current was injected between electrodes 2 and 4, and the voltage was measured between electrodes 2 and 3 and between electrodes 3 and 4.

Table 4-2. The electrodes involved in the measurement of four datasets at y = 90 mm using the electrode system shown in Figs. 4–12 and 4–13.

Dataset	Current Injection Electrodes	Voltage Electrodes	Voltage Notation*
1	1,5	2,3	V_{23}^{15}
		3,4	V_{34}^{15}
2	1,3	1,2	V_{12}^{13}
		2,3	V_{23}^{13}
3	3,5	3,4	V_{34}^{35}
		4,5	V_{45}^{35}
4	2,4	2,3	V_{23}^{24}
		3,4	V_{34}^{24}

*In this notation, the current injection electrodes are listed in the superscript and the voltage measurement electrodes in the subscript.

4.4.3 Resistance Calculation Procedure

For the DC tests, a constant current of 200 mA was injected using a GW INSTEK PSM 6003 programmable DC source with a precision resistor connected to a computerised data acquisition system.

4.4.3.1 Calculation of surface resistances

The measurements are based on the assumption that when either of the current injection electrodes coincides with the voltage electrodes, the measured resistance includes that of the electrode. Similarly, it is assumed that when the injection electrodes do not coincide with the voltage electrodes, the parasitic resistance, Re, is not included in the measurement. Furthermore, given that the electrodes are uniformly distributed over the surface of the sample, it is assumed that the material resistance, R_m, between two adjacent electrodes in a line (along x or y) is constant across the sample.

As an example of calculation, the measured potential values from datasets 1 and 2 provide the parasitic resistance, R_e, for electrode 3 (given that $R_{e2} = R_{e3} = 0$ for V_{23}^{15}) through the following equation:

$$R_{e3(1)} = \frac{V_{23}^{13} - V_{23}^{15}}{I_{\text{circuit}}} \tag{4-3}$$

The resistance for the same electrode can also be obtained again using the potential values from datasets 1 and 3:

$$R_{e3(2)} = \frac{V_{34}^{35} - V_{34}^{15}}{I_{\text{circuit}}} \tag{4-4}$$

The values obtained for $\mathbf{R_{e3(1)}}$ and $\mathbf{R_{e3(2)}}$ are very close for all electrodes, *n*, across the sample.

For electrodes 2 and 4, datasets 1 and 4 are used:

$$R_{e2} = \frac{V_{23}^{24} - V_{23}^{15}}{I_{\text{circuit}}} \tag{4-5}$$

Using the above calculation method and repeating the test for all the electrode lines, a map of resistances was obtained for the entire sample. Table 4–3 and Fig. 4–14 show the resistances calculated in this way for electrodes 1–5 along the line corresponding to *y* = 90 mm in Fig. 4–12.

Table 4-3. DC resistance of the electrode, R_e, and material, R_m, measured for a test sample with a [0°,0°] ply lay-up for electrodes 1–5 along *y* = 90 mm using the electrode system shown in Figs. 4–12 and 4–13.

Electrode	*1*	*2*	*3*	*4*	*5*
R_e (Ω)	8.7	6.9	6.5	5.1	7.9
R_m (Ω)	5.8	5.8	5.4	5.4	

4.4.3.2 Unidirectional sample

All 20 plies in this sample were orientated in the 0° direction. Table 4–4 lists the full set of DC resistances for all electrodes calculated in the x and y directions using the procedure described in the previous section.

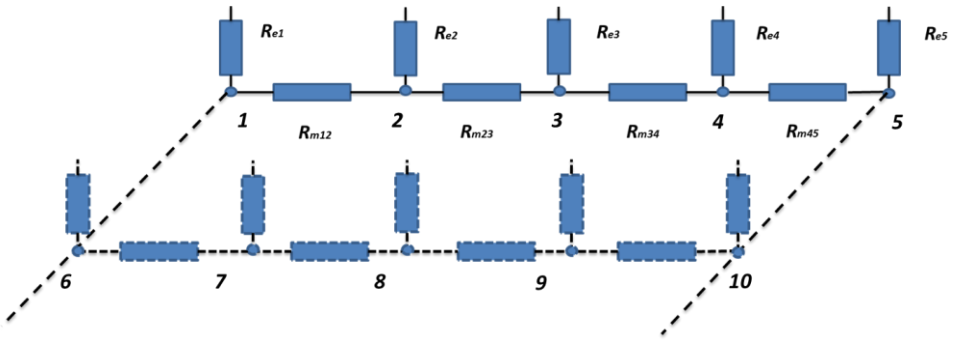

Fig. 4-14. Circuit representation of the tested sample.

Table 4-4. DC resistances of the electrode, R_e, and material, R_m, measured for a [0°,0°] ply lay-up sample for all the electrodes in the system shown in Figs. 4–12 and 4–13.

Config. 2 *x* (mm)	**Electrode pairs R_m(Ω)**		**Electro de No.**	**R_e (Ω)**
			1	1.28
	1,6	0.45	6	1.00
10	6,11	0.45	11	0.89
	11,16	0.60	16	1.09
	16,21	0.60	21	1.24
			2	0.89
	2,7	0.67	7	0.66
30	7,12	0.67	12	0.69
	12,17	0.68	17	0.66
	17,22	0.68	22	0.73
			3	1.51
	3,8	1.20	8	0.92
50	8,13	1.20	13	0.83
	13,18	0.39	18	0.98
	18,23	0.39	23	0.97
			4	0.86
	4,9	0.46	9	0.75
70	9-,4	0.46	14	0.65
	14,19	0.54	19	0.76
	19,24	0.54	24	0.79
			5	1.12
	5,10	0.47	10	0.77
90	10,15	0.47	15	0.81
	15,20	0.72	20	0.74
	20,25	0.72	25	0.83

Config. 1 *y* (mm)	**Electrode pairs R_m(Ω)**		**Electro de No.**	**R_e (Ω)**
			1	6.81
	1,2	5.83	2	3.96
90	2,3	5.83	3	6.20
	3,4	5.39	4	4.53
	4,5	5.40	5	5.83
			6	6.14
	6,7	6.03	7	3.58
70	7,8	6.03	8	5.46
	8,9	5.64	9	4.18
	9,10	5.65	10	5.48
			11	5.91
	11,12	6.40	12	3.50
50	12,13	6.40	13	5.25
	13,14	5.42	14	3.97
	14,15	5.42	15	5.52
			16	6.23
	16,17	5.71	17	3.55
30	17,18	5.67	18	6.42
	18,19	5.45	19	4.25
	19,20	5.41	20	5.61
			21	6.77
	21,22	5.94	22	3.92
10	22,23	5.94	23	5.76
	23,24	5.33	24	4.46
	24,25	5.33	25	6.01

For configuration 1 (transverse), the current path crosses the resin gaps between the fibres, which explains the relatively high values obtained for R_m (5.4–6.4 Ω) and R_e (3.5–7 Ω). For configuration 2 (longitudinal), in contrast, the resistances R_m and R_e range from 0.4 Ω to 1.2 Ω and from 0.65 Ω to 1.5 Ω, respectively. The resistance is indeed expected to be lower in the longitudinal direction as the current flows readily along the carbon fibres. This effect is also verified by IR thermography (Fig. 4–15). For configuration 2, the hot spots along the current injection path are indicative of current confinement, while for configuration 1 the current spread is more pronounced.

These experiments were repeated under impulse energisation, with similar results obtained (Fig. 4–15). This verifies that the electrical network inside a carbon composite is indeed primarily composed of electrically conductive carbon fibres. Assuming that the fibres are perfect conductors, the distortion resistance can be assumed to be zero for current flow along the fibres. Therefore, for a unidirectional panel with no distortion resistance, Eq. (4-5) becomes Re = Rc. For multi-layered carbon fibre composites or for samples with different ply orientations, separating the contributions from the distortion and contact resistances is less straightforward.

The results obtained with the current injected in the transverse direction reveal widespread current flow. This indicates that the distortion resistance is relatively high and that the carbon fibres can be modelled as perfect insulators in the transverse direction.

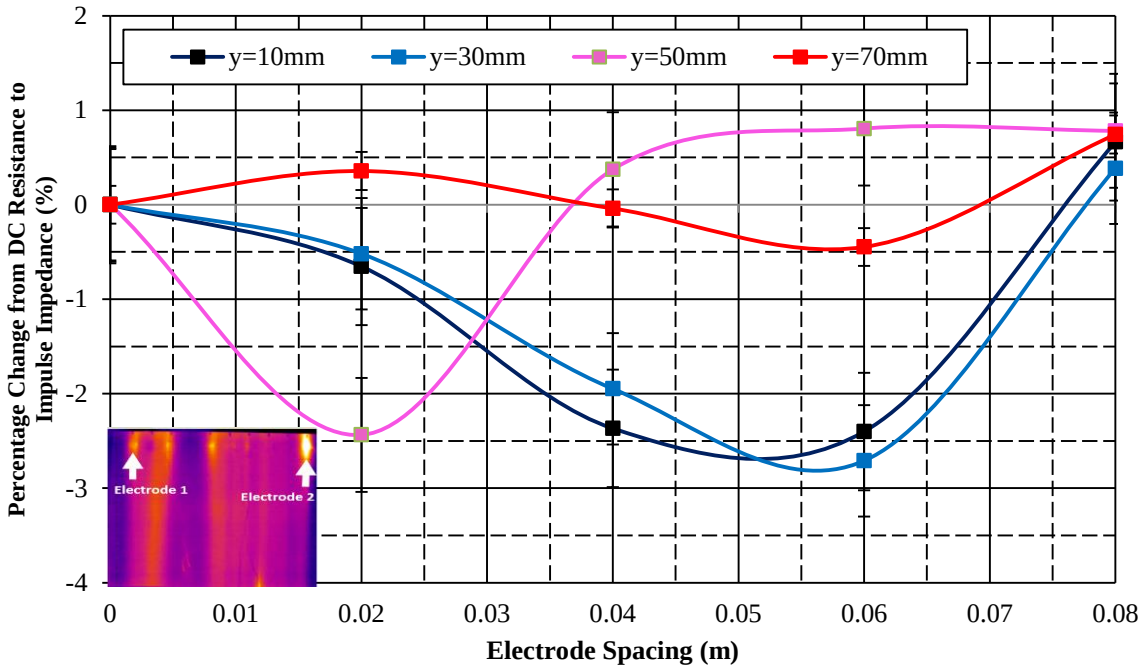

(a) Configuration 1

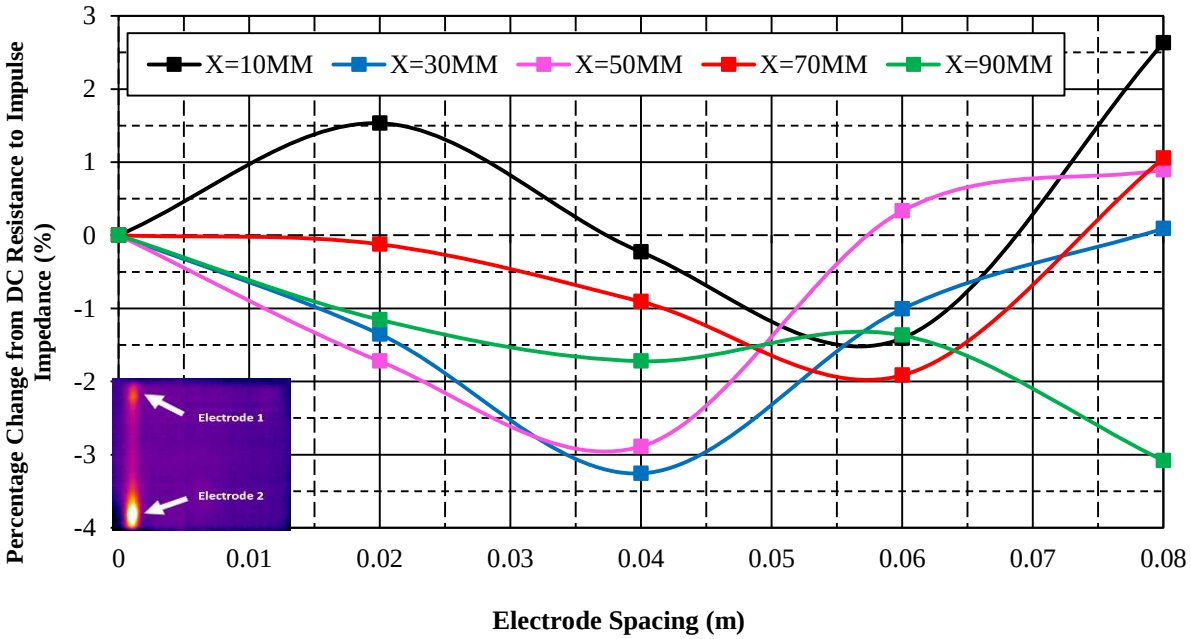

(b) Configuration 2

Fig. 4-15. Percentage difference between the DC and impulse resistances measured at different positions along (a) *x* and (b) *y* for a unidirectional sample, using the system shown in Figs. 4–12 and 4–13.

4.4.4 Cross-ply sample

Similar measurements were performed on a 2 mm thick cross-ply sample composed of 16 plies. The electrode array for this sample was prepared by photo-etching. Because of the symmetrical ply lay-up, the resistance for this sample is expected to be the same in both directions. As a result, the current distribution should also be the same along the *x* and *y* axes. Interestingly, however, the results in Table 4–5 show that despite the symmetrical ply lay-up, the resistances of the material as measured, here, for transverse and longitudinal current injections, are different, with values of ~30 mΩ and ~0.3 mΩ, respectively. It is thought that this results from the current penetrating or not into the sample. Indeed, while current injected along the fibres penetrates into the panel, current injected across the fibres does not, such that configuration 2 will always yield lower resistances than configuration 1.

The thickness of the panel is also important in this context. The unidirectional and cross-ply samples simulated here are respectively 5 mm and 2 mm thick. The penetration depth of the current into the sample is readily obtained computationally but was not verified experimentally in this work. The simulated current paths obtained for transient currents show that the current spreads over most of the surface. However, there is no current flow inside the sample between the current electrodes, showing that transverse currents do not penetrate into the composite.

4.4.5 Resistance profiles on composite surfaces

In addition to bulk resistance measurements, the apparent surface resistance profiles along the *x* and *y* paths were measured with current injected at the end electrodes of each line. A profile typical of the ones obtained is shown in Fig. 4–16 along with a diagram of the experimental setup. The resistance profiles along the *y* and *x* axes measured under DC energisation for a

unidirectional panel are shown in Figs. 4–17 and 4–18, respectively. The resistance profiles along the *x* axis (current flow perpendicular to the fibre direction) are similar, which is due to the high resistance along these paths across the insulation layers. There is some variability between the profiles along the *y* axis (along the fibre direction), which may be due to random contact between the fibres along certain paths, causing small changes in the resistance and deviations in the corresponding distributions.

Table 4-5. DC resistances of the electrode, R_e, and material, R_m, measured for a cross-ply sample for all the electrodes in the system shown in Figs. 4–12 and 4–13.

Config. 1 *y* (mm)	**Electrode Pairs**	**R_m (mΩ)**	**Electrode Number**	**R_e (Ω)**
			6	1.67
	6,7	30	7	1.99
70	7,8	30	8	1.26
	8,9	32	9	7.20
	9,10	32	10	1.59
			11	1.35
	11,12	26	12	1.68
50	12,13	26	13	1.03
	13,14	30	14	2.13
	14,15	30	15	1.21
			16	1.61
	16,17	28	17	1.68
30	17,18	28	18	1.09
	18,19	32	19	1.30
	19,20	32	20	1.49
			21	1.79
	21,22	36	22	2.34
10	22,23	36	23	1.57
	23,24	40	24	1.43
	24,25	40	25	2.46
Config. 2 x (mm)	**Electrode Pairs**	**Rm (Ω)**	**Electrode Number**	**Re (Ω)**
			2	1.44
	2,7	0.30	7	1.63
30	7,12	0.30	12	1.36
	12,17	0.34	17	1.31
	17,22	0.34	22	1.80
			3	1.41
	3,8	0.18	8	1.01
50	8,13	0.18	13	0.89
	13,18	0.18	18	0.98
	18,23	0.18	23	1.92
			4	1.46
	4,9	0.26	9	6.25
70	9,14	0.26	14	2.00
	14,19	0.20	19	1.09
	19,24	0.20	24	1.15
			5	1.33
	5,10	0.24	10	1.32
90	10,15	0.24	15	0.99
	15,20	0.32	20	1.16
	20,25	0.32	25	1.94

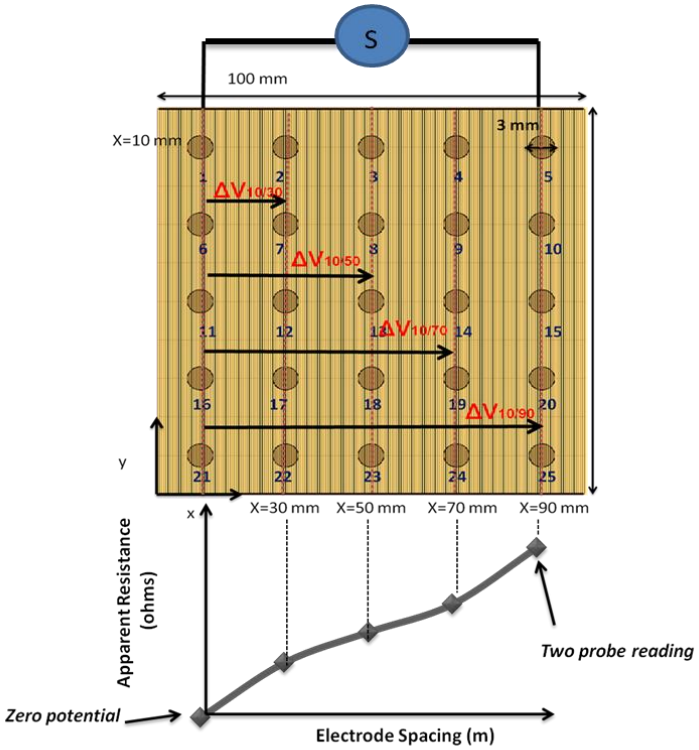

Fig. 4-16. Electrode array placed on the surface of composite samples for three-probe resistance measurements and an example of the apparent resistance profiles obtained.

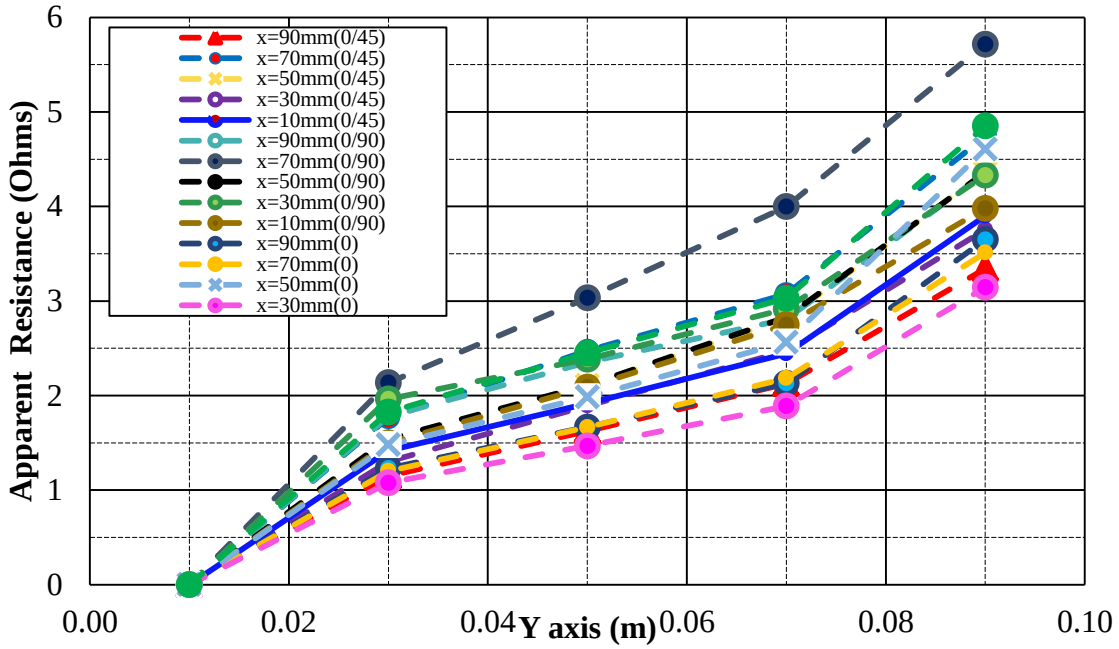

Fig. 4-17. Apparent resistance profiles measured along the *y*-axis at different values of *x* on the surface of carbon fiber composite samples with different lay-ups using the experimental setup shown in Fig. 4–16

Figs. 4–17 and 4–18 also show the resistance profiles obtained in a similar manner for [0°,90°], and [0°,45°] samples. The values obtained for the different paths along *y* (at different values of *x*) are somewhat scattered (Fig. 4–17), whereas the profiles along *x* (at different values of *y*) are concentrated together with little variability between those obtained for different paths (Fig. 4–18). (Note that the scattering along *y* is even greater for the [0°,45°] sample.)

The same apparent resistances are measured along x = 10 mm and x = 30 mm, and the resistance is higher along the path at x = 70 mm. This is because of a restrained edge effect at x = 70 mm, which—in contrast with the situation at x = 10 and x = 30—prevents the current traveling back and forth between layers.

For the [0°,45°] sample, there is some variability among the resistance profiles measured along the y-axis but not for those measured along the *x*-axis. This shows that the distortion resistance for current flow in line with the fibres is negligible and that the main contribution to the parasitic resistance is the contact resistance.

The apparent resistance is the largest for the unidirectional sample at x = 90 mm. Current injected along the *y* axis is in line with the fibre direction. This ensures that the distortion resistance is minimised and that the material resistance, therefore, accounts for a larger proportion of the total resistance. The exact proportion is unknown, however, because the contact resistance contribution cannot be determined. Along the *x*-axis, substantial current distortion means that similar resistance profiles are obtained at all y values.

Current injected in the transverse direction tends to spread across the surface of the panel such that similar apparent resistances are measured for all the paths across the surface. The current follows the path of least resistance, and this depends on the ply orientation of the

sample.

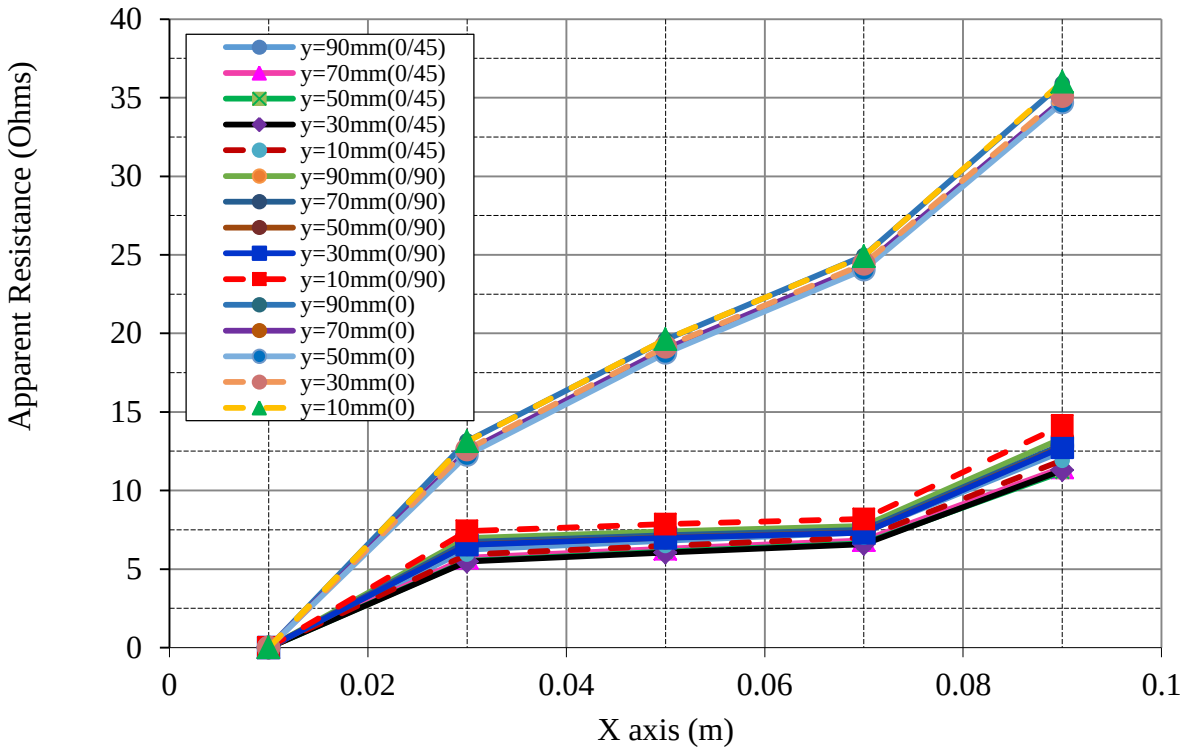

Fig. 4-18. Apparent resistance profiles measured along the *x*-axis at different values of *y* on the surface of carbon fibre composite samples with different lay-ups using the experimental setup shown in Fig. 4–16.

The apparent resistance of a current path is higher if this runs transverse to the fibre direction. In this situation, the fibres behave as perfect insulators leading to a high distortion resistance, which equalises the resistance measured for all paths on the surface. For the unidirectional sample, Fig. 4–18 shows that the resistance along *x* for all values of *y* is 35 Ω. For the [0°,45°] and [0°,90°] samples, however, the apparent resistance remains between 5 Ω and 10 Ω for values of *x* between 10 mm and 70 mm and only at the edge of the sample (*x* = 90 mm) does increase to 15 Ω. This increase along *x* is, however, much less than that observed for the unidirectional sample along the same paths. Indeed, the values in Fig. 4–18 for the unidirectional sample are similar to those for the [0°,45°] and [0°,90°] samples at *x* = 30 mm but diverge between *x* = 50 mm and *x* = 90 mm. Those for the multidirectional samples vary

by less than 10 Ω while the apparent resistances measured for the unidirectional sample increase by more than 20 Ω. For both samples, moreover, most of this increase occurs between x = 70 mm and x = 90 mm. Specifically, as x increases from 30 mm to 50 mm, from 50 mm to 70 mm, and from 70 mm to 90 mm, the increase for the multidirectional samples is 0.3 Ω, 0.4 Ω, and 5.6 Ω, respectively, while for the unidirectional sample, increases respectively of 6 Ω, 5 Ω, and 11 Ω, are recorded. At x = 30 mm, the difference in apparent resistance between the unidirectional and the [0°,45°] and [0°,90°] samples is approximately 6 Ω. For x = 30–70 mm, the apparent resistance of the multidirectional samples varies little around an average value of ~7 Ω. Since the values for the unidirectional sample increase, the difference in apparent resistance between the unidirectional and the [0°,45°] and [0°,90°] increases, from approximately 6 Ω at x = 30 mm, to 13 Ω, 18 Ω, and 22 Ω at 50 mm, 70 mm, and 90 mm, respectively.

4.5 Volume Characterization

4.5.1 Test configurations for volume characterisation

Volume characterisation was performed using two- and four-probe methods. For the two-wire method, initial measurements were collected using the single-point electrical connection soldered at low-temperature using Lipowitz's alloy (see Section 4.8), and thereafter, with the entire length of the sample painted with silver (Fig. 4–19). A subsequent set of measurements was obtained by applying silver paint to the entire electrode, setting a thin and highly flexible wire along the entire length of the sample, and then leaving the paint to cure.

Resistances were calculated from the mean of three measurements, each performed over a minute with current flowing. The interval between successive measurement was at least two

minutes. Voltage versus intensity (V-I) plots were used to examine the dependence (or not) of the resistance on the current intensity.

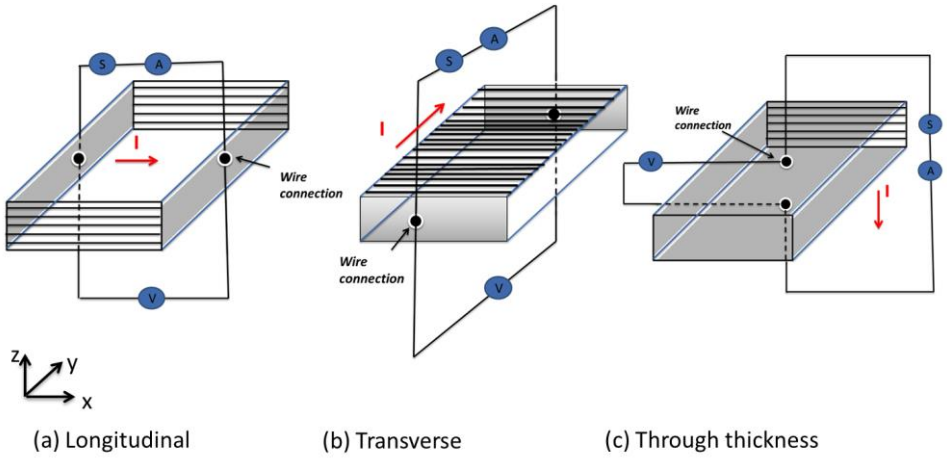

Fig. 4-19. Schematics of the layouts used to measure the (a) longitudinal, (b) transverse, and (c) through-thickness volume resistivity of carbon fibre composite samples using the two-probe method.

4.5.2 Impulse circuit

A Haefely Type 481 recurrent impulse generator capable of delivering up to 500 V was used for the low-current impulse tests. A photograph of the experimental setup is show in Fig. 4–20. The stray inductance effect on the measurement circuit was minimised by carefully connecting the voltage and current leads. Fig. 4–21 shows typical voltage and current profiles measured under impulse injection.

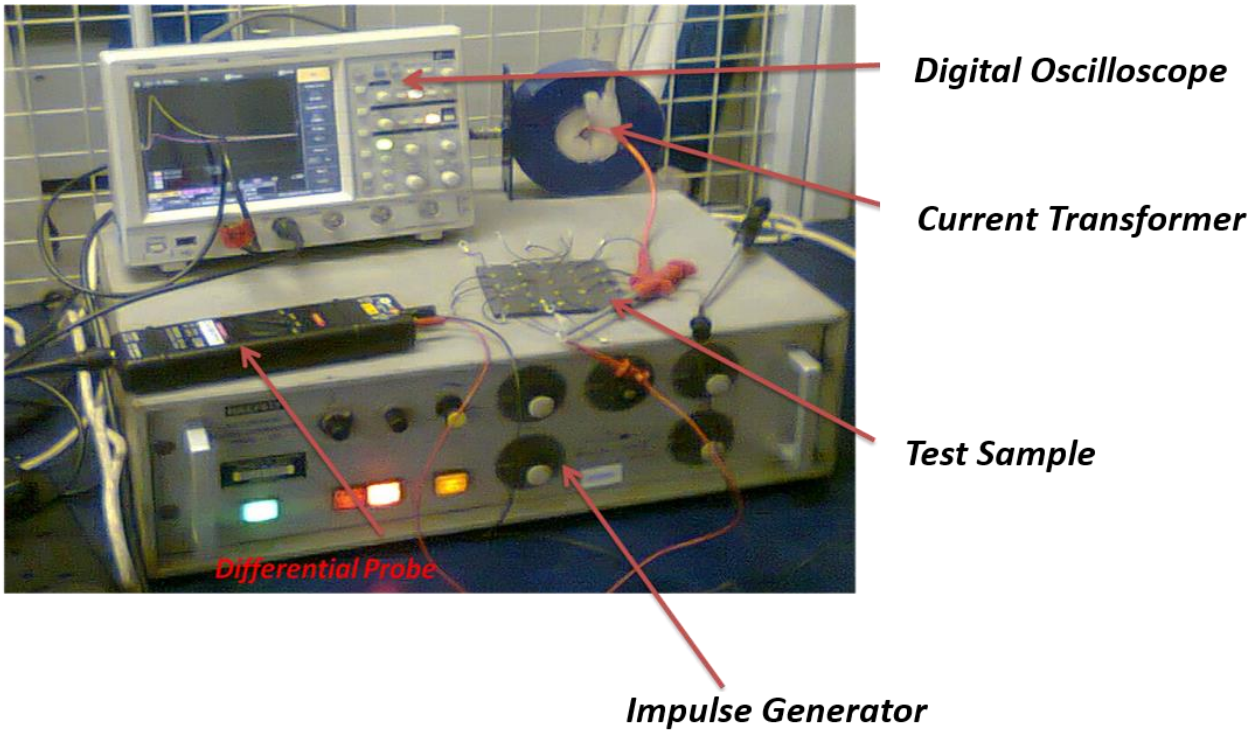

Fig. 4-20. Photograph of the experimental setup used for low-current impulse measurements of the volume resistivity of carbon fibre composites.

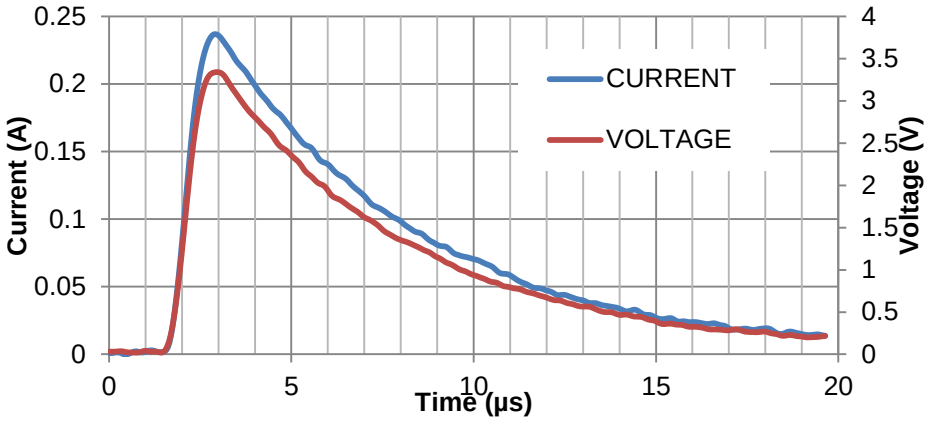

Fig. 4-21. Typical voltage and current vs. time profiles obtained for low-current impulse measurements of the volume resistivity of carbon fibre composites.

The settings of the generator are listed in Table 4-6. The response of the carbon composite test sample is resistive, with instantaneous voltage and current shapes coinciding very well. The impulse resistance was calculated based on the peak current to eliminate any inductive effects in the test and measurement circuits:

$$Z_p = \frac{V_{Ip}}{I_p} \tag{4-6}$$

where V_{Ip} and I_p are the peak voltage and current, respectively.

Table 4-6. Equipment and settings for the test circuit used to measure the volume resistivity of carbon fibre composites.

Equipment type	Model number	Settings
Impulse generator	Type 481 (Haefely Recurrent Surge Generator)	R_p = 6k8, R_s = 10E, L = 0H, C_s = 220nF, C_b = 68nF
Differential probe	DP25 (Pintek)	Attenuation setting = 1/20
Oscilloscope	Leroy Waverunner 64Xi	
Current transformer	Wide Band Terminated Current Transformer Model 58MH100	Voltage to current ratio = 1/10

4.6 Volume characterisation results

The specifications of the samples tested using the two-wire technique are listed in Table 4–7. The measurements on the sample were collected using the method described in Section 4.5. Samples of MTM28-1/T800H-type material were studied in three different sizes and for various ply lay-ups to provide general dimensional-dependent resistance information for carbon composites. Only one sample size was characterised for the remaining composite types. An example of the layer configuration of the samples, obtained by scanning electron microscopy, is shown in Fig. 4–22 for the M21/T800s sample. Note that in contrast with the other studied materials, the MTM28-1/T800H sample did not contain independent resin layers or resin gaps.

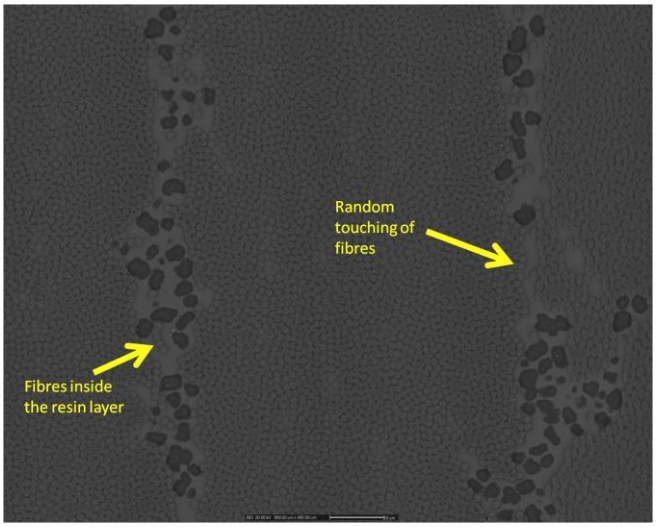

Fig. 4-22. Scanning electron micrograph of an M21/T800s-type carbon fibre composite.

Preliminary investigations were performed using electrodes soldered using Lipowitz's alloy; however, measurements were mainly recorded with silver painted electrodes (RS electronics silver paint) with wires (Farnell high flexibility thin copper wire) running along their entire length.

The directional resistances of samples containing expanded copper foil (ECF) embedded in the top resin layer were also studied. The ply lay-up of this material was identifiable but not its designation. Fig. 4–23 shows the cross-sectional microstructure of this ECF sample. Other ECF samples were separately obtained from DEXMET. bThe electrodes on the ECF-embedded carbon composite samples were formed using RS silver paint. The ECF type used in the sample is 2Cu4-100FA 0.015 psf (73.3 g/m^2), containing diamond in both the short and long directions. A detailed investigation of current penetration into carbon composite panel containing ECF is beyond the scope of this thesis. On account of their configuration, however, the ECF-containing samples are assumed to have anisotropic electrical properties.

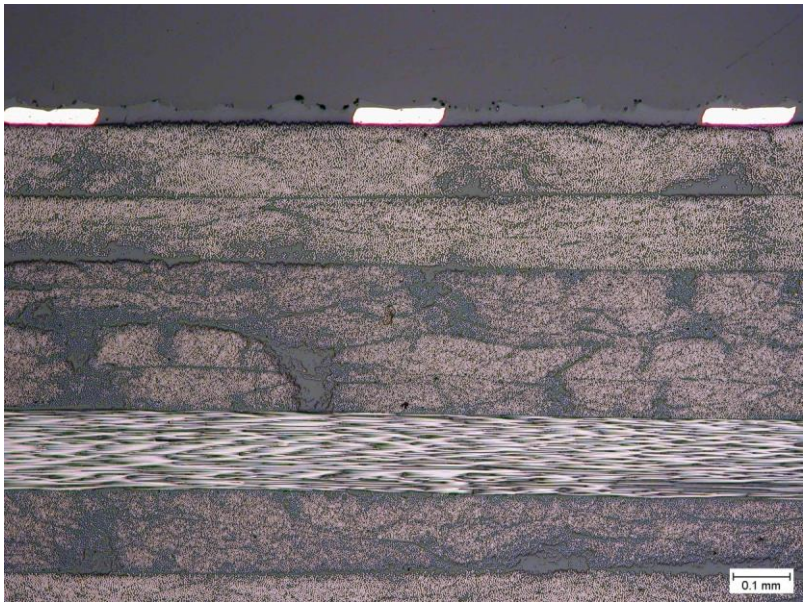

Fig. 4-23. Cross-sectional optical micrograph of a carbon fibre composite with expanded copper foil embedded in the top resin layer.

For the MTM28-1/T800H samples, a detailed analysis of resistance was performed as a function of sample dimensions, with three different sizes investigated per ply lay-up (Table 4–7). The through-thickness resistance of the ECF sample was found to be 9.35 Ω, approximately 19 times higher than the values obtained for the quasi-isotropic samples (0.5 Ω on average). This is because the path of least resistance for the ECF sample is along its surface rather than in the thickness direction.

For unidirectional panels in which all layers are oriented at 0°, the resistances in the longitudinal and in line directions are ~0 and ~29 μΩ, respectively, whereas in the transverse direction, the resistance is approximately 1900 times higher (55 mΩ) due to current flow to the return electrode being impaired by the resin gaps. In the through thickness direction, the resistance is 14 mΩ, 4 times less than in the transverse direction but 483 times more than the longitudinal resistance. The two layered samples have similar longitudinal resistivities, but differ substantially in terms of their transverse and through thickness resistivities.

Table 4-7. MTM28-1/T800H sample dimensions and the areas of the electrodes used for volume resistivity measurements.

Sample Dimensions	Electrode Area (mm^2)		
(cm)	**Longitudinal**	**Transverse**	**Through-thickness**
8 x 2.2 x *t*[a]	2.2 x ***t***	8 x ***t***	8 x 2.2
11x3.3 x *t*	3.3 x ***t***	11 x ***t***	11 x 3.3
15x5.2 x *t*	5.2 x ***t***	15 x ***t***	15 x 5.2

[a] t = 2 mm, 2.5 mm , and 3 mm for the samples containing 16, 20, and 30 plies, respectively.

The conductivities of the different samples are compared in Fig. 4–24. The unidirectional sample has the lowest through-thickness conductivity (0.3 S/m), 23 times less than that of the 5-ply [45°,−45°] oriented sample. The unidirectional sample also has the lowest transverse conductivity, this parameter being maximal for the [0°,90°] panel because the effect of the upper 0° layer is cancelled out by the lower 90° layer, for which the nominally transverse current runs parallel to the fibre direction. For the unidirectional samples, the transverse conductivity is 29 times higher with a 45° than with a 0° orientation, the end-to-end fibres in the 45° orientation acting as efficient current carriers.

The longitudinal conductivities of all the samples are similar (Fig. 4–24), with 3500 S/m, 2449 S/m, 4680 S/m, and 2858 S/m recorded for the unidirectional (0° and 45°), [0°,90°], [0°,45°,90°], and [45°,−45°] samples, respectively. In contrast, the transverse conductivity differs substantially between the different samples; the [0°,90°] panel is the best transverse conductor, followed by the [45°,−45°], [45°,45°], and [0°,0°] samples, with transverse conductivities of 7611 S/m, 1552 S/m, 220 S/m, and 7 S/m, respectively. The through thickness conductivities of the [0°,0°], [0°,90°], [45°,45°], [45°,−45°] are 0.3 S/m, 0.4 S/m, 3.6 S/m, and 7.2 S/m, respectively.

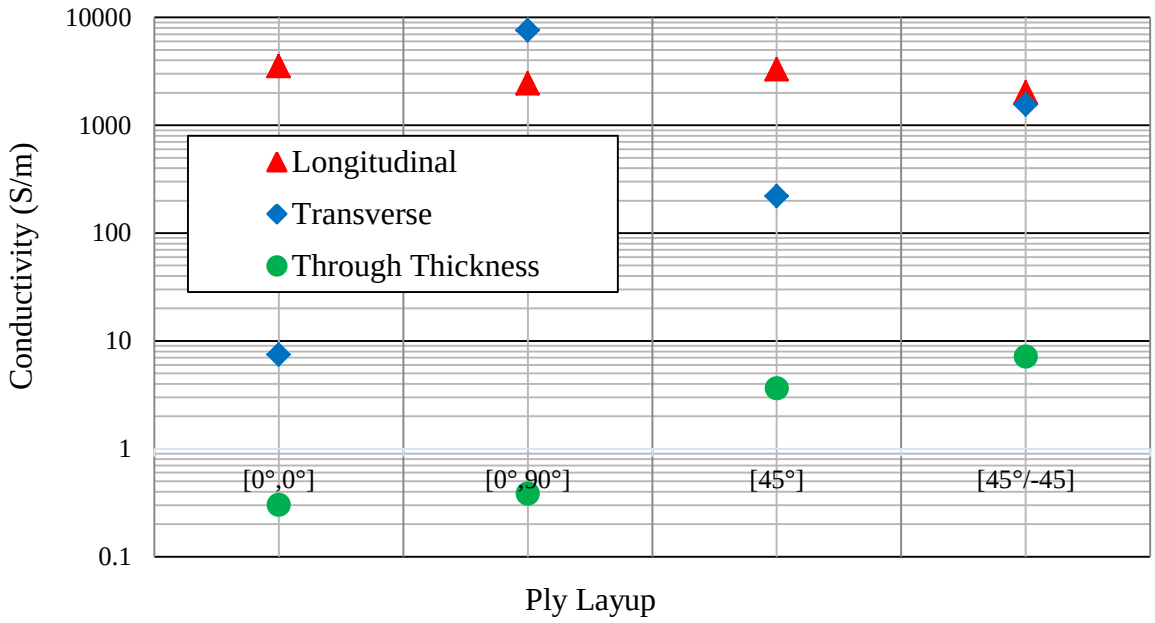

Fig. 4-24. Longitudinal, transverse, and through-thickness conductivity (on a logarithmic scale) of two-layered M21/T800s samples with different ply lay-ups.

4.7 Two-wire measurement of quasi-isotropic ply lay-ups

The DC voltage versus current plots were obtained using two-wire sensing for M21/T800s samples with 16, 20, or 30 plies, as described in Table 4–8. The slope of the lines for the 16- and 30-ply samples is ~0.5 Ω in the through-thickness direction but only ~0.05 Ω in the longitudinal and transverse direction. For the 20-ply sample, the gradients are slightly larger, but the overall trends are observed. This indicates that for these quasi-isotropic samples, the resistance measured in the through-thickness direction is 10 times larger than in the transverse and longitudinal directions.

The AC response of these quasi-isotropic samples was also analysed in all three directions. Fig. 4–25 shows their AC resistivity in the through thickness direction, with similar values obtained at all frequencies. The AC impedance in the through-thickness direction is roughly 10 times larger than the impedance measured in the longitudinal and transverse directions.

4.8 Variable Alternating current circuit

The Cardiff University Impedance Measurement System (IMS) was employed for AC tests for frequencies ranging from 50 Hz to 100 kHz. A single digital signal processing lock-in amplifier stage was used to generate a sinusoid (<1 V root mean square (rms)), which was fed to the input of the power amplifier stage. The output of the power amplifier was then connected across the test specimen.

Voltage measurements were collected using a LeCroy Waverunner 64Xi; no moving average filter was used on the inputs. Functions programmed into the oscilloscope were used to determine the cyclic rms currents and voltages. These quantities were then used to determine the V-I characteristics of the specimen. Electrode currents from 50 mA to 1 A were applied to the sample at each of the predefined test frequencies (viz. 20 Hz, 52 Hz, 100 Hz, 1 kHz, 10 kHz, and 100 kHz). Specimen heating was minimised by using a very short excitation duty (approximately 10%).

The phase angle of the wave for a frequency scan of unidirectional sample is slightly negative (−4.04°) at 20 Hz, increases up to 3.93° at 5 kHz, and then decreases to 1.25° at 100 kHz. Large and small phase angles are respectively indicative of capacitive and resistive behaviour in a circuit. The behaviour of the unidirectional CFRP sample studied here is therefore purely resistive.

Table 4–10 shows that the values obtained here for the conductivity of these quasi-isotropic samples are different from those reported elsewhere in the literature [51], but nonetheless of the same order of magnitude. Note that the inherent variability of the material and the fact that the samples investigated were not identical in size mean that differences between the datasets are expected. In the longitudinal and transverse directions the measured resistivity is

the sum of the resistivity of each ply. These contributions have to be taken into account due to the presence of diagonal layers. The ρ resistivity is given by [51]

$$\rho = \frac{R_{measured}}{l}\left[\langle A\rangle_{1st\ ply} + \langle A\rangle_{2nd\ ply} + \cdots \ldots \ldots \ldots \ldots \ldots \ldots \langle A\rangle_{last\ ply}\right] \quad (4\text{-}7)$$

This expression takes into account the different effective areas of the conducting diagonal layers. This can be derived from measurements performed on one sample, for example (45,135,0,0,90,0,135,0) s, for which the longitudinal and transverse resistances are 21 mΩ and 116 mΩ, respectively. In the transverse (longitudinal) direction, the electrode spacing (length) is 58 mm and the electrode length (spacing) is 20 mm (see Fig. 4–19). For a top 45° layer, the longitudinal direction runs parallel to the width of the sample, as shown in Fig. 4-2(c) in Section 4.3. The sample is 4 mm thick; therefore, each of the 16 plies is 0.25 mm thick. The longitudinal resistivity ρ_{long} of a quasi-isotropic sample such as this is therefore [51],

$$\rho_{long} = \frac{0.021}{0.020}\left[(N_d * t_d * \sqrt{2} * 0.058) + (N_o * t_o * 0.058)\right] \quad (4\text{-}8)$$

where N_d and t_d and N_o and t_o are the number and thickness of the diagonal and non-diagonal plies, respectively. The scaling factor for a [45°,135°] sample is √2, for which Eq. (4-8) gives the resistivity as 2.8×10^{-4} Ω·m, and therefore, the conductivity as 3.6×10^{3} S/m in the longitudinal direction

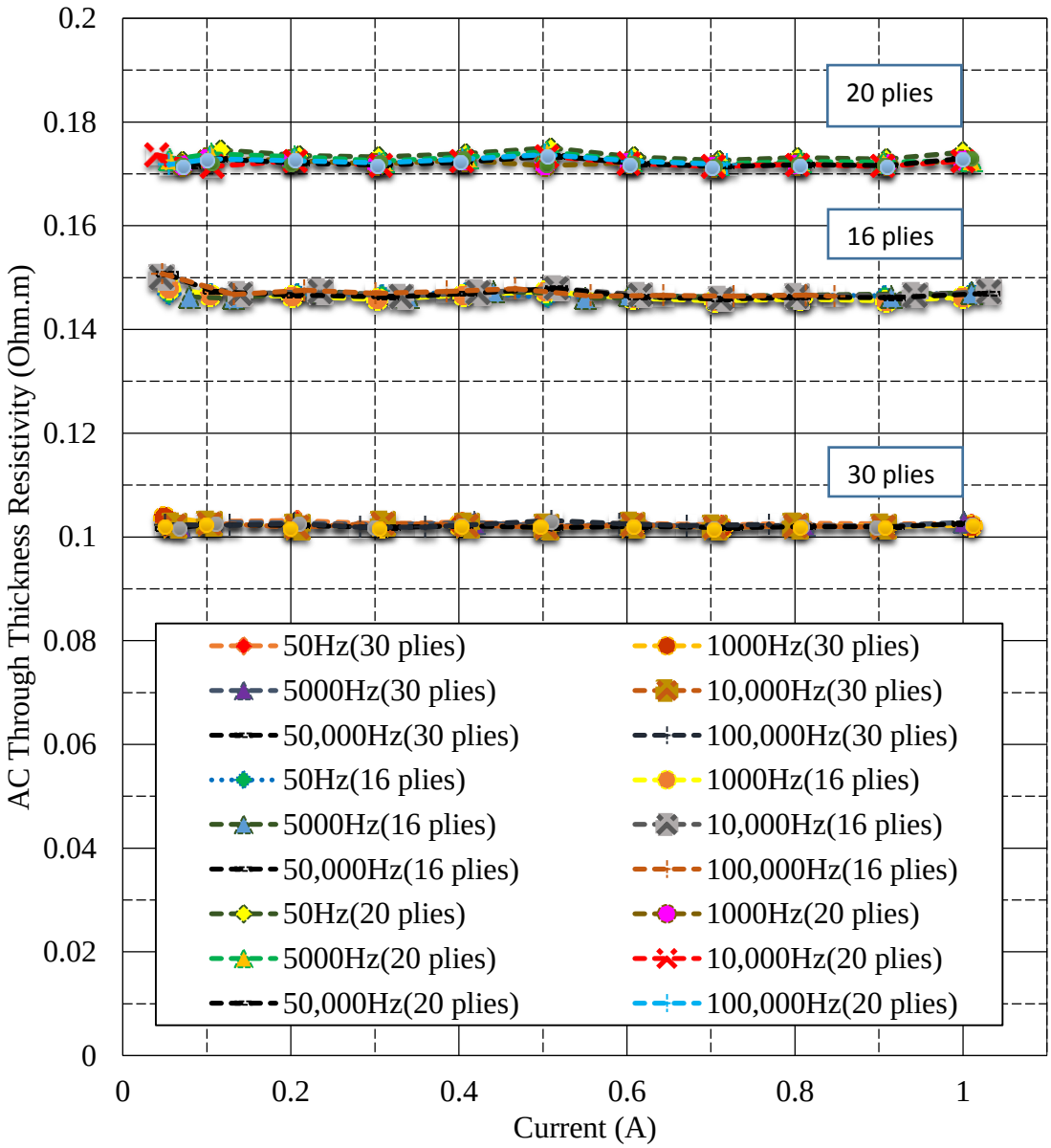

Fig. 4-25. AC through-thickness resistivity at different frequencies of different quasi-isotropic M21/T800s samples as measured by two-probe sensing.

In the transverse direction, the conductivity for the [45°,135°] layers is assumed to be zero (see Fig. 4.2(b)), such that only the 90° layers, in line with the current path, will conduct. In the longitudinal direction in contrast, the same 90° layers will be non-conducting plies, while the [45°,135°] and 0° layers will conduct. For another 16-ply lay-up, (45,90,−45,0,45,90,−45,0)s for example, the longitudinally conducting plies will be the [45°,−45°] and 0° ones, with an electrode length of 30 mm and an electrode spacing of 10

mm, giving a resistance of 33 mΩ in the longitudinal direction. There are 8 diagonal layers out of the 16 in total and the ply thickness is 0.25 mm. The resistivity calculated using Eq. (4-8) is, therefore, 0.48 mΩ·m, corresponding to a conductivity of 2.1×10^3 S/m. Table 4–10 shows that the 20- and 30-ply samples have transverse conductivities of the same order of magnitude as the longitudinal conductivities reported by Piche et al. for unknown number of plies composite [51].

Table 4-10. Directional conductivities of quasi-isotropic samples with different ply lay-ups as measured here and as reported in the literature [51].

σ (S/m)	16 plies[a]	16 plies[b]	20 plies	30 plies	σ (S/m) [5**1**]
σx	3.6×10^3	2.1×10^3	1.2×10^3	153	40×10^3
σy	682	6.3×10^3	27×10^3	17×10^3	165
σz	15	7	6	10	50

[a](45,90,-45,0,45,90,-45,0)s
[b](45,135,0,0,90,0,135,0)s

4.9 Two-wire resistivity measurements for cross-ply laminates

The resistivity measurements reported in this section were obtained from laminates (without ECF) with ply lay-ups of (0,60,60,60,60,0) and [(0, 90)4]s. The resistances measured in the longitudinal, transverse, and through-thickness directions for the (0,60,60,60,60,0) laminate are 0.038 Ω, 0.28 Ω, and 0.173 Ω, respectively. For the cross-ply laminates, the corresponding values are 0.0235 Ω, 0.0665 Ω, and 0.26 Ω, respectively. Furthermore, the conductivities measured for the cross-ply laminates were 9.0×10^3 S/m, 18×10^3 S/m, and 4 S/m, in the longitudinal, transverse, and through-thickness directions, respectively. For the (0/60/60/60/60/0) laminate, the conductivities were calculated by accounting for the area scaling factor described in the preceding section, giving 11×10^3 S/m, 8.5×10^3 S/m, and 4 S/m, respectively, in the longitudinal, transverse, and through-thickness directions.

4.10 Non-destructive electrical characterisation under lightning impulse currents of less 100A

Tests were conducted using two types of electrodes. Silver-paint gap electrodes were used according to the ASTM D257 standard (Fig. 4–26). This setup was compared with aluminium electrodes embedded in the panels after manufacturing. The middle electrode was aerospace fastener EN6115V4-5, which has a nominal diameter of 6.3 mm. The rivet electrodes (6.3 mm in diameter) on the edge of the sample were placed at 22.5° intervals and a crown ring was fitted through the rivets. The dimensions of samples were 150 mm × 150 mm × 2 mm. A third set of samples was prepared with an embedded-electrode design but without the metal ring and with smaller (3.2 mm) rivets. These samples were 100 mm × 100 mm in size. A total of 41 samples were tested under both low and high current intensities. A subset was also characterised under high-DC intensity.

4.10.1 Concentric ring electrode tests

4.10.1.1 Silver-painted electrodes

The electrodes for this test were prepared according to the ASTM D257 standard. A gap electrode was used for the top surface, whereas the bottom electrode covered the entire surface of the sample. The central electrode was four times the thickness of the panels and the gap between the top two electrodes was at least twice the thickness of the panels. Measurements were collected in the through-thickness direction. For this configuration, the area of the sample is given by,

$$A = \frac{\pi(D1 + g)^2}{4} \tag{4-9}$$

where *D*1 is the diameter of the central electrode on the top surface and g is the width of the gap between the central and outer electrodes. The resistivity is then calculated using

$$\rho_v = \frac{A}{t} R_v \tag{4-10}$$

Concentric electrodes avoid electric field fringing on the edges of the sample. For direct currents, R_v in Eq. (4-10) is equivalent to the measured resistance. For impulse currents however, R_v corresponds to the resistance at peak current magnitude, which may not be the maximum resistance. The different ply lay-ups characterised in these tests are listed in Table 4–11.

The results obtained under increasing lightning current magnitudes (0–80 A) are presented in the following sections.

4.10.1.2 Unidirectional sample

Lightning impulses at current intensities of up to 80 A were injected into a unidirectional sample in which all layers were oriented at 0° using the guard electrode setup. The electrodes for this test were prepared using silver paint. The gap between the electrodes was 10 mm and D1 and D2 were equal to 80 mm and 10 mm, respectively (see Fig. 4–26). Fig. 4–27 shows that the resistance at peak current decreases as the peak current increases, from 1 Ω at ~2 A down to 0.8 Ω at 80 A, which is equivalent to a 20% decrease in the impulse resistivity of the sample. The voltage increases linearly with the peak current intensity.

Table 4-11. Sample specifications for concentric ring electrode tests for silver-painted samples.

Ply Lay-up	Number of plies	Material Type	
		M21/T800s	**MTM28-1/T800H**
45/-45	10	√	
45	10	√	
0,60,60,60,60,0	6	√	
0,90,90,90,90,0	6	√	
[0/90/90/0/+45/-45/0/90]s	16	√	
[0/90/90/0/+45/-45/0/90/90/0]s	20	√	√
(45,135,0,0,90,0,135,0,0,135,0,90,0,0,135,45)	16	√	√
(45,90,-45,0,45,90,-45,0)s	16	√	
[(0/90/90/0/+45/−45/0/90/90/0/-45/+45/0/90)(0/90/90/0/+45/−45/90/0/90/0/−45/+45/0/90/90/0)]	30	√	√
0,90,0,90,90,0,90,0	8	√	
0	20	√	
0,90	20	√	
0,45	20	√	
0,45,90	30	√	

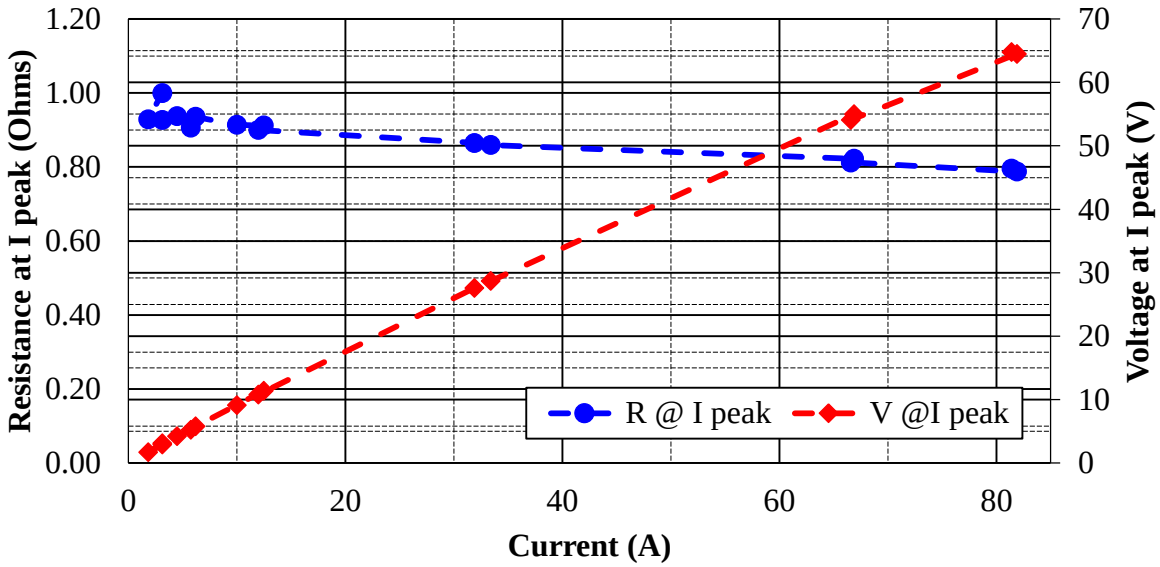

Fig. 4-27. Resistance and voltage at peak current vs. current magnitude for a unidirectional carbon fibre composite sample, as measured with silver-painted concentric ring electrodes.

This electrode configuration provides an estimate of the through thickness resistance of the sample and avoids the fringing effects incurred when full metal electrodes are used.

4.10.1.3 Three-layered sample

Fig. 4–28 shows that the resistance of the three-layered sample [0°,45°,90°] follows the same trend with increasing current intensities as that shown in Fig. 4–27 for the unidirectional sample. The resistance decreases from 2.3 Ω at a peak current of 10 A to 1.9 Ω at 65 A, a similar relative decrease (~20%) as for the unidirectional sample. For this sample, the gap between the electrodes was 16 mm and D1 and D2 were 30 mm and 10 mm, respectively.

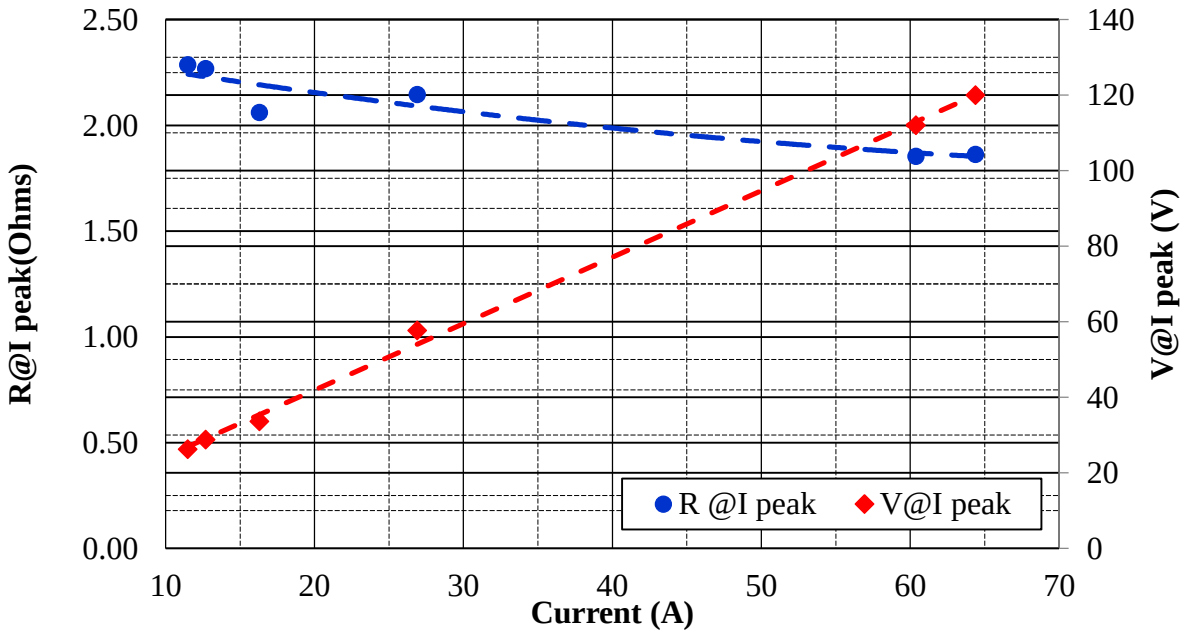

Fig. 4-28. Resistance and voltage at peak current vs. current magnitude for a three-layered carbon fibre composite sample, as measured with silver-painted concentric ring electrodes.

Resistivity measurements were also performed using the guard electrode setup on a sample with a [0°,90°] lay-up. Figs. 4–29 and 4–30 summarise the results obtained for the three samples with different ply lay-ups (viz. unidirectional, [0°,90°], and [0°,45°,90°]). Fig. 4–29 shows that the resistivity is stable up to 1 A of DC current. In Fig. 4–30, however, the resistivity decreases as the peak intensity of the impulse current increases. The through thickness resistances for undamaged unidirectional and [0°,45°,90°] samples are 1 Ω (Fig. 4–

27) and 2.3 Ω (Fig. 4–28) respectively. The voltage in the three-layered sample is ~120 V for a 60 A impulse (Fig. 4–28), while for the unidirectional sample, the voltage is 66 V for a 80 A impulse (Fig. 4–27).

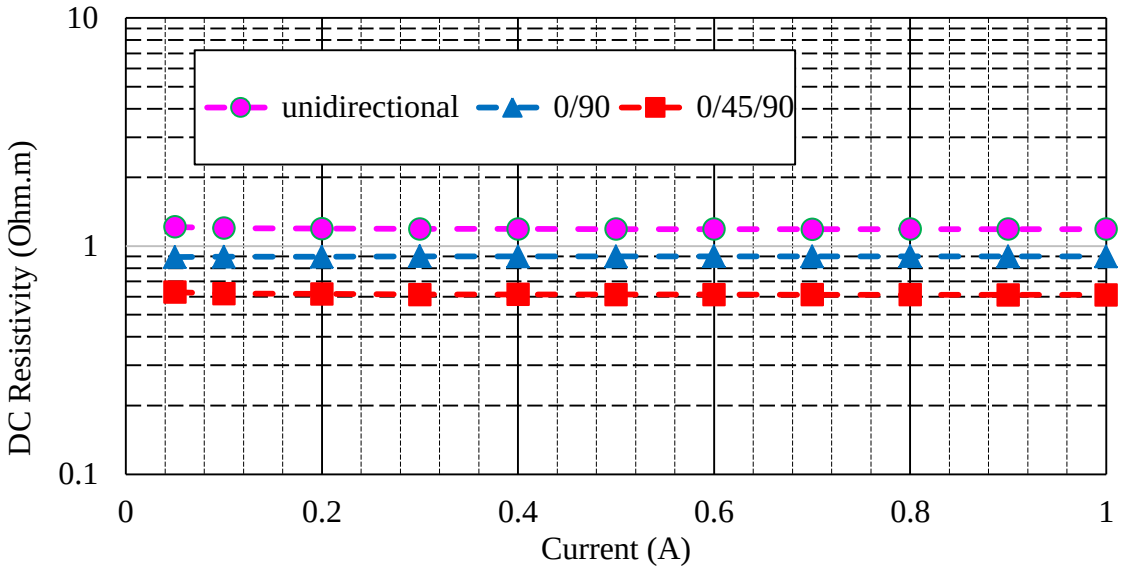

Fig. 4-29. DC resistivity of unidirectional, two-layered, and three-layered carbon fibre composite samples as a function of current magnitude, as measured with silver-painted concentric ring electrodes.

The voltage profiles in Figs. 4–27 and 4–28 remain linear up to high current intensities, indicating, therefore, that no breakage occurred. The DC resistance is, however, not sensitive to delamination or matrix cracking.

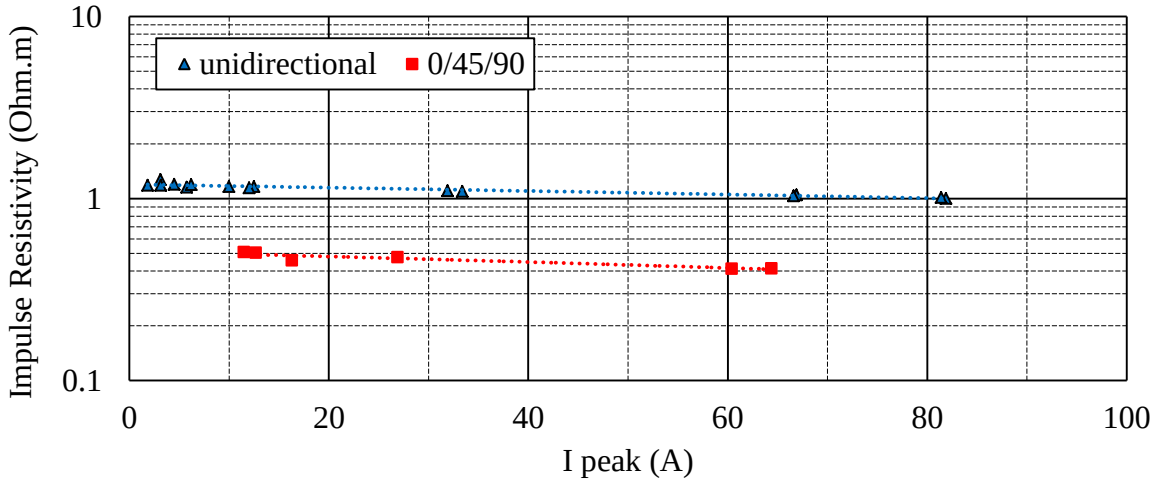

Fig. 4-30. Impulse resistivity of unidirectional and three-layered carbon fibre composite samples as a function of the magnitude of the current impulse, as measured with silver-painted concentric ring electrodes.

Fig. 4–30 highlights a decrease in impulse resistivity of ~17% both for the unidirectional and three-layered samples. (Note that the DC resistivity of the same samples decreases by ~20% over a similar current magnitude range). This decrease in resistivity is believed to stem from the dissipation of the energy from the lightning impulses.

4.10.1.4 Samples with embedded electrodes (category 1)

The metal-ring electrodes (see Fig. 4–31) used for this part of industry. All samples were tested under direct and impulse currents up to 100 A in the lower voltage test range, then tested at current magnitude up to 350 A. (The results of the latter tests are discussed in Chapter 5) All samples in this category had ply lay-ups of (45,135,0,0,90,0,135,0) and measured 150 mm × 150 mm × 2 mm.

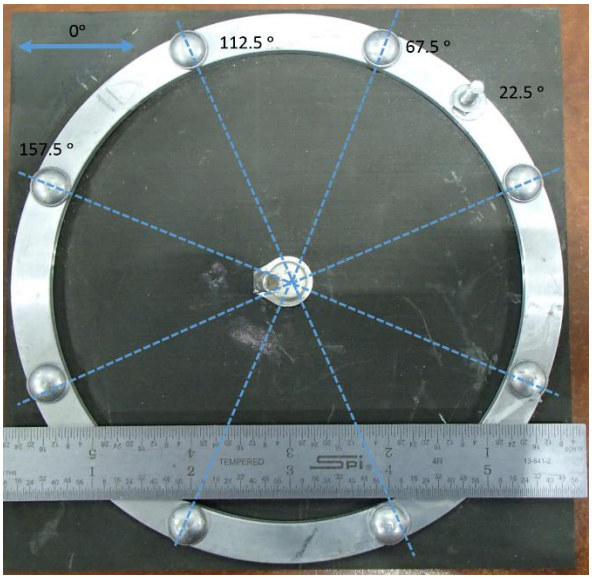

Fig. 4-31. Photograph of a metal ring electrode sample

Fig. 4–32 shows that the resistance variation with magnitude current. This increase is, however, non-linear for intensities above 80 A. No particular trend is discernible in Fig. 4–32

for the impulse impedances, which remain between 0.09 Ω and 0.07 Ω over the whole current range.

Fig. 4–33 shows that energy dissipated in these samples increases non-linearly with the peak intensity of the current impulse. The non-linear increase in the energy dissipation explains

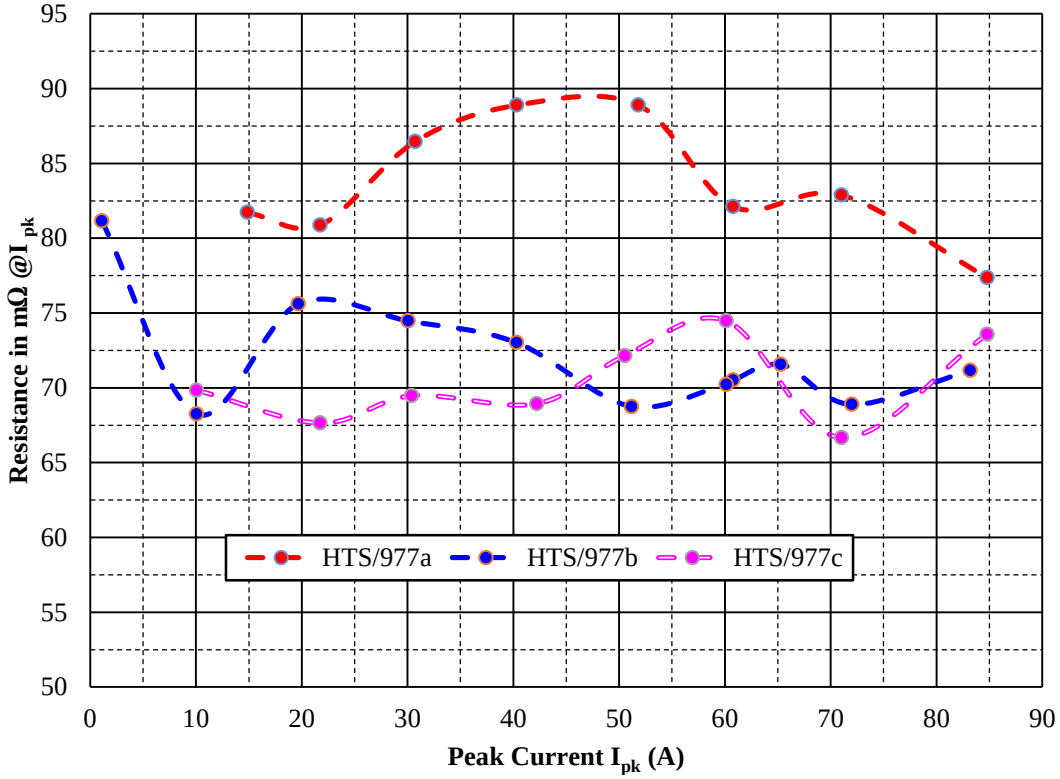

how high-intensity lightning strikes can inflict substantial damage to aircraft components.

Fig. 4-32. Resistance peak current vs. current magnitude for different metal-ring carbon fibre composite samples with an embedded electrode.

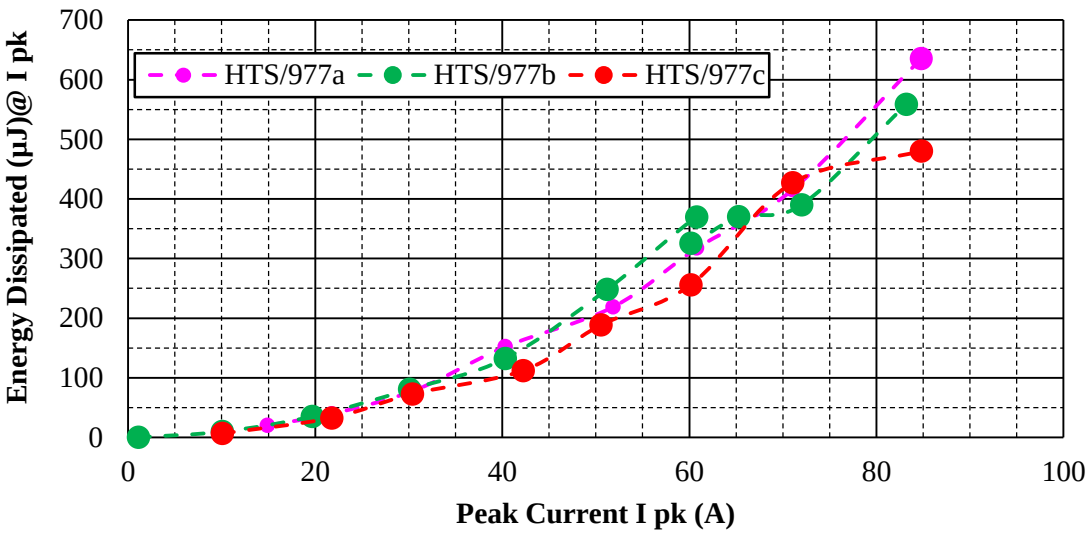

Fig. 4-33. Energy dissipated at peak intensity vs. current magnitude in different metal-ring carbon fibre composite samples with an embedded electrode.

4.11 Conclusions

In this chapter, surface and layer characterization for variable ply lay-ups was performed. A novel method of surface characterization was developed which measured the sum of electrode Re and material resistance Rm, as the apparent resistance. The parasitic resistance Re then includes the contact resistance of the electrode and the distortion resistance due to the current distortion. For a unidirectional panel, the current path crosses the resin gaps between fibers, which explains the relatively high values of resistance Rm and Re for current injection transverse to fiber direction. For Configuration 2 (longitudinal), however, the resistances Rm and Re were considerably lower. These lower ranges are expected as the current flow is along the carbon fibers. Same trends in resistances were observed under impulse energization mode.

The directional conductivities of quasi-isotropic composite samples were determined experimentally under three different energization modes, AC, DC and impulse and found to be comparable with values published elsewhere in the literature. Different ply lay ups were

used for testing including that from 16 plies to 30 plies maximum, electrodes for volume electrical conductivity were made using silver paint and a thin flexible wire.

The through-thickness resistivity was also measured using tests with guard electrode. The results suggest that the resistivity decreases under lightning impulse currents of increasing magnitude up to 80 A. Two other experimental configurations were also studied, on thinner and thicker panels, with and without metal ring electrodes. The thicker samples were obtained from T-joint panels containing ECF.

Chapter 5

MECHANISMS OF DAMAGE PROPAGATION IN CARBON COMPOSITES UNDER HIGH IMPULSE CURRENT MAGNITUDES AND DC CURRENT

5.1 Introduction: Damage to carbon fibre composite parts/structures due to lightning strikes

The different types of damage caused by lightning strikes to aircraft have been recalled/summarized by Uman and Rakov [56]; they are generally due to the flow of the discharge current that induces or aggravates structural deformation through burning, eroding, and/or blasting. To predict the type and extent of this damage, carbon fibre reinforced composite (CFRP) parts can be modelled and simulated using appropriate software, e.g. as in [8]. Chapters 1 and 2 of this thesis describe the structure of carbon fibre composites, and consider their behaviour under lightning strike. Carbon fibre composites are good electrical conductors in the direction parallel to the orientation of the fibres, but poor conductors in directions orthogonal to this. Indeed, the epoxy used as a filler between the fibres has a high resistivity such that the conductivity between and across layers is much lower than along them [8]. Earl has modelled the behaviour of CFRP structures and skin under both direct and indirect lightning effects [8]. His study reveals that the properties of CFCs depend on the characteristics of the underlying material and that numerical modelling is an effective tool to understand their electromagnetic properties.

To evaluate the direct effects of lightning strikes, Earl [8] presents a model that represents a test T-joint with an aluminium spar and CFC skin with additional foil for lightning protection. In the original study [8], the model was meshed with different layers of cells, with the tested CFC panel aligned with the mesh to reflect its anisotropic conductivity. For the sake of simplicity, only flat panels were modelled. However, a study of curved panels would have been more interesting. The goal of the aforementioned study was an estimate of lightning-induced damage in T-joints. The results obtained demonstrate that changes in the measured waveforms can be predicted from the sum of resistances between the return conductor and the spar. Furthermore, Earl [8] also outlines how these models can be used to predict the electromagnetic properties of CRFP panels with arbitrary structures.

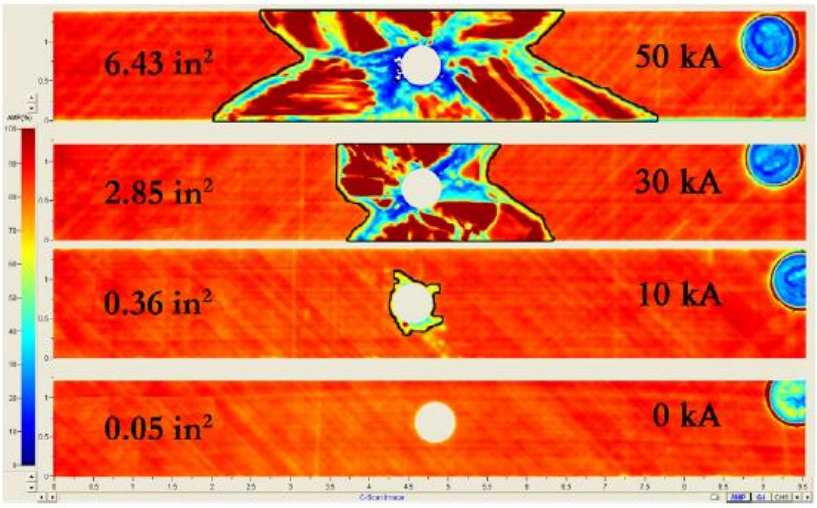

Fig. 5-1. C-scans of filled-hole composite samples tested at different levels of current intensity [57].

Feraboli and Miller [57] studied un-notched and filled-hole CFRP samples under different lightning current magnitudes (viz. 10 kA, 30 kA, and 50 kA). The mechanical properties of these samples were then tested to estimate the extent of the damage. Fig. 5–1 shows the extent of the damaged areas for a filled-hole sample subjected to currents of 0 A, 10 kA, 30 kA, and 50 kA (32 mm^2, 232 mm^2, 1839 mm^2, and 4148 mm^2, respectively). The authors

concluded that the damage in the filled-hole sample was greater at high currents than that in the un-notched samples, which is clearly shown in Fig. 5–1. For the un-notched sample, the damage was only a few plies deep. However, for the filled-hole sample, the damage spread either throughout the fastener or to the entire lamina lay-up. The types of damage reported included vaporisation of the resin and inter- and intra-ply arcing. However, the authors did not investigate damage types and mechanisms, which is a primary concern in this field. The main objective of the tests performed by Feraboli and Miller [57] was an improved understanding of the effects of a metal fastener on CFRPs during lightning strikes. Indeed, two of the most important factors in estimating the damage to a CFRP panel are the position of the metallic fastener and the conductivity of the constituent materials.

The standard samples used by Feraboli and Miller [57] (as defined by Boeing) to measure residual strength were very small (304 mm × 38 mm), which introduces complex finite-width effects in the calculations of damage and of the residual strength. This is a limitation of their work. Indeed, the results obtained in their study cannot be extrapolated to larger panels because of the finite width of the samples, which constrains the formation of damage and its propagation.

Hirano et al. [58] investigated the damage in CFRP samples subjected to artificial lightning strikes. The types of damage they recorded included fibre damage, resin deterioration, and delamination. The authors [58] concluded that the anisotropic electrical properties of the graphite/epoxy laminate affected damage propagation in the in-plane direction in each layer. These results, therefore, indicate that the behaviour under lightning strikes of CFRPs is strongly related to their electrical properties. However, they in their study [58] neglected the influence of the stacking sequence of the constituent materials, the testing samples all being composed of the same materials arranged in the same stacking sequence. Therefore, more

work is needed to understand the effects of different materials and stacking orientations on the damage caused to CFRP panels by lightning strikes.

Fig. 5–2 shows the damage resulting from a lightning strike on a Transcowl composite [59]. The damage was inspected using ultrasonic techniques, which revealed that the sliders, track lines, and impact zones all experienced superficial burns, as is clearly seen in Fig. 5–2. The damaged area covered approximately 160 mm × 210 mm in the vicinity of the impact site. The delamination zone was 68 mm × 45 mm across and 1.4 mm deep. Prominent burns were also found in the bronze mesh surface.

Fig. 5-2. Photograph of a Transcowl composite sample after a lightning impact test [59].

Baldacim et al. [59] focused on protecting carbon fibre composites by providing an adequate path for the current to pass through the aircraft structure without causing any major damage therein. According to the same authors, three basic phenomena that can disturb the operation of an aircraft are lightning (direct and indirect effects), electromagnetic interference, and electrostatic discharge [59]. The work in this thesis focuses on the effects of lightning. During a lightning strike, sound shockwaves may damage CFC skins and can lead to pyrolysis of the resin. Testing techniques and configurations need to be defined for CFRP samples in order to

predict the damage induced by direct and/or indirect lightning effects. Some of these are discussed in the following section.

5.2 Protecting carbon fibre composites against lightning strikes

Carbon fibre composites are typically surface-protected against lightning attachment. The usual procedure is to apply a thin metallic layer in the form of mesh or foil on the outer layer. In the event of lightning attachment, this outer layer is designed to vaporise the damage leaving the inner CFRP layer undamaged. An insulating layer can also be added between the CFRP layer and the mesh or foil layer, preventing current flow into the carbon layer at the arc root. With this method, the underlying CFRP skin is also protected from arc heat. Although these approaches provide a certain level of protection, some current flow into the CFRP layers is still possible, as is the damage it entails for the carbon fibres. An alternative approach is to use copper as the metal layer and aluminium as the protective layer; in this arrangement, however, corrosion is likely between the aluminium and carbon layers. The mesh or foil layer has to be at least 20 μm thick to provide adequate protection. Haigh [60] has tested different lightweight composites and metallic panels under lightning strikes. Comparing the resistance of painted and foil-covered panels, the results of Haigh's study show that paint aggravates the explosive effects of lightning strikes, leading to greater structural damage. The conclusion of this study is, therefore, that foil and wire protection is preferable.

Baldacim et al. [59] detail the ideal design for protecting CFC parts from a lightning strike based on the fact that CFC laminates used in aircraft skins have thicknesses of 0.5–5 mm. According to these authors, the design objectives for CFC parts/structure protection are as follows.

- Parts designed for zones 1A, 2A, 1B, and 2B should be protected from serious damage, including puncturing and cracking at the attachment points.
- Damage should be prevented at T-joints by providing an adequate path for the lightning current to flow. This is of particular importance for carbon fibre composite fuel tanks and must be established without any arcing and sparking to avoid ignition of the fuel vapours therein.
- Protection from electromagnetic interference and indirect lightning effects should be designed in accordance with the necessary protection of carbon fibre composites from direct effects of lightning.

As explained in [59], the CFC parts in an aircraft that require protection from lightning effects include the following:

- fuselage pressure hull;
- engine nacelle and pylons;
- flight control surfaces;
- avionics bays; and
- fuel tank skins.

However, the CFC tail cones, non-pressurised fuselage, and landing gear doors do not require lightning protection. As stated above, the primary objective of lightning protection is to provide a sufficient number of conductive paths for the lightning current to flow safely through the airframe, inducing no hazard or damage through its combined effects to the aircraft [59].

As discussed in Section 4.3, lightning strikes typically lead to the vaporisation of the resin, de-lamination of the fibre layers, and arcing due to the ionisation of the trapped air between the metal fastener and the carbon fibre composite.

5.3 Experimental procedure for high current tests

Low-voltage measurements provide useful information regarding the electrical resistance of a given material. However, experiments performed under high current magnitudes are important in this context to test for damage via changes in pre- and post-strike resistance values. The tests for this section were, therefore, performed in three stages:

A. Impulse tests with mid-range magnitude currents ranging from 50 mA to 350 A on the samples listed in Table 5-1.
B. Impulses tests based on waveform D with currents ranging from 30 kA to 100 kA on the sample detailed in Table 5–2.
C. Direct current tests at 10 A on the samples listed in Table 5–3.

The samples in categories A and B were tested respectively at the Cardiff University High Voltage Lab and Morgan Botti Lightning Lab (MBLL).

Table 5-1: Details of the samples tested under impulse currents in the 50–350 A range.

Ply Lay-Up	No. of Plies	Material Type	No. of Samples	ECF
[(0,90)4]s	16	Hexcel 914	1	x
(45,135,0,0,90,0,135,0) s	16	M21/T700s	1	√
[0/90/90/0/+45/−45/0/90/90/0]s	20	MTM28-1/T800H	1	x
(0,45,90,-45)s	8	M21/T700s	3	x
(0,45,90,-45)s	8	977-2/HTS	3	x
0	20	M21/T800s	1	x
0,90	20	M21/T800s	1	x
0,45,90	20	M21/T800s	1	x
0,45	20	M21/T800s	1	x

Table 5-2: Details of the sample tested using waveform D impulses.

Ply Lay-Up	No. of Plies	Material Type	ECF
0	20	M21/T800s	x

Table 5-3: Details of the samples tested under 10 A direct current.

Ply Lay-Up	No. of Plies	Material Type	No. of Samples	ECF
[(0,90)4]s	16	Hexcel 914	4	x
(0,45,90,135)s	16	M21/T700s	4	√

The configuration used for current testing up to 350 A is shown in Fig. 5–3. The current was injected using a Ferranti current generator. The potential was measured using a voltage divider and the current magnitude using a current transformer with a 10 V/A sensitivity. All data was recorded on a Lecroy digital oscilloscope. The metal ring electrode was grounded. The tests were conducted with one current injection per charging voltage level Vc. At Vc=48 kV, the digital oscilloscope indicated 350 A for most carbon composite samples. The Ferranti generator was set to deliver up to 50 kV, corresponding to maximum peak currents of 350 A.

Although, there was no significant difference in terms of the maximum current magnitude in the thinner or thicker samples, owing to the presence of resin in the thicker samples, the corresponding voltage graphs showed evidence of electrical breakdown due to electrical discharges.

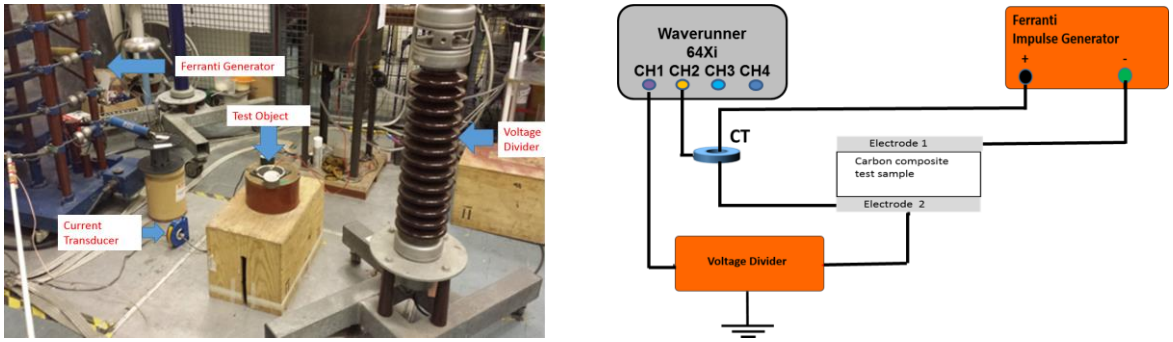

Fig. 5-3. Photograph of the experimental setup for high-current testing in the Cardiff High Voltage Lab (left) and schematics of the experimental set up (right).

5.4 Impulse current tests (up to 350 A)

For these samples, the current was injected in the middle fastener and the outer metal ring was used as the return electrode. The two-layered samples in this category were tested without a metal ring joining the rivets – the current was injected diagonally using one rivet-fastener pair – and clearer voltage signals were obtained than for the quasi-isotropic samples. As before, a charging voltage of 48 kV was used and the current was delivered through a Ferranti current generator. All quasi-isotropic samples exhibited similar responses. The voltage magnitude across the sample is expected to be very small. Therefore, electromagnetic interference dominates and is clearly visible through the measured high frequency oscillations (see Fig. 5–4). It was observed that the thickness of the samples made no significant difference on the maximum current that could be injected.

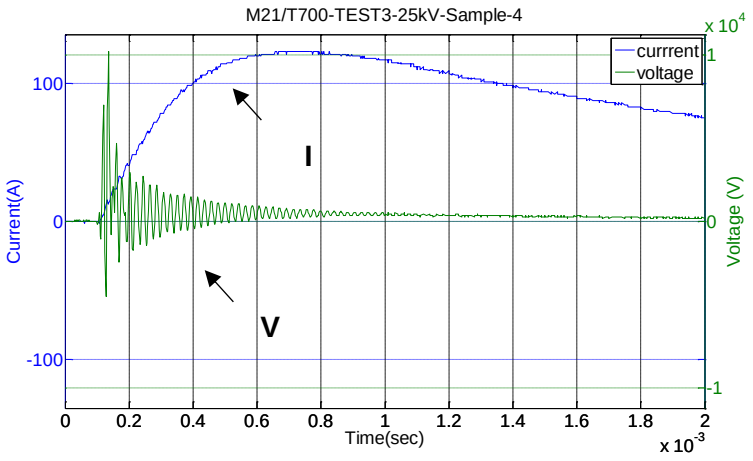

Fig. 5-4. Measured impulse voltage and current traces of a M21/T800s-type sample with a [0°,45°,90°] lay-up (generator charging voltage of 25 kV)

The current impulse shape generated using a Ferranti generator differs from that delivered by a Haefely generator. The rise time for this waveform is 1.2 µs.

5.5 Metal ring samples subjected to 350 A impulses

The samples tested under repetitive lightning impulses in section 5.3 and 5.4 at MBLL were subsequently examined using mechanical 4-point bending tests. As shown in Fig. 5–5, the metal-ring samples were divided into several smaller sections to obtain mechanical strength (flexural modulus) maps, an example of which is shown in Fig. 5–6. The mechanical strengths measured on both sides of the samples extracted with a 90° top layer were found to be similar because the two sides of the panel are mirror images of one another. However, the measurements obtained for either face of the samples with a 0° top layer were found to differ. The microscopic damage in the fastener area of the same sample was studied (no bending tests were used), revealing cracking beneath the fastener that extended down to the eighth ply, but did not propagate throughout the sample.

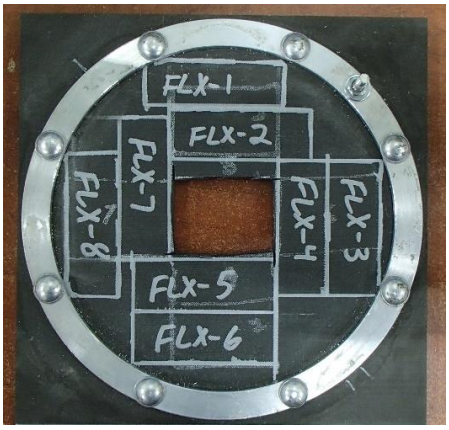

Fig. 5-5. Photograph showing the different mechanical testing regions on a sample with a metal ring electrode previously subjected to a 350 A impulse.

The total elongation/deflection at failure was also recorded for these samples, as plotted against their flexural strength in Fig. 5–7. The samples with a 90° top layer have a lower flexural modulus and a greater elongation at failure than those with a 0° top layer.

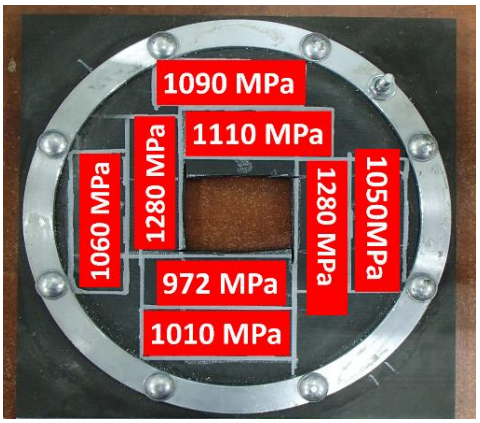

Fig. 5-6. Flexural strength map for a metal ring electrode sample previously subjected to a 350 A impulse.

This analysis shows that impulses in the 300 A range do not have a substantial effect on the mechanical strength of carbon fibre composites. Higher-intensity (kA) impacts are, however, expected to cause sufficient damage for this to be reflected in a degraded mechanical strength. Also, it is worth noting that injection through a metal electrode like a fastener

allows better current distribution. Hence, energy absorption is shared better, and consequently damage is reduced.

Examining Fig. 5–7, shows that the flexural moduli of the different sections of samples, subjected to a lightning impulse of 350 A, it can be seen that they cluster according to the orientation of the top layer. Indeed, those with a 0° top layer have a higher flexural modulus than those whose top layer is oriented at 90°.

As mentioned above, the values measured for the flexural moduli of these samples indicate that the 350 A impulse does not degrade their mechanical strength, with the fastener distributing the electrical energy from the impact in the sample. However, an equivalent mechanical impact of 15 J does affect the mechanical strength of these samples and leads to internal damage to the fibres, which are pushed downwards by the impact. It is important to note that as shown in the previous chapter, increasing the intensity of the impulse up to the kA range leads to pyrolysis. In contrast with the indentation caused by mechanical impacts, pyrolysis causes the plies to move upwards.

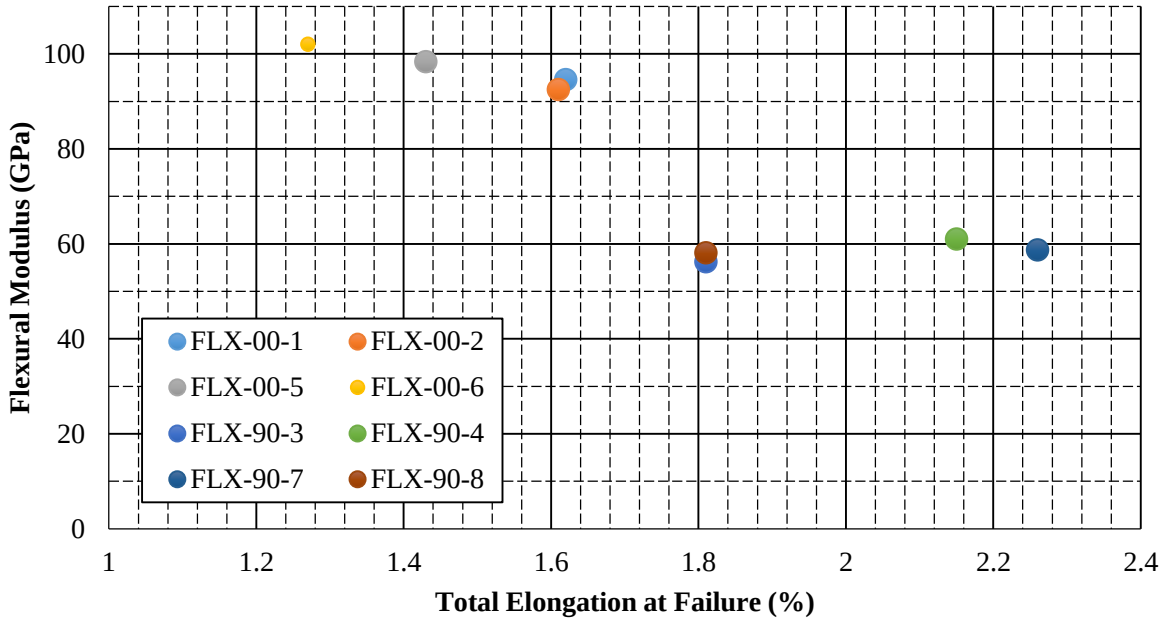

Fig. 5-7. Flexural modulus as a function of the elongation at failure for metal ring electrode samples previously subjected to a 350 A impulse as shown and numbered in Figure 5-5.

With reference to Fig. 5–7, a flexural modulus of 0.1 GPa is measured near the impact point (in sample FLX-05 for instance). The flexural modulus does not vary much across the sample with a 90° top layer (see also Fig. 5–6). The elongation at failure is lowest in the vicinity of the lightning impact point, but there is no difference in the flexural strength of these samples. These results are not in agreement with those found in the literature on lightning strikes and their effect on the mechanical strength of composites. Indeed, this is mainly degraded by mechanical impacts, typically from bird strikes, which are statistically far more frequent than lightning strikes. (Lightning strikes occur on average once per year, whereas bird strikes occur more than once per year). The leading edge of an aircraft wing must, therefore, not only satisfy aerodynamic design requirements, but must also be strong enough to protect the front spar in the event of a bird strike [68]. In this study, the samples had the same ply lay-ups as typically used for civilian aircraft wings.

5.6 Characterisation of CFRP panels under waveform D lightning strike

Two unidirectional M21/T800s 550 by 550 mm samples were characterised using the setup shown in Fig. 5–8(a), with waveform D impulses delivered using the MBLL D-bank (Fig. 5–8(b)).

A current transformer with a sensitivity of 10V/A was used to measure the current using an attenuator probe setting of 1413:1. The sample was clamped at the rig with small G-clamps. For each sample, four strikes were applied with peak magnitudes ranging from 30 kA to 70 kA, and the ply damage was subsequently examined using an optical microscope. Scanning electron microscopy was used to measure the extent of surface delamination. The depth to which fibre-scale damage extended was also measured. The fibre burns and thermal damage are very clear in the images shown in Fig. 5–9.

In [61], un-notched and filled-hole CFRP samples were tested with lightning impulses of different current magnitudes. The damage caused as well as, the tensile strength and compression modulus of the CFRP samples were recorded. It was found that the compression strength of the filled-hole samples is the most affected, decreasing significantly as the strike magnitude was increased from 30 kA to 50 kA. Non-destructive tests showed that, at 10 kA, the damage for the filled-hole samples was confined to the fastener, but more substantial than that suffered by the un-notched samples. Microscopy analysis confirmed that, for the un-notched samples, the damage was confined to the upper two–four plies, while for the filled-hole samples, the damage was either confined to the fastener (at 10 kA) or spread down through the entire thickness of the laminate up to the backface (for higher intensity currents). The authors of [62] also found that the damage caused to the laminate consisted of pyrolised fibres, vaporised resin, and traces of inter- as well as intra-ply arcing. In this thesis, a

microstructural study was performed of the damage penetration of single impulses increasing in intensity from 0–70 kA on a unidirectional panel (see Fig. 5–10).

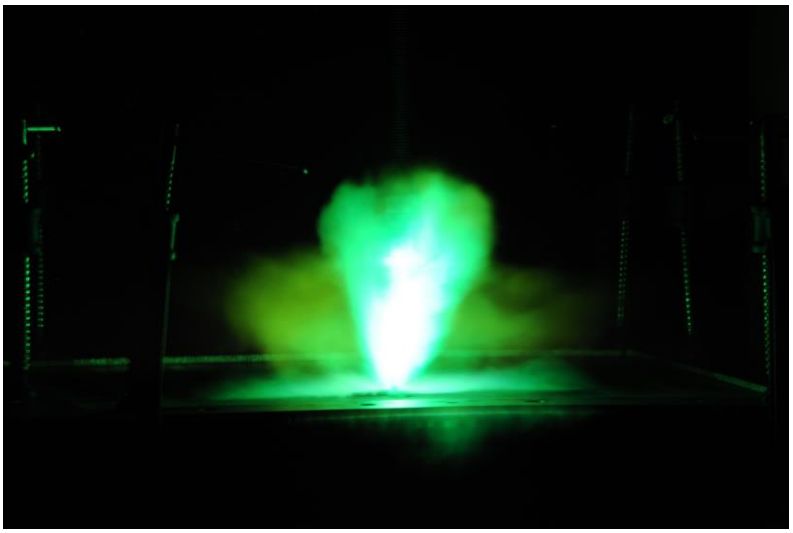

(a)

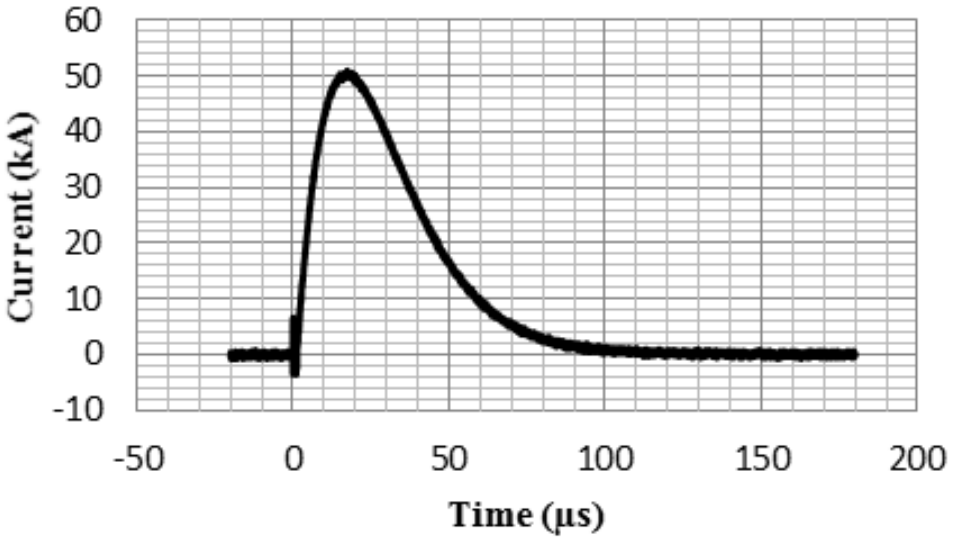

(b)

Fig. 5-8. (a) Photograph of the lightning chamber at the Morgan Botti Lightning Lab (MBLL) during a lightning strike test at 50kA and (b) current vs. time profile for an MBLL Bank D waveform.

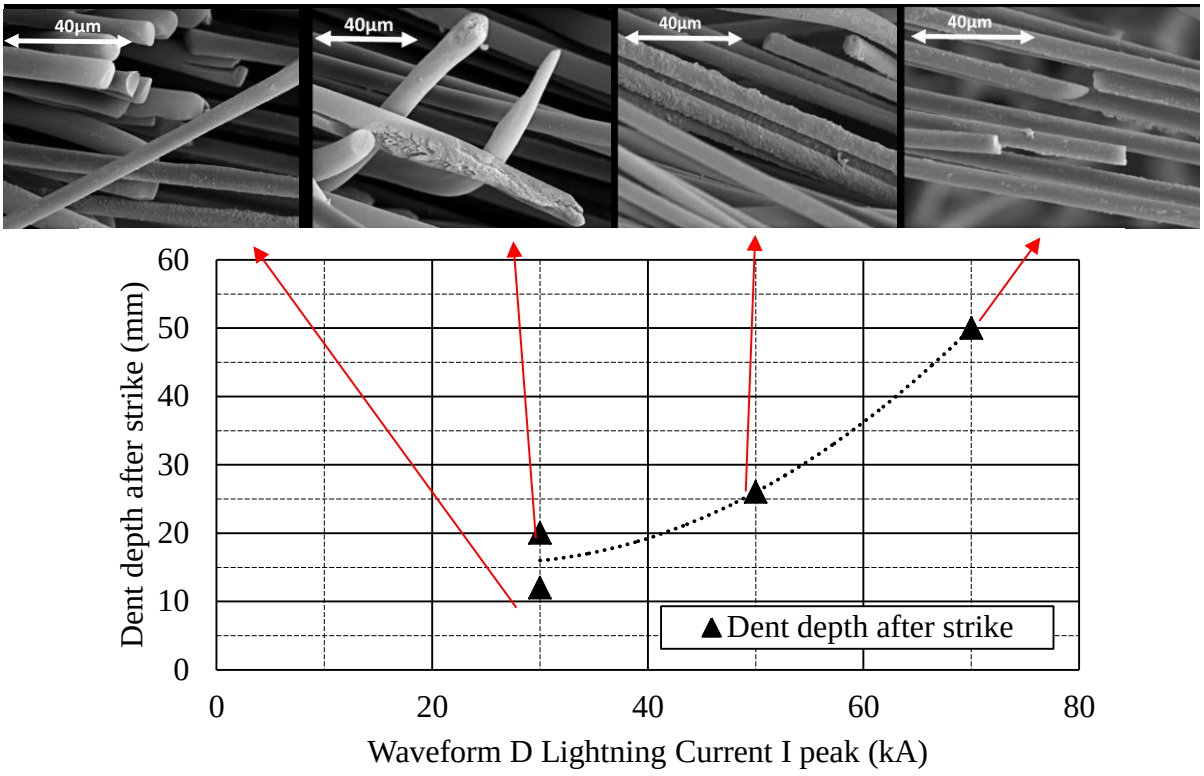

Fig. 5-9. Dent depth as a function of peak current magnitude on a unidirectional M21/T800s panel. The corresponding scanning electron microscopy images are shown above.

The ply damage for the four impulses is shown in Fig. 5–11 while the corresponding surface damage is shown in Fig. 5–12. In terms of delamination, the depth of damage penetration increases with the intensity of the lightning impulse current, as does the total number of damaged plies. At 30 kA, the damage reaches the fourth ply on the first impulse and the fifth ply after the second impulse. In contrast, for 50 kA and 70 kA impulses, Fig. 5–11 shows that the damage penetrates down to plies 6 and 20, respectively. No damage was visible, however, from the back surface of the panel.

It is a normal practice in the research area to correlate the damage depth with the action integral of the waveforms. This was performed here, using a Microsoft Excel template, for the 50 kA impulse. The net electrical charge Q delivered by a typical lightning impulse is given by

$$Q = \int_0^t i dt \tag{5-1}$$

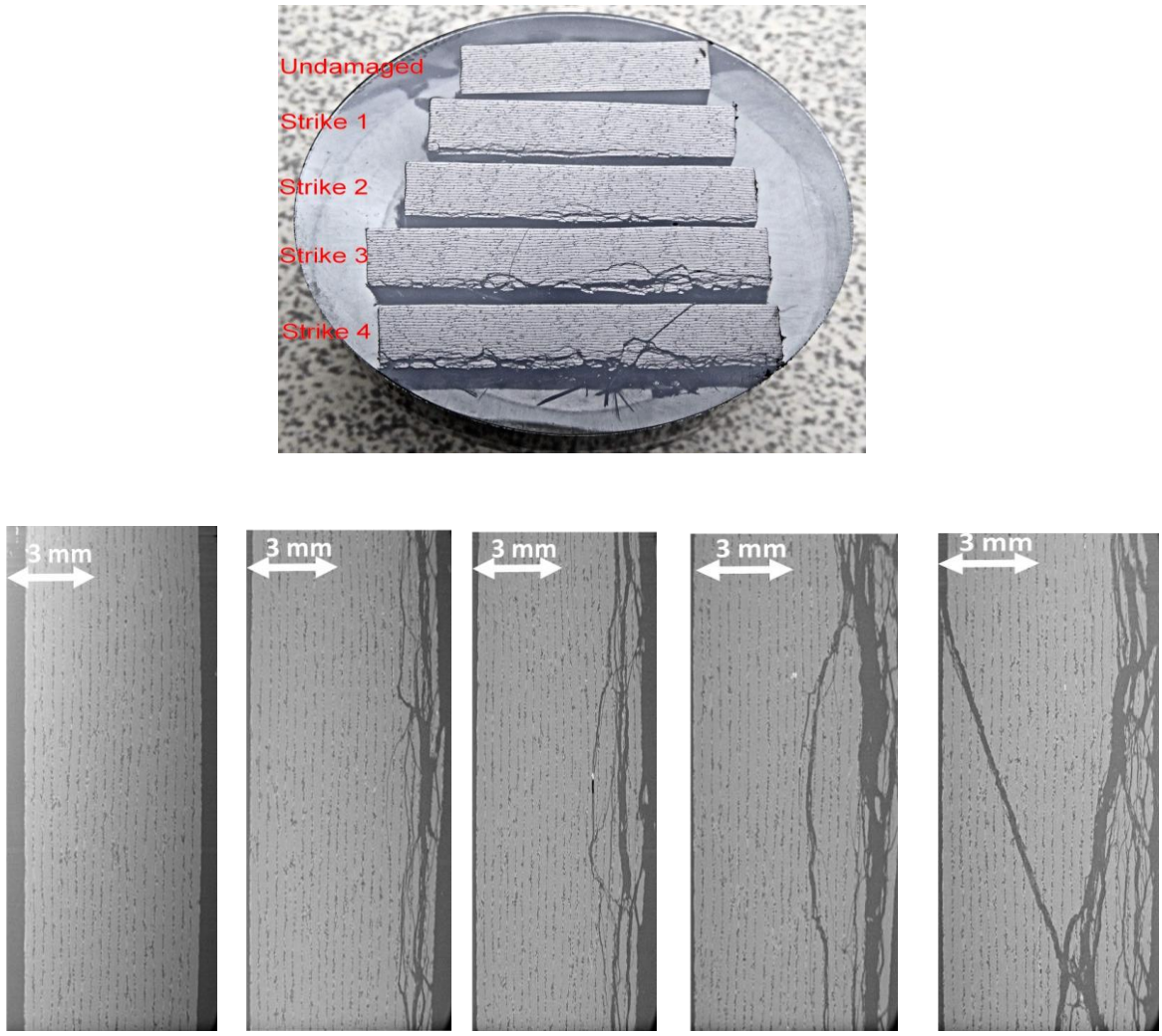

(a) 0 kA (b) impulse 1: first 30 kA (c) impulse 2: second 30 kA (d) impulse 3: 50 kA (e) impulse 4 :70 kA

Fig. 5-10. Photographs (top) and corresponding micrographs (bottom) showing the penetration of lightning damage from the bottom and top surfaces into an unprotected unidirectional carbon fibre composite panel.

The action integral, which is proportional to the total electrical energy, is given by

$$I = \int_0^t i^2 dt \tag{5-2}$$

As shown in Fig. 5–12, the area of surface delamination is 6×10^{-3} m^2 for a 30 kA impulse, increasing to 8×10^{-3} m^2, and 16×10^{-3} m^2 for 50 kA and 70 kA impulses, respectively. The action integrals calculated for the 50 kA and 70 kA waveforms are 0.309 A^2·s and 0.810 A^2·s, respectively, with T1/T2 defined as 5.24/7.96 μs and 7.21/18.1 μs, respectively, for the intensity peak of waveform D—T1 being the front time and T2 the time to half the maximum value. For action integrals of 0.31 A^2s and 0.81 A^2s, the delamination size on surface reaches 0.008 m^2 and nearly 0.016 m^2, respectively. Larger action integrals are indicative of greater surface delamination and greater ply penetration—to the 5^{th} and 20^{th} plies for action integrals of 0.31 A^2s and 0.81 A^2s, respectively.

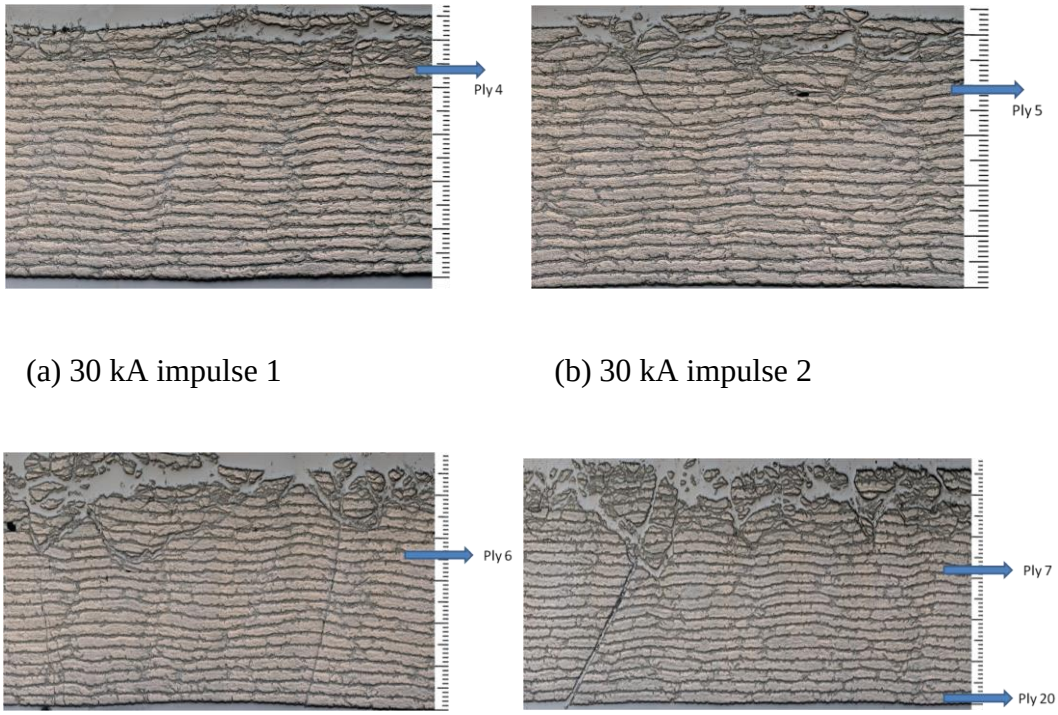

(a) 30 kA impulse 1 (b) 30 kA impulse 2

(c) 50 kA impulse (d) 70 kA impulse

Fig. 5-11. Cross-sectional scanning electron micrographs showing the depth of ply damage in a unidirectional M21/T800s-type sample after waveform D impulses of (a) 30 kA (impulse 1), (b) 30 kA (impulse 2), (c) 50 kA, and (d) 70 kA.

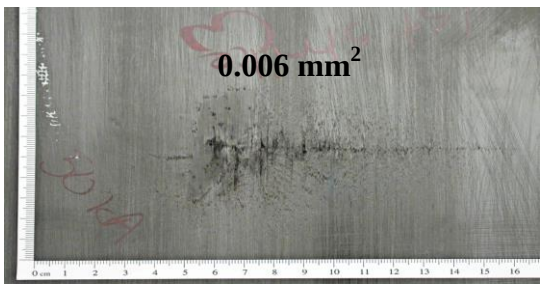

(a) 30 kA Impulse 1

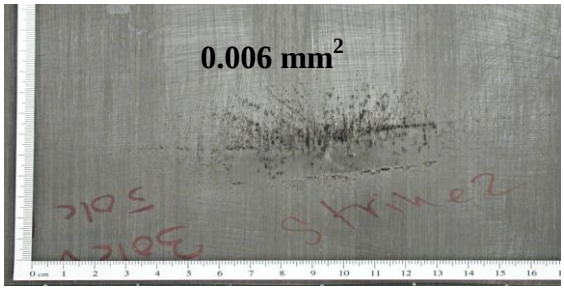

(b) 30 kA Impulse 2

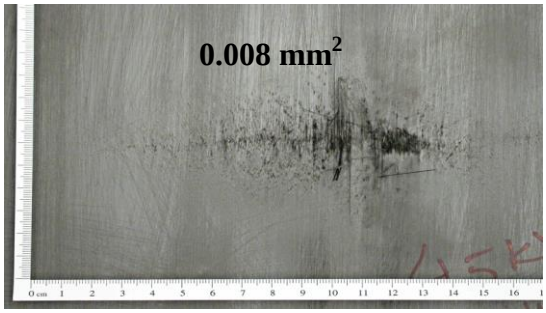

(c) 50 kA Impulse

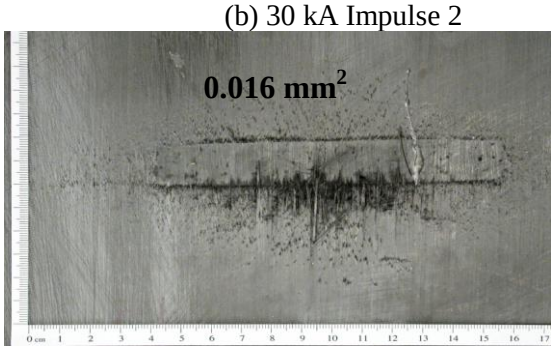

(d) 70kA Impulse

Fig. 5-12 Photographs of the Size of the delaminated area on a unidirectional M21/T800s-type panel with corresponding peak intensity of the waveform D current impulse

Many approaches are possible to assess the degradation of the mechanical strength of aircraft panels following lightning strikes and a number of procedures have been defined to evaluate the mechanical strength following lightning and mechanical impacts. The results obtained in this study for the shear strength of the samples following the application of waveform D impulses are shown in Fig. 5–13.

The damage from lightning strikes can puncture aircraft panels but concentrates mainly on their surface. A noticeable feature of the waveform D tests performed herein is the spread of damage on the sample surface. This is attributed to the sample's lack of lightning protection. The surface spread results from the current taking the path of least resistance, which is along the fibres—therefore, across the surface—instead of crossing the fibres in the through-thickness direction. Furthermore, the absence of lightning protection means that some current penetration occurs in addition to the surface spread.

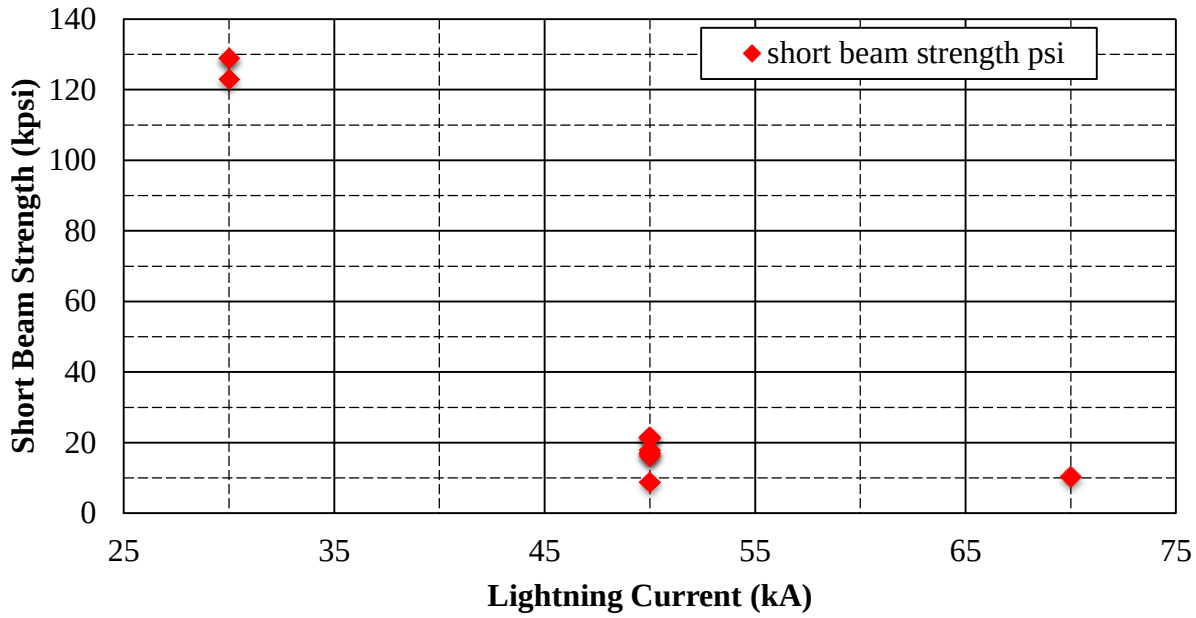

Fig. 5-13. Short beam strength of a unidirectional composite panel following waveform D lightning impulses of increasing magnitude.

The mechanisms of damage propagation are quite complex. Clearly, the fibres act as current carriers while the highly resistive resin matrix impairs current flow in certain directions. However, although the longitudinal resistance in this study was measured to be roughly 40 mΩ, there is no means of comparing the proportions of the total current passing longitudinally and transversely. From the infrared experiments reported in Chapter 4, we know that the distortion resistance is very small for a unidirectional sample with current injected between two surface electrical contacts. However, it is important to note that the progression of current across or into carbon composite panels is ply lay-up dependent.

5.7 Mechanical tests on waveform-D-impacted samples

One of the samples tested under waveform D at the MBLL was submitted to three-point bending tests. The different regions tested are shown in Fig. 5–14. An undamaged region was also tested in comparison, and this sample was then subjected to currents up to 20 kA in three locations. The data obtained from the three-point bending tests are plotted in Fig. 5–15. The

flexural strength of the initially undamaged samples subjected to high magnitude currents is lower than the flexural strength of those submitted to lower magnitude impulses, decreasing from ~1200 MPa to 976 MPa following a 17 kA strike.

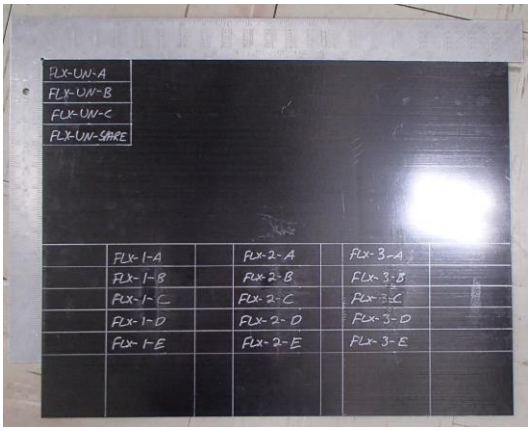

Fig. 5-14. Photograph showing the different mechanical testing regions on a sample previously tested using waveform D impulses.

The flexural strengths of damaged areas indicated in Fig. 5–14 are also plotted in Fig. 5–15. While the flexural strength of the undamaged samples are in the 1200–1250 MPa range, those for the damaged samples are lower, with higher magnitude lightning impulses leading to a greater reduction in strength. The flexural strength of the region submitted to a 17 kA strike is ~970 MPa. Fig. 5–15 also highlights the shift to lower flexural moduli of the initially undamaged samples with the intensity of the impulse current. This verifies the suggestion made above that the mechanical strength of carbon composites is only affected by strikes in the kA range, and not by those of up to 350 A discussed in the previous section.

Current impulses in the kA range can be equated to a mechanical impact in the Joule range, with 0–50 kA equivalent to 0–30 J of mechanical impact energy. These equivalences, which are not specific to composite aircraft, are typically used to evaluate the threat levels associated with both types of impact. The mechanical strength data obtained here can easily be compared with the data presented in Chapter 5 for the degradation in strength of the

composite following mechanical impacts. In the presence of a fastener, mechanical impacts are expected to cause more damage than lightning strikes. Fig. 5–15 shows that the flexural modulus and strength are both lower for testing coupons subjected to higher magnitude lightning currents.

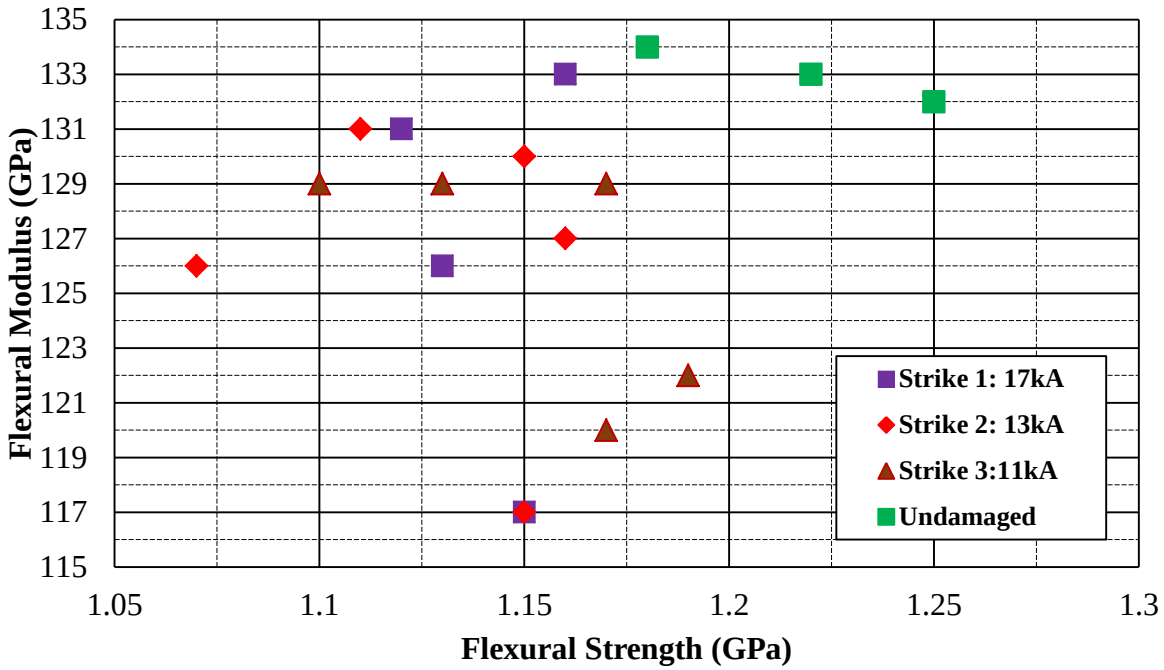

Fig. 5-15. Flexural modulus vs. strength for a unidirectional composite sample previously submitted to waveform D current impulses.

This degradation of the mechanical strength is important to consider with respect, in particular to, the industrial requirements and design loads for real aircraft. Indeed, these results show that electrical characterization studies for carbon fibre composites are necessary but not sufficient because of the associated degradation in mechanical strength. The preliminary evaluation conducted in this thesis suggests that the ply angle has no effect on the electric potential distribution. The main factors considered in the design of carbon composites are mechanical rather than electrical. The findings presented herein of the mechanical effects of high magnitude impulses go beyond a simple investigation of the thermal damage inflicted on the carbon fibres of the composites. The samples with fasteners tested for currents of up to

350 A were found to have their flexural strength unaffected. Samples without fasteners were not tested in this (mA–kA) current range. In summary, therefore, whereas ampere-range lightning impacts had no measurable effect on the mechanical strength of these samples, kiloampere-range strikes lead to about 10% decrease in their flexural strength (21% for a 20 kA current).

5.8 Microscopic damage analysis

Microscopy was used to study the damage in all samples tested under high currents. For the 8-ply sample, cracking was visible beneath the metal fastener (see Fig. 5–16). The remaining samples were tested without the metal ring and in particular directions. As described previously, the electrode rivets were labelled 1–8. The middle fastener was used for current injection while the outer rivets (1–8) were grounded. For impulse currents of 50–350 A, Fig. 5–16 shows that the damage did not penetrate down to the lower layers but this was not the case for the waveform D currents exceeding 1 kA. For the samples destined for zone 2A subjected to waveform D impulses, the fastener region was studied. The damage was found to be concentrated in the vicinity of the fastener, in the form of delamination cracks in the fibre layers rather than in the resin. The cracks were not continuous and did not reach the centre (in the thickness direction) of the panels.

Since the precise lay-up of the panel was unknown, the different layers may have been perpendicular to each other; current injection was, therefore, assumed to be transverse. For other samples, there was no visible damage to the fasteners except in regions where ECF had been removed from the surface. In the sample from zone 1C, the ECF layer was burnt in the damaged region and removed from other regions on the surface of the carbon fibre composite. Splintering was also observed in the images obtained for these regions,

highlighting the de-bonding of the copper mesh used for lightning protection from the surface of the carbon fibre composite, allowing current penetration into the panel.

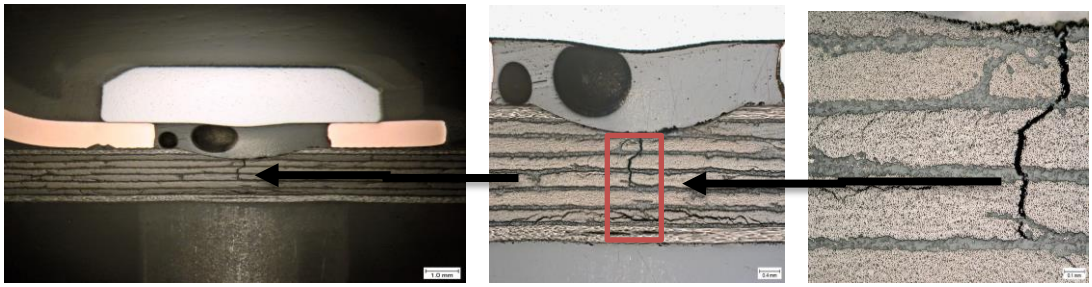

Fig. 5-16. Cross-sectional optical micrographs showing cracking and damage in a M21/T700s-type samples following repeated 50–350 A impulse current injections.

It is noteworthy that this microscopy analysis revealed manufacturing defects in the form of voids, which were found to run down through the panel (see Fig. 5–16). One such gap was observed for the panel from zone 2A, which was found to be devoid of cracks.

Fig.5–16 shows that the damage propagates downwards beneath the fastener region in the quasi-isotropic sample. The cracks then spread horizontally in the middle region of the sample, in some cases, reaching the lateral extremities of the sample. This current path (viz. flow into the panel for a quasi-isotropic lay-up) is attributed to the symmetrical lay-up of the panel; the results are different for a two-layered panel, as shown in Figs. 5–17 and 5–18. These samples did not have a metal ring electrode. Instead, the different rivets on the outside allowed directional current injection.

Fig. 5–18 shows cross-sectional optical micrographs—taken after application of lightning impulses—of the samples depicted in Fig. 5–18. The current path into the panel is visible in Fig. 5–18(a) as well as the resulting cracks. As shown in Chapter 3, the resistive distribution of equipotentials means that the potential is the sample in the two layers of bilayer carbon

composites. This explains why cracking is observed here in layers, while the fastener is heavily burned.

(a)0/90 M21/T800S sample (b) 20-ply quasi-isotropic lay-up (c) ECF T-joint sample with primer for a quasi-isotropic lay-up

Fig. 5-17. Photographs of the different samples studied under high-intensity impulse currents, the directions of current injection are indicated by dotted green lines.

The damage in Fig. 5–18 for the T-joint sample with primer and ECF is similar to that shown in Fig. 5–16 for the M21/T700s-type sample, originating from the fastener tip and spreading down to the lower layer with diminished intensity. For the 20-ply sample, on the other hand, no damage is observed along the path of current flow between the fastener and the rivet (Fig. 5–18 (d)).

Ogasawara et al. [61] have studied thermal damage in carbon fibre composites. The authors found that the electrical conduction in the through-thickness direction of CFRPs was an important parameter to consider to model the thermal decomposition of the panels accurately. The electrical conductivity in the through-thickness direction was assumed to vary linearly with temperature for temperatures ranging from the epoxy decomposition temperature to the sublimation temperature of the carbon fibres. Simulations were used to estimate the delamination area and penetration depth of the damage, with the results obtained agreeing

qualitatively with experiments. The authors of [61] concluded that Joule heating is a significant vector of lightning strike damage.

(a) near the fastener

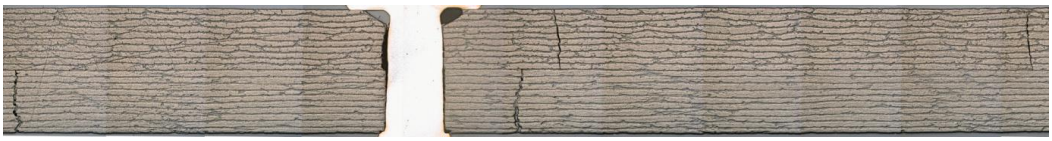

(b) near rivet 2,

(c) a quasi-isotropic T-joint sample containing ECF

(d) an MTM28-1/T800H-type sample.

Fig. 5-18. Cross-sectional optical micrographs showing the damage following high-magnitude current impulses

5.9 Simulations of multi-layered carbon fibre composites

5.9.1 Simulations without aluminium fasteners

A simulation was performed in COMSOL for a multi-layered carbon fibre composite panel with epoxy layers. The composite panel consisted of seven layers, with five alternating carbon fibre layers sandwiched between top and bottom epoxy layers. The composite was simulated in air (above the topmost epoxy layer). This configuration is depicted in Fig. 5–19, and the electrical properties of the different simulated layers are listed in Table 5-4.

Table 5-4: Electrical properties of each layer in the modelled composite panel.

Layer	**Conductivity σ (S/m)**	**Relative Permittivity ε_r**
Carbon Fibre	70×10^3	1
Epoxy Resin	0	3
Air	0	1

Figs. 5–20 and 5–21 illustrate the different boundary conditions applied; the top and bottom edges of the model were grounded, the sides were electrically insulated and continuous boundary conditions were applied between the layers. The lightning impulse voltage was applied at the centre of the topmost epoxy layer of the panel.

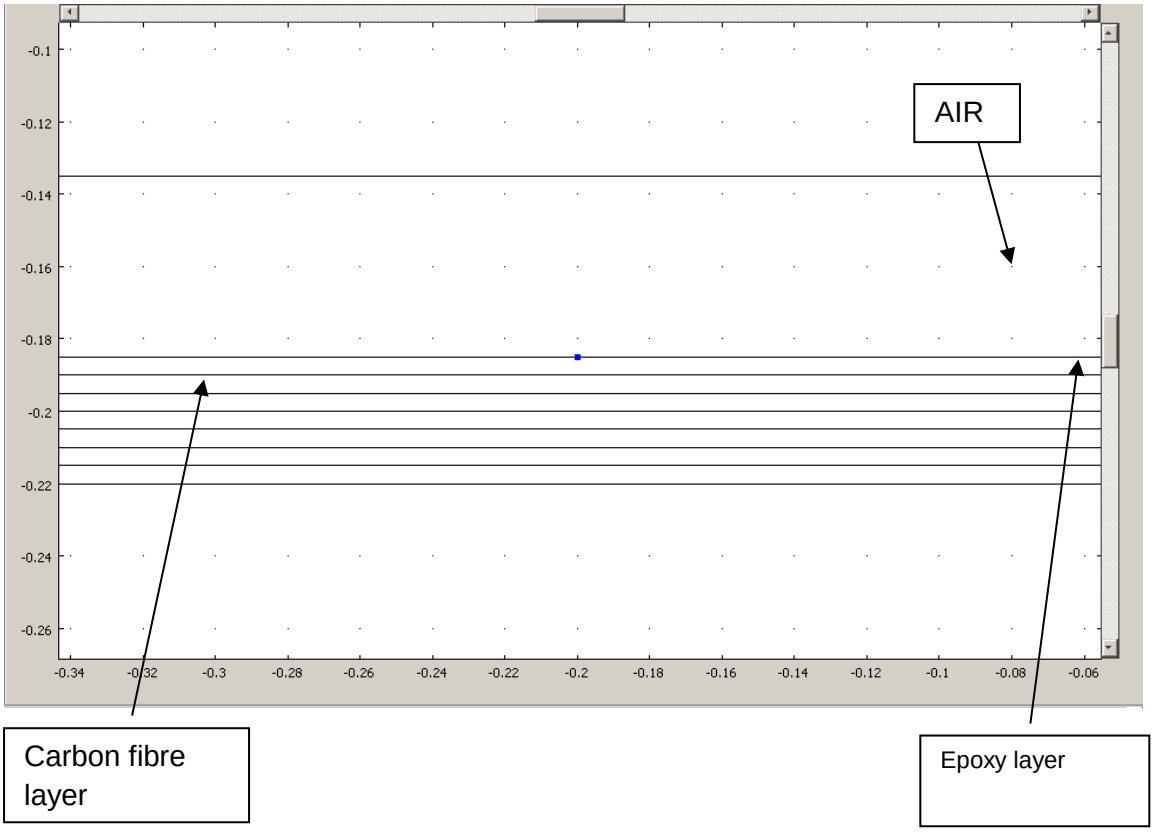

Fig. 5-19. Schematic of a seven-layer carbon fibre composite panel as simulated in COMSOL.

The applied lightning impulse voltage is characterized by the following expression:

$$V(t) = 114285.7\left(e^{-\alpha t} - e^{-\beta t}\right), \tag{5-3}$$

where $\alpha = \frac{1}{68.2\times10^{-6}}$ and $\beta = \frac{1}{0.405\times10^{-6}}$ (5-4)

As already stated, the carbon fibres and epoxy resin constitute conducting and insulating media, respectively. To achieve a sufficient level of accuracy in the region of interest, the simulations were performed with finer meshing in the vicinity of the lightning strike than elsewhere. Note that the additional memory cost incurred by applying this finer mesh to the entire system would have prevented the simulations converging. Electrical contour plots such as the one shown in Fig. 5–20 were obtained from these simulations. Fig. 5–20 highlights the concentration of equipotential lines in the air layer and the top epoxy layer.

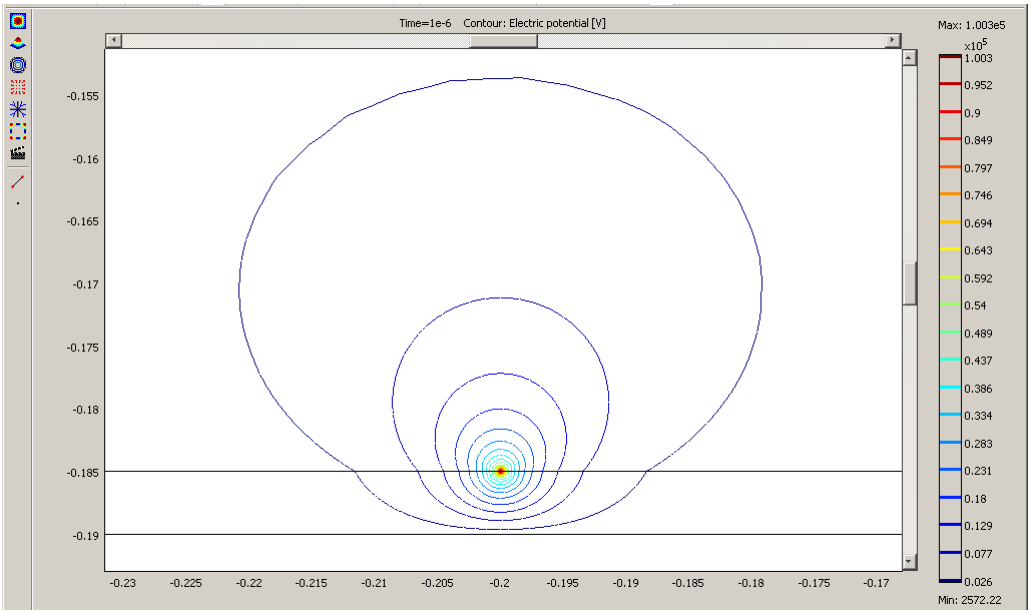

Fig. 5-20. Electrical potential obtained from a COMSOL simulation of the two-layered carbon fibre composite panel. The first two layers of the panel are shown, as well as the air layer on top.

For the aforementioned model, the electrical potential reached a maximum of 100.3 kV at 1 µs in the region where the lightning voltage was applied. An expanded view of the simulated lightning impact zone is shown in Fig. 5–21, where the contour lines cluster.

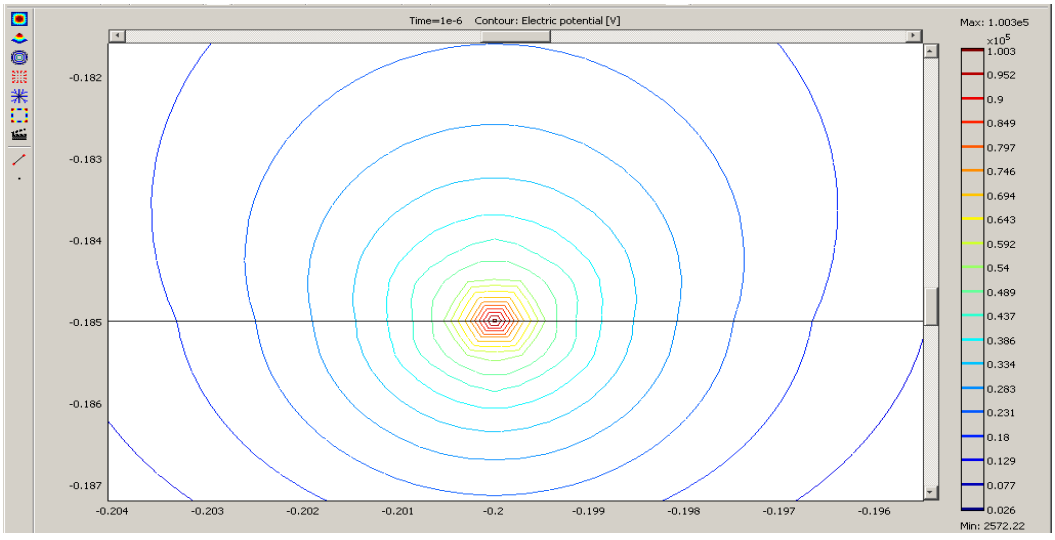

Fig. 5-21. Electrical potential contour lines clustering in the vicinity of the simulated lightning strike.

5.9.2 Simulations with an aluminium fastener

The goal of this simulation was to understand the effects of incorporating a conducting material (aluminium metal in this case) between the composite layers. This is typical of the modifications applied for various applications in which increased conductivity is required. Current simulations can be performed using the same model to determine the preferred paths through the composite and identify the regions susceptible to lightning damage.

A simulation was then performed following the same concepts applied for the composite panel discussed in Section 4.5.1, but now with an aluminium fastener added between the composite layers (with each layer being 5 mm thick and 2 m long; see Fig. 5–22). The lightning impulse voltage was applied on all edges of the aluminium fastener. The remaining boundary conditions were the same as those presented in Section 4.5.1, and as before, a tighter meshing was defined in the vicinity of the aluminium fastener. There were two layers of air in this model, one above and one beneath the simulated panel.

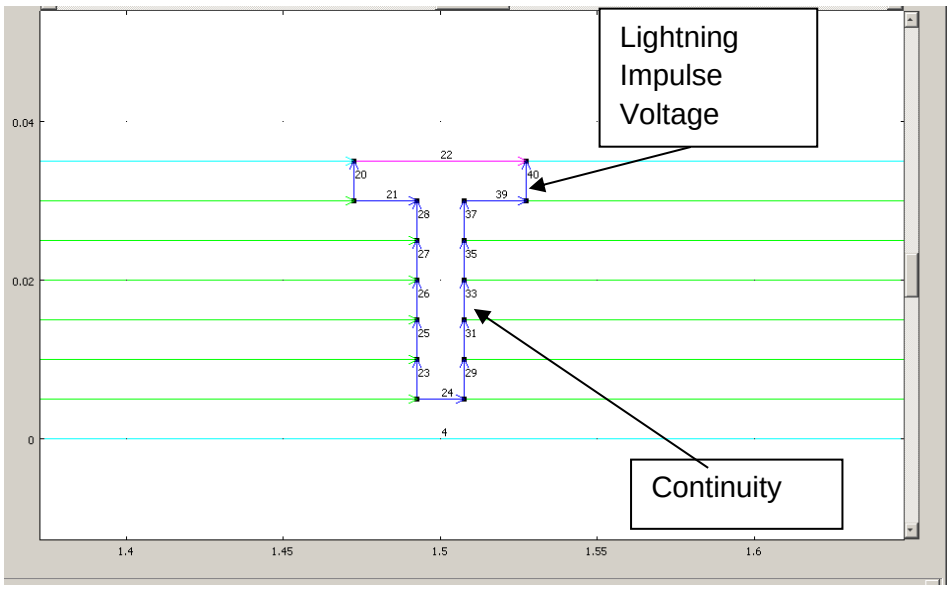

Fig. 5-22. Schematic of the boundary conditions used for the COMSOL simulations of the carbon fibre composite panel with an aluminium fastener.

As defined in COMSOL, the aluminium fastener had an electrical conductivity of 3.47×10^7 S/m and a relative permittivity of 1.

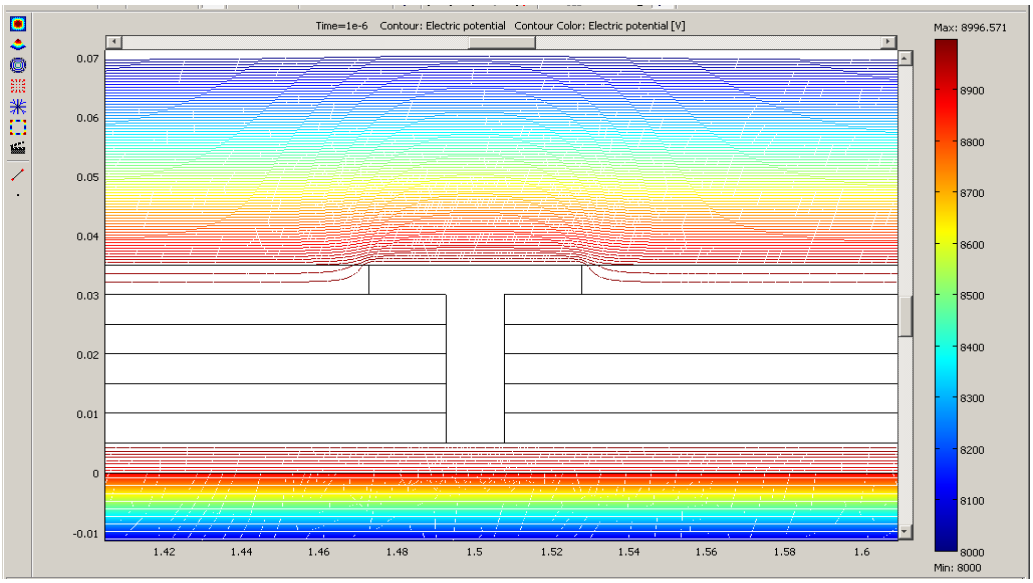

Fig. 5-23. Electric field lines for a multi-layered composite panel with a T-shaped aluminium fastener under a simulated lightning voltage.

The electric potential contours obtained for this simulation are shown in Fig. 5–23. The highest voltages are found above the topmost epoxy layer and near the aluminium fastener. The carbon fibre layers in the composite panel shield the inner epoxy layer in which no equipotential lines are observed. The maximum voltage—obtained at 1 μs—for this simulation was 9 kV.

5.9.3 Current distribution in CFRP panels in the presence of fasteners

A current simulation was performed for the same multi-layered carbon fibre composite panel with an aluminium fastener described above (Fig. 5–22). A lightning current source was used

and the current density in the fastener was obtained by dividing the intensity by the total area of the fastener (6.5×10^{-4} m^2). The current source was defined as follows:

$$I(t) = I_0 \left(e^{-\alpha t} - e^{-\beta t}\right) \tag{5-5}$$

where I_0 and the rise time, *t*, were set to 218 kA, and 50 μs, respectively, and

$$\alpha = 11354\ s^{-1} \tag{5-6}$$

and

$$\beta = 647265\ s^{-1}. \tag{5-7}$$

This gave a current density of 1.9×10^8 A/m^2, which was applied to all edges of the aluminium fastener. The boundary conditions were modified, with the air above and below the panel set to be insulating and the lateral extremities of the model, previously insulating, now grounded.

Fig. 5–24 shows that the current is maximum at the interface where the aluminium fastener meets the composite structure. Indeed, the red regions are concentrated where the head of the aluminium fastener contacts the carbon fibre layer. All of the carbon fibre layers are of the same colour, indicating that the current density therein is the same.

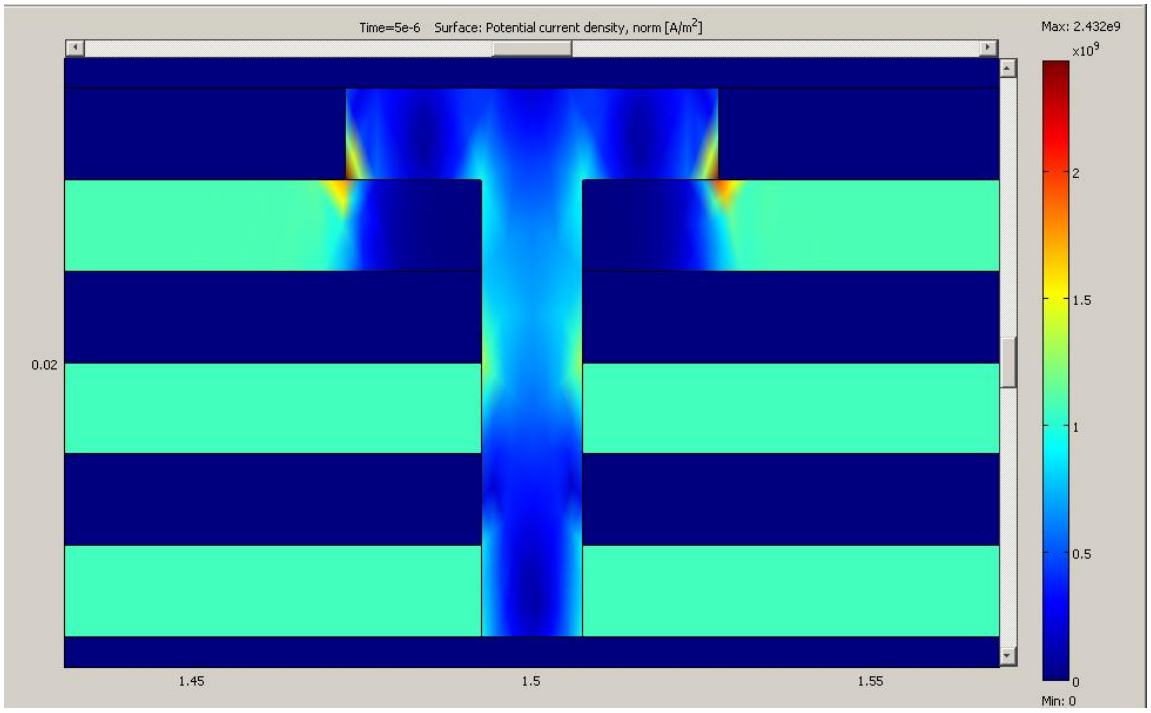

Fig. 5-24. Current density on the surface of the multi-layered carbon fibre composite panel with a T-shaped aluminium fastener.

The current density reached 2.4 × 10^9 A/m^2 at 5 µs. Current penetrating through the critical regions where the metal is in direct contact with the carbon fibre material is likely to be damaging. Lightning protection measures for CFRP structures and aircraft parts are discussed in the following section.

The simulation in Section 6.3.2 was performed with no air gap between the metal fastener and carbon fibre composite. Although the results obtained showed that the carbon fibres provided effective shielding, this may not be representative of the situation in practice, where air gaps between the fastener and the composite reduce the shielding effectiveness of the latter. Carbon fibre layers by themselves may, therefore, prove adequate under a real lightning strike.

The main subject of discussion in this context is the conductivity of carbon fibre composites. Indeed, although carbon fibre composites are good conductors, they offer a greater resistance

to current flow than metals. Adding a more conductive material (e.g. a metal) should boost the shielding capacity of carbon fibre composites. In the current simulations, performed for a multi-layered carbon fibre composite panel with an aluminium fastener (Section 6.3.3), the current density was highest at the metal–carbon-fibre interface, which constitutes the path of least resistance for current flow and dissipation out of the fastener. Furthermore, the equipotential lines in the bottom and top epoxy layers of the model (see Fig. 5–20) show that lightning strikes can lead to the dielectric breakdown and decomposition of the polymer matrix layers.

The composite can lose its structural integrity because of 'thermal decomposition', that is, resin vaporisation and the associated release of gases. Again, this effect is illustrated in the above simulations via the presence of electric field lines in the epoxy layers that were not shielded by the carbon fibre layers. Since the other desirable properties of carbon fibre composites make their use in the aerospace industry inevitable, a detailed study and optimisation of CFRP lightning protection is required to avoid or minimise the damage incurred. Even using cutting-edge engineering techniques however, this remains a significant challenge.

5.10 Thermal damage due to prolonged direct current application

A direct current (10 A) was injected for an extended period of time into T-joint samples using a modified experimental setup; the central fastener was used as the current injection electrode while rivets 1–8 were used in turn as current return electrodes. Fig. 5–25 highlights the substantial burning at rivets 3, 4, and 5; the red lines in this figure indicate the current injection paths, with the voltage measured from the same locations. The damage was the most severe at rivet 5 (Fig. 5–26). At rivet 5, the magnitude of the injected current was reduced for a period of time due to signs of burning being detected (i.e. for safety reasons).

These tests were also performed on other samples (see Table 5-1). In these T-joint samples, current is mostly carried by the ECF layer. However, the presence above the ECF of a primer and a composite layer, and the 45° orientation of the bottom ECF layer, impairs current flow through the sample. As a result, the current has to cross the high resistivity matrix leading to rapid burning.

Fig. 5–26 shows the fibre burning at rivet 5 that resulted from the direct current (10 A) applied during these tests. Interestingly, although rivet 1 is located along the same high-impedance path, no burning occurred there (see Fig. 5–25). This difference may be due to a poor connection between rivet 1 and the carbon composite.

Table 5-1: Details of the samples tested under direct current and of the tests performed.

Sample Ply Lay-Up	DC Current Injection Level (A)	ECF	Configuration
(45,135,0,0,90,0,135,0,0,135,0,90,0,0,135,45)	10 A	Yes	Rivets/fastener
45,135,0,0,90,0,135,0	10 A	No	Metal ring electrode /fastener
((0,90)4)s	10 A	No	Rivets/fastener

Fig. 5-25. Photograph of a T-joint sample containing ECF and primer as used for direct current damage tests.

The thermal damage shown in this section is due to the injection of 10 A direct current, using the central fastener as the positive terminal and one each of the rivets in turn as the return current terminal. Joule heating damage is one of the most common effects of lightning strikes in carbon fibre composites. Ogasawara et al. [69], for instance, conclude that the damage detected following their impulse tests arose via Joule heating. The authors in [69] use Joule's law to describe the electrical power, *Pec***,** dissipated via current flow into the conductor using the following equation

$$P_{ec} = J.E = (E.\sigma).E = \sigma E^2 = \frac{J^2}{\sigma} \tag{5-8}$$

The fibre burns shown in Fig. 5–27 demonstrate that direct current alone can cause individual fibres to crack. Interestingly, however, the resin remains undamaged, only the fibres are affected. This explains the results from Chapter 5 that fibre breaks are evidenced by changes in DC resistance, whereas low-magnitude impulse currents—which cause delamination in addition to fibre breakage—can be used to reveal mechanical impact damage via non-linearity in measured voltage profiles.

The continuous injection of current at 10 A caused Joule heating in the carbon composites. The thermal damage that is the result of this Joule heating is shown in Figs. 5–26 and 5–28. These micrographs were obtained from areas between the fastener and rivet 5 and reveal substantial resin vaporisation in some regions and the presence of voids in others. The damage to the resin is more extensive to the fibres.

Fig. 5-26. Thermal damage (fibre breakage) at rivet 5 of the T-joint sample due to prolonged direct current injection.

The DC resistances measured from the central fastener to rivets 8 and 1 are 0.147 Ω and 0.057 Ω, respectively. In other words, the resistance to rivet 8 is 2.6 times greater than along the adjacent path to rivet 1. This highlights the effect of the ply orientation of the sample, the 45° degree orientation of the top layer and the angular spacing of 22.5° between the samples meaning that the path to rivet 8 is primarily transverse. For the same reason, the resistance measured at rivet 6 (0.115 Ω) is 3.2 times that measured at rivet 5 (0.37 Ω). Similar DC resistances were measured at rivets 2 and 7 (respectively 0.067 Ω and 0.071 Ω). Pyrolysis is a complex phenomenon in carbon fibre composites but mainly occurs when the resin decomposes due to Joule heating [69]. Pyrolysis was observed here at rivets 3, 4, and 5. The test was repeated for another sample where all rivets were burned. For the latter sample, the resistances at rivets 1 and 2 were found to be 0.057 Ω and 0.067 Ω, respectively. This ratio of 1.2 between the resistances measured at neighbouring rivets is low compared to a ratio of 2 measured for rivets 3 (0.24 Ω) and 4 (0.112 Ω). These values were obtained after 500 s of current injection. However, when burning was observed before 500 s, the injection was interrupted to perform resistance measurements.

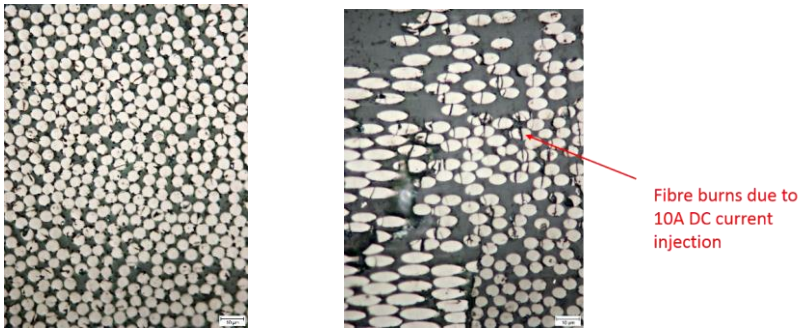

Fig. 5-27. Cross-sectional electron micrographs showing fibre burns induced by 10 A direct current in the vicinity of the fastener.

The resistive behavior for this type of configuration is quite complex. Indeed, for rivet pairs 1-2 and 2-3, the two rivets adjacent to each other and, therefore, separated by an angle of 22.5°. However, while for the former the ratio of DC resistances is only 1.2, it is 3.6 for the latter. The absence of a clear trend is confirmed for the other rivet pairs. The resistance at rivet 4 is a factor of two lower than at rivet 3. The DC resistance at rivet 5 is three times higher than at rivet 4 but three times lower than that measured at rivet 6, which in turn is 1.6 times higher than that measured at rivet 7. Finally, the DC resistance from the central fastener to rivet 8 is 2.6 times higher than that to rivet 7.

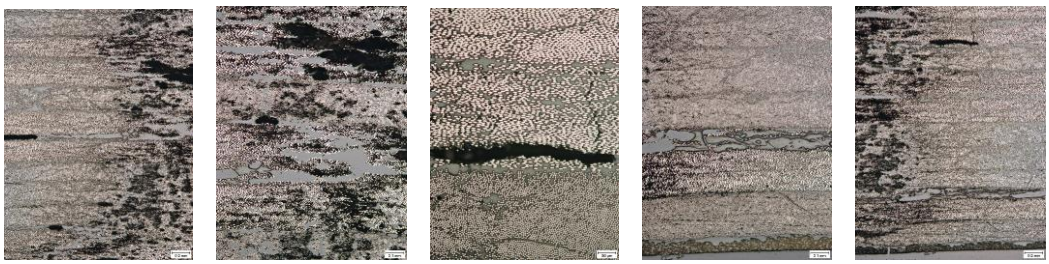

Fig. 5-28. Micrographs showing the thermal damage at rivet 5 on a T-joint composite sample due to prolonged injection of 10 A direct current.

High-current tests of the frequency dependence of the AC impedance of these samples were not performed for this thesis. These would nonetheless be interesting, as the frequency dependence of the impedance would indicate the alteration of current paths in the sample due to emerging damage. Disruptions to the electrical circuit in the carbon composites would be revealed by non-linear variations as a function of frequency of the voltage profiles.

5.11 Conclusions

In this chapter, high magnitude current tests were conducted in the MBLL on various CFRP samples. Lightning impulse tests were conducted using waveform D impulses. The size of the de-laminated area in the samples was found to increase with the intensity of the lightning current. The dent depth and ply damage were also studied for lightning currents of up to 70

kA. At this current magnitude, the damage penetrated down to the 20^{th} ply of a unidirectional panel, whereas the damage only reached the 6^{th} ply for a current of 30 kA. The damage to the fibres was imaged using advanced microscopy, which clearly showed fibre breakage and burns following waveform D impulses of 30–70 kA.

Three-point bending tests performed on composite panels previously subjected to 17 kA waveform D currents at the MBLL highlighted the degradation of tensile strength caused by lightning strikes. For the sample tested with lightning impulses up to 350 A, the middle region was studied by microscopy and was, therefore, not subjected to three-point bending tests. However, a flexural map showed no significant decrease in the mechanical strength of areas in the vicinity of the lightning impulse injection fastener site.

Simulations were performed using COMSOL for Carbon fibre geometry with a fastener; these results showed that the damage to carbon composites with fasteners could be of great significance.

Continuous Direct Current injection into a carbon composite sample showed that Joule Heating can cause significant damage to metal fasteners and can cause cracking of individual fibres, thereby, causing smoking and degradation of material. At this point, a mechanical strength test to study the effect of dc injection on mechanical strength was not attempted in this work.

Chapter 6

CONCLUSIONS AND FUTURE WORK

6.1 CONCLUSIONS

Extensive testing of carbon composite samples has identified the resistive network within the samples. Special techniques were used to prepare composite samples with up to 25 surface electrodes to ensure that their entire surface was characterised. These comprised the photo etching technique in which copper was deposited on a carbon composite sample and electrodes were then formed using lipowitz's alloy. Electrodes on remaining samples were formed using a different technique of silver paint and a thin wire. Attaching electrodes to the surface of samples introduces two additional sources of uncertainty for subsequent resistance measurements. These are the contact resistance of the electrode and the distortion resistance, which result from the current spread away from the electrode. These distortions were not examined in this work but were avoided using careful experimental design. A material resistance parameter was defined for the test electrodes. There is no established technique to characterize material resistance using surface electrodes in carbon fibre composites. Therefore, the technique used here for surface characterization is useful in establishing a surface resistance technique to obtain material resistance for such carbon composites and being applicable to carbon composites of all ply lay-ups.

Furthermore, bulk conductivity properties were determined – with respect to the orientation of the carbon fibres – in the longitudinal, transverse and through-thickness directions. Tests were performed under both low-intensity direct and impulse currents, with good agreement between the two resulting datasets. The electrical properties of the carbon fibre composites were also characterised via a careful analysis of the microstructure of different samples. The

effects of low and non-destructive high lightning-magnitude strikes ranges were visualised in a clear manner. Surface characterization and volume characterization was done separately for the carbon fibre composites, and the volume characterization was performed for different ply lay ups. It was found, generally, that the electrical conductivity of carbon fibre composites varies in the three principal directions. The conductivity in the x-direction, σx , was found to be of the order of 10^3 S/m whereas in the y direction it was of the order of magnitude 100 S/m, and in the z–direction, it was the lowest, of the order of 10 S/m. These values corresponded quite well with work published in the literature by other researchers; however, minor discrimination is seen due to the difference in the material and dimensions used by other researchers in literature. It is noteworthy here that the values reported in literature are specific to a specific ply lay-up. However, work performed in this thesis covers a wide range of ply lay ups and values have been found through intensive testing.

A good electrical contact is critical to characterise the electrical properties of composite samples accurately and is also challenging. This was achieved here on the basis of an extensive analysis of the different techniques described in the literature whereas initially experimentation was done using different techniques like the photo etching method comprising electro-plating of the sample and then performing masking and etching of the sample. However, due to application of the electro plating, the electrodes came off from some areas. This process of attachment of electrodes showed that electroplating is not a good technique to deposit metal on a carbon composite sample and it is also not reliable. Adhesion of copper, therefore, to a carbon composite was not found to be good enough for electrode formation. This survey indicated that the optimal approach was to cover the entire length of the electrode with silver-painted conductive adhesive and to fix thereupon a thin and highly flexible wire. This setup maximises the contact area between the paint and the wire. After curing, the electrode was fixed to the silver paint. Thereafter, all measurements taken were

using the same electrode connection type. It was found that the resistance of samples under all energizations including alternating current, direct current and lightning impulse were very close in value. Therefore, the electrical network inside the carbon composite is completely resistive.

Numerical simulations performed, verified the findings that behaviour of carbon composites under lightning impulse and direct current was resistive, as existence of shared equi-potentials was found. The shared equipotentials were also verified using an infra-red camera by injecting a direct current and not an impulse, the electrodes were formed using silver paint and highly thin flexible wire with the current injection direction being in the through thickness. The infra-red experiment evidenced that the shared equipotentials do exist in the real experimental world in carbon fibre composites. When a ply lay-up of 0/90 was tested under a current magnitude of 350 A, the pattern of damage was alternating which indicates that the shared equipotentials must exist in reality even at high current.

High current characterization was performed to evaluate damage mechanisms in carbon fibre composites. Two ranges of current were used one in intermediate current Amperes and the other one in kilo Amperes. The intermediate amperes range did not seem to have any effect on mechanical strength of carbon fibre composites. Note that mechanical strength is important in aircraft structures as the mechanical design dominates the electrical design in general aircraft construction. For samples enduring mid-range of current in amperes, the metal ring was used as the return electrode and a current fastener is used for the current injection. For higher currents in the kilo-amperes range, the testing was performed at Morgan Botti Lightning Lab. Dent depth and surface delamination was measured using microscopy. The samples were also tested for mechanical strength parameters. Extensive lightning strike testing was not performed for this thesis. Only two samples unprotected were struck under

lightning from 17 kA to 70 kA. The damage in these samples was compared on a micro scale with that caused by currents ranging in intensity from 50 A to 350 A. Such a comparison is not available anywhere else in the literature, and it was unknown before how much a mechanical strength will degrade after such levels of current are injected into carbon composite samples.

In the kA range, the mechanical strength reduced with increasing current level, from 11 kA to 17 kA, the reduction in mechanical strength denotes that lightning current in the kiloampere range will adversely affect the mechanical design of an aircraft composed of carbon composites. However, for an equivalent range of J in the mechanical impact experiment, the mechanical strength degradation will be more compared to an equivalent lightning impulse event.

For DC thermal tests, the microstructure revealed that continuous injection of DC current as high as 10 A, eats away the carbon fibres so that splits are seen inside the individual carbon fibres. A close image indicated that, if the split inside the carbon fibre was mainly across the diameter, this split then will affect the electrical network. However, each fibre is still in contact with another unbroken fibre, and thus, the electrical network is renewed. This is the concept of electrical ineffective length in carbon fibre composites.

Microscopy in this thesis was used for measuring the dent depth and surface delamination of samples impacted under mid-range of lightning impulse. It was found that the damage because of lightning impulse occurs as a blast with the fibre layers moving upwards. The microstructure analysis of low current samples enduring 350 A showed that for 0/90 oriented sample the damage propagated in a twisted pattern with cracks developing in alternating layers, this represents and is linked to the shared equipotential found in Chapter 3 in simulations which shows that the equipotential is shared in the two layers, similarly the

cracking observed in the 0/90 degree layup is not continuous, it is shared in the two layers. For remaining samples especially the quasi isotropic sample, the damage diminished at the end of the bottom layer. The sample tested under 350 A was tested under repetitive impulse testing in Cardiff High Voltage Lab. A quasi isotropic sample showed that the damage diminished at the end of the fastener.

For lightning strike tests under waveform D, the samples tested showed burned fibres, and broken fibres, with splits and damage. For continuous DC current injection, there microscopy was also performed, the fibres were observed to have cracks along their diameter length, this represents an attack of direct current on fibres due to joule heating. An alternate test of continuous injection of AC current is not performed in this work. However, direct current is also equally damaging compared to a lightning strike magnitude of 70 kA as studied in this work, if it is passed continuously for 500 seconds or more.

The experiments conducted in this thesis are for smaller panels up to 550 mm however in the larger panels on aircrafts especially the non-flat panels the effects may be different.

6.2 FUTURE WORK

Future work in this field should concentrate on the development of more cost-effective methods for damage assessment in composite panels. The literature study in this thesis of the effects of loading on the electrical resistance of carbon fibre composite highlights the potential of this approach as a monitoring tool. Reports on the fatigue life of carbon composites subjected to lightning impulse currents of different intensities are scarce in the literature. A technique that would allow the remaining service life of carbon composites post lightning strike event to be determined as a function of electrical impact history could prove valuable in industry. Real-time resistance monitoring to test for impacts is another field of work worth exploring. Future work in this context should concentrate on further development

of the microstructural models used here, to simulate current penetration paths into carbon fibre composites with variable ply lay-ups. For this purpose, micro-computed tomography should be performed on small samples and the resulting data should be imported into COMSOL for comparison with finite element simulations.

REFERENCES

[1] M. Langley, "Carbon Fibers in Engineering", London, McGraw-Hill, ISBN 10: 0070844216 , 1973

[2] Clyne TW, Hull D. "An Introduction to Composite Materials", London, Cambridge University Press, ISBN 9780521388559, 1996.

[3] Piggott MR, "Load Bearing Fiber Composites", Oxford, Pergamon Press, ISBN 0080242316, 1980.

[4] Tsai SW, Hahn HT, "Introduction to Composite Materials". Westport, Technomic, ISBN 0877622884, 1980.

[5] Jones RM, "Mechanics of Composite Materials", Philadelphia, Taylor & Francis, ISBN 9781560327127, 1999.

[6] Angelidis N, Wei CY, Irving PE, "The electrical resistance response of continuous carbon fibre composite laminates to mechanical strain", Composites Part A: Applied Science Manufacturing, vol. 35, pp.1135–47, 2004

[7] Morley JG, "High-Performance Fibre Composites", Orlando, Academic Press, ISBN 9780125064453, 1987

[8] Earl SJ, "Some methods for modelling CFC for the effects of lightning", Challenges in the Modelling and Measurement of Electromagnetic Materials, IET, pp. 33–8, 2006

[9] Lodge KJ "A Designers' Guide to the Achievement of Electrical Continuity in Carbon Fibre Composite Structures", Caswell, Plessey, BR--100178 , 1986.

[10] Saleem A, Frormann L, and Iqbal A, "High Performance Thermoplastic Composites: Study on the Mechanical, Thermal, and Electrical Resistivity Properties of Carbon

Fiber-Reinforced Polyetheretherketone and Polyethersulphone", Polymer Composites, vol. 28(6), pp. 785–96, 2007

[11] W. G. Heath, "Carbon Fibre Composites- Promises and Problems " *AGARD Conference Proceedings No.112, Impact of Composite Materials on Aerospace Vehicles and Propulsion Systems*, 20-22 September, 1972.

[12] Howell, "Effects of Simulated Lightning Currrents on the Tensile Strength of Graphite/Epoxy " *Paper 38-1, International Conference on Lightning and Static Electricity,* June 1983.

[13] Reid, "Strength Degradation of CFRP due to Conduction of Simulated Lightning Currents with varying Moisture Content and Mechanical Loading " *Paper 10A.2, International Conference on Lightning and Static Electricity,* September 1989.

[14] M. G., "Mechanical Properties of bolts made by CFRP," *Composites (France),* vol. 6, pp. 33-35, 1993.

[15] R. Starikov and J. Schön, "Fatigue resistance of composite joints with countersunk composite and metal fasteners," *International Journal of Fatigue,* vol. 24, pp. 39-47, 2002.

[16] Whyatt O.H. and Hughes D. D, "*Metals, Ceramics and Polymers",* Cambridge University Press, London, ISBN 978-3-540-73448-2, 1974.

[17] Saunders G.A, "*Electron transport in graphites and carbons"* Academic Press, London 1970

[18] E. Fitzer and L. M. Manocha, "*Carbon reinforcements and carbon /carbon composites"* Springer-Verlag Berlin Heidelberg, ISBN: 978-3-642-63707-0, 1998.

[19] Hyer M. W, "*Stress analysis of fibre-reinforced composite materials"* Mc-Graw Hill Singapore, ISBN: 9780070167001, 1988.

[20] Diefendorf R.J. and Tokarsky E, "High Performance Carbon Fibres " *Polymer*

Engineering and Science vol. 15(3), pp. 150-159, 1975.

[21] M Guigon, A Oberlin, and G Desarmot , "Microstructure and structure of some high modulus, PAN base carbon fibres " *Fibre Science Tech* vol. 20, pp. 177-198, 1984.

[22] W Watt, and BV Perov, "*Strong Fibres, Handbook of composites"* vol. 1, ISBN**:** 9780444875051, 1985.

[23] C Thiagarajan, "Smart Characterisation of damage in carbon fibre reinforced composites under static and fatigue loading conditions by means of electrical resistivity measurements " *PhD thesis, Cranfield University UK,* 1995-1996.

[24] R. Grimberg, A. Savin, R. Steigmann, and A. Bruma, "Eddy current examination of carbon fibres in carbon-epoxy composites and Kevlar," *International Journal of Materials and Product Technology* vol. 27, pp. 221-228, 2006.

[25] R Schueler, SP Joshi, K Schulte, "Conductivity of CFRP as a tool for health and usage monitoring" *Smart Structures and Materials, SPIE proceedings* vol. 3041, pp. 417-426, 1997.

[26] J. B. Park, T. K. Hwang, H. G. Kim, and Y. D. Doh, "Experimental and numerical study of the electrical anisotropy in unidirectional carbon-fiber-reinforced polymer composites," *Smart Materials and Structures,* vol. 16, pp. 57-66 2007.

[27] M.N Miller, "Bounds for effective electrical, thermal and magnetic properties of heterogeneous materials " *Journal of Mathematical Physics* vol. 14 (11), pp. 1988-2004, 1969.

[28] J. Vilcáková, P. Sáha, and O. Quadrat, "Electrical conductivity of carbon fibres/polyester resin composites in the percolation threshold region," *European Polymer Journal,* vol. 38, pp. 2343-2347, 2002.

[29] M. Weber and M. R. Kamal, "Estimation of the volume resistivity of electrically conductive composites," *Polymer Composites,* vol. 18, pp. 711-725, 1997.

[30] L. Shen, J. Li, B. M. Liaw, F. Delale, and J. H. Chung, "Modeling and analysis of the electrical resistance measurement of carbon fiber polymer-matrix composites," *Composites Science and Technology,* vol. 67, pp. 2513-2520, 2007

[31] J. B. Park, T. Okabe, N. Takeda, and W. A. Curtin, "Electromechanical modeling of unidirectional CFRP composites under tensile loading condition," *Composites Part A: Applied Science and Manufacturing,* vol. 33, pp. 267-275, 2002.

[32] P. C. Conor and C. N. Owston, "Electrical Resistance of Single Carbon Fibres " *Nature,* vol. 223, pp. 1146-1147, 1969.

[33] C. N. Owston, "Electrical properties of single carbon fibres " *J. Phys. D: Appl. Phys.* , vol. 3 pp. 1615, 1970.

[34] Dresselhaus, M.S., Dresselhaus, G., Sugihara, K., Spain, I.L., Goldberg, H.A.., "Graphite fibres and filaments " *Springer Series in Materials Science* vol. 5, ISBN 978-3-642-83379-3, 1988.

[35] Y. Okuhara and H. Matsubara, "Memorizing maximum strain in carbon-fiber-reinforced plastic composites by measuring electrical resistance under pre-tensile stress," *Composites Science and Technology,* vol. 65, pp. 2148-2155, 2005.

[36] R. Schueler, S. P. Joshi, and K. Schulte, "Damage detection in CFRP by electrical conductivity mapping," *Composites Science and Technology,* vol. 61, pp. 921-930, 2001.

[37] K. Ogi, H. Inoue, and Y. Takao, "An electromechanical model for the temperature dependence of resistance and piezoresistance behavior in a CFRP unidirectional laminate," *Composites Science and Technology,* vol. 68, pp. 433-443, 2008.

[38] X. Wang and D. D. L. Chung, "Continuous carbon fibre epoxy-matrix composite as a sensor of its own strain " *Smart Mater. Struct.*, vol. 5 pp. 796-800, 1996.

[39] T. Prasse, F. Michel, G. Mook, K. Schulte, and W. Bauhofer, "A comparative investigation of electrical resistance and acoustic emission during cyclic loading of CFRP laminates," *Composites Science and Technology*, vol. 61, pp. 831-835, 2001.

[40] W. A. Curtin, "Multiscale Models of Multifunctional Composites for On-Board Damage Detection and Failure Prevention " AFRL-SRAR-TR-09-01572008.

[41] G. W. Reid, "Mechanical Damage to Aircraft Structures from Lightning Strikes," *Proceedings of the Institution of Mechanical Engineers, Part G: Journal of Aerospace Engineering*, vol. 207, pp. 1-14, January 1,1993.

[42] F. A. Fisher, J. A. Plumer, and R. A. Perala, " Aircraft Lightning Protection Handbook," Sep 1989.

[43] R.E Baldmin, G.W. Reid, and C. J.Hardwick, "Lightning hazard to modern aircraft structures and systems " in *Aerotech 87* Birmingham 27-30 October 1987.

[44] Society of Aeronautical Engineers. Aircraft Lightning Zoning. In: Aerospace Recommended Practice 5414. SAE International, 2000.

[45] P. L. Anders Larsson, Bondiou-Clergerie and Delannoy, "The lightning swept stroke along aircraft in flight. Part I: thermodynamic and electric properties of lightning arc channels " *Journal of Physics D, Applied Physics* vol. 33, pp. 1565-2346, 2000.

[46] Phillpot, "Recommended Practice for Lightning Simulation on Testing Techniques for Aircraft " UKAEA Report, CLM-R163.

[47] European Organization for Civil Aviation Equipment 'Aircraft Lightning Environment and Related Test Waveform' Report of EUROCAE WG-31 and SAE Committee AE4L, ED-84, 1997.

[48] European Organization for Civil Aviation Equipment. Aircraft Lightning Zoning Standard. Report of EUROCAE ED-91, 1998.

[49] M. A. Uman and V. A. Rakov, "The interaction of lightning with airborne vehicles " *Progress in Aerospace Sciences* vol. 39, pp. 61-81, 2003.

[50] Feraboli P, Kawakami H. “Damage of Carbon/Epoxy Composite Plates Subjected to Mechanical Impact and Simulated Lightning”, Journal of Aircraft, vol. 47(3), pp. 999–1012, 2010

[51] A. Piche, I. Revel, G. Peres, E. I. Works, and France, "Experimental and Numerical Methods to Characterize Electrical Behaviour of Carbon Fiber Composites Used in Aeronautic Industry," *Advances in Composite Materials - Analysis of Natural and Man-Made Materials,* vol. InTech, 09, September, 2011.

[52] M. Louis, S. P. Joshi, and W. Brockmann, "An experimental investigation of through-thickness electrical resistivity of CFRP laminates," *Composites Science and Technology,* vol. 61, pp. 911-919, 2001.

[53] D. D. L. Chung and S. Wang, "Discussion on paper ‘The electrical resistance response of continuous carbon fibre composite laminates to mechanical strain’ by N. Angelidis, C.Y. Wei and P.E. Irving, Composites: Part A 35, 1135–1147 (2004)," *Composites Part A: Applied Science and Manufacturing,* vol. 37, pp. 1490-1494, 2006.

[54] D. D. L. Chung, *Functional Materials Electrical, Dielectrical, Electromagnetic, Optical and Magnetic Applications* vol. 2, ISBN: 9789814287166, World Scientific 2010.

[55] A. Todoroki, " Long Life Durability of Electrodes of Electrical Resistance Change Method for Damage Monitoring of CFRP Composite Structures," Tokyo Institute Of Tech (Japan) Dept Of Mechanical Engineering March 2008.

[56] Rakov VA, Uman MA. “Lightning: Physics and Effects”. London: Cambridge University Press, ISBN: 9780521035415, 2003.

[57] P. Feraboli and M. Miller, "Damage resistance and tolerance of carbon/epoxy composite coupons subjected to simulated lightning strike," *Composites Part A: Applied Science and Manufacturing,* vol. 40, pp. 954-967, 2009.

[58] K. Yoshiyasu Hirano, Yutaka Iwahori, Akira Todoroki, "Artificial Lightning Testing on Graphite/Epoxy Composite Laminate," *Composites Part A: Applied Science and Manufacturing,* vol. 41, pp. 1461-1470, 2010.

[59] S. A. Baldacim, N. Cristofani, J. L. F. Junior, and J. R. Lautenschlager, "Lightning Effects in Aircraft of the Composite Material " presented at the Congresso Brasileiro de Engenharia e Ciência dos Materiais, Foz do Iguaçu, PR, Brasil., 2006.

[60] S. J. Haigh, "Impulse Effects during Simulated Lightning Attachments to Lightweight Composite Panels " presented at the International Conference on Lightning and Static Electricity Paris, 2007

[61] T. Ogasawara, Y. Hirano, and A. Yoshimura, "Coupled thermal–electrical analysis for carbon fiber/epoxy composites exposed to simulated lightning current," *Composites Part A: Applied Science and Manufacturing,* vol. 41, pp. 973-981, 2010.

[62] Johnson AF, Pickett AK, Rozycki P., "Computational methods for predicting impact damage in composite structures", Composites Science and Technology, vol. 61(15) pp. 2183–92, 2001.

[63] Chippendale, Richard D., et al. "Transport properties and current flow patterns in homogeneous strongly anisotropic materials." *COMPEL-The international journal for computation and mathematics in electrical and electronic engineering* 30.3 (2011): 1047-1055.